Wayne State University Dissertations

1-1-2018

3d Momentum Imaging Spectroscopy Probing Of Strong-Field Molecular And Surface Dynamics

Lin Fan
Wayne State University,

Recommended Citation

3D MOMENTUM IMAGING SPECTROSCOPY PROBING OF STRONG-FIELD MOLECULAR AND SURFACE DYNAMICS

by

LIN FAN

DISSERTATION

Submitted to the Graduate School

of Wayne State University,

Detroit, Michigan

in partial fulfillment of the requirements

for the degree of

DOCTOR OF PHILOSOPHY

2018

MAJOR: CHEMISTRY (PHYSICAL)

Approved By:

_____
Advisor   Date

_____

_____

DEDICATION

To my beloved families and lovely friends.

ACKNOWLEDGEMENT

TABLE OF CONTENTS

LIST OF TABLES

LIST OF FIGURES

x

CHAPTER 1. INTRODUCTION

1.1 Momentum imaging

Momentum imaging is an effective tool to study gas phase atomic/molecular dynamics. The reconstructed 3D momentum distributions of ions and electrons are very helpful to understand the excited electronic states and unravel multiple ionization/dissociation pathways of atoms/molecules and solid phase materials. The photon energy needed for single or multiple photon ionization and kinetic energy release of ions can trace which electronic and vibrational state were accessed and which dissociation potential energy surface the excited molecule or ion proceeded through to fragment. The angular distributions of ions/electrons provide information on transition dipoles, symmetry of electronic orbitals and the dissociation time period relative to a pulse duration. For electrons, the double ionization mechanism can be studied through the relative angles between two electrons.

Cold target recoil ion momentum spectroscopy (COLTRIMS) [1-2] and velocity mapping imaging (VMI) are widely used to implement momentum imaging. COLTRIMS combines both electric and static magnetic field to guide charged particles to a detector. VMI can focus ions/electrons with the same initial velocity but different generation locations to the same spot on a detector. VMI needs relatively high voltages (hundreds to thousands) to generate inhomogeneous electric field to accelerate/decelerate charged particles alone TOF axis (more details are included in Chapter 2).

1.2 Strong field ionization

In light and matter interaction, the primary step is the liberation of an electron from its binding state. For strong field ionization, Keldysh and authors of subsequent work [3-

5] suggested that an electron could tunnel through its atomic Coulomb potential that is suppressed by the intense laser field, as shown in Figure 1 (a). The electric field at the first Bohr orbit of a hydrogen atom is $E_a = e/a_b^2 = 5.1 \times 10^9$ V/cm, where $a_b = \hbar^2/mc^2 = 5 \times 10^{-9}$ cm is the Bohr radius. This field corresponds to the laser intensity $I_a = cE_a^2/8\pi = 3.4 \times 10^{16}$ W/cm^2. [6] A laser field with intensity comparable to this value can distort the Coulomb potential and tunneling ionization could happen.

Keldysh tunneling parameter is $\gamma = \sqrt{\dfrac{I_p}{2U_p}}$, where $U_p = \dfrac{e^2E^2}{4m\omega^2}$ is the ponderomotive potential, e and m are the charge and mass of an electron, E is the electric field strength at which the atom is ionized and ω is the angular frequency of the laser radiation. I_p is the ionization threshold of the atom. When $\gamma < 1$ ($I_p < 1/2U_p$), the laser intensity is strong enough to modify the Coulomb potential. One side of the Coulomb potential increases while the other side is suppressed down. An electron could tunnel through the lower side of the Coulomb potential. In other words, tunneling ionization is the dominant process when the laser intensity is sufficiently high. When $\gamma \ll 1$, the Coulomb potential could be bent so much that one side is even lower than the binding energy of an electron. This electron is field ionized directly, which is called over-the-barrier ionization. For $\gamma \gg 1$ ($I_p \gg U_p$), the laser intensity is not strong enough to deform the Coulomb potential significantly and multiphoton ionization process dominates.

1.2.1 Ultrafast lasers

The laser intensity comparable to molecular Coulomb potential could be reached easily by femtosecond Ti:sapphire laser pulses. Ultrafast Ti:sapphire laser was first developed in the 1980s.[7] Besides the strong laser intensity, the pulse duration is in the range of tens of femtosecond (10^{-15} s), which is the time scale for nuclear motion in

molecules. When exploiting an ultrafast laser pulse to excite a molecule/ion, electronic states are excited before the nuclear moves (vibration motion). The time scale of electron motion is in the range of tens to hundreds of attoseconds (10^{-16}s). To achieve higher time resolution to study electronic dynamics, scientists have been developing attosecond spectroscopy. High harmonic generation (HHG) and attosecond angular streaking are two ways to achieve attosecond time resolution. When strong field femtosecond laser interacts with noble gases/molecules, loosely bound electrons are ripped from gas molecules through tunneling ionization. These electrons can be accelerated away from the ion core. When the phase of the oscillating laser field changes, the electrons are decelerated and then accelerated back toward the ion core. The recollision of electrons and the ion core can leading to emission of high-energy photons (in the range of XUV and/or soft X-ray).[8] Each pulse inside the pulse train has a duration of tens to hundreds of attoseconds. The laser intensity to generate attosecond pulse trains is 10^{13} to 10^{15} W/cm^{-2}, which can be easily obtained with a Ti:sapphire femtosecond laser. Attosecond angular streaking is another way to reach attosecond regime. The changing phase of a laser pulse could deflect the emission angle between two ejected electrons when using circularly polarized ultrashort pulses to ionization atoms/molecules.[9-11] Using the angle and phase evolution of the laser pulse, the time duration of the two ionization events can be deduced. Ultrafast Ti:sapphire laser is the enabler for both HHG and angular streaking methods to explore interesting electron correlation dynamics in attosecond time domain.

1.2.2 Tunneling ionization and possible consequences

In Figure 1 (a), the laser polarization is along x direction and the electron with binding energy $-W_b$ could tunnel through the lower side of the modified potential barrier

alone either x of –x direction as the laser field oscillates. [12] The tunneling ionization rate is nonlinearly dependent on the laser intensity to high orders, so the ionization is confined to a small fraction of the period of a few-cycle NIR pulse, near the maximum intensity field. As shown in Figure 1 (b), the red thin curve shows a few-cycle NIR pulse and the grey line represents the envelope of this pulse. The green curve shows the time duration (several subfemtosecond) in which tunneling ionization happens. The scheme of tracing tunneling ionization in real time is shown in Figure 1 (c). A subfemtosecond XUV pulse and a NIR pulse were used as pump and probe beam to study the electron tunneling in atoms through monitoring the multi-electron excitation and relaxation processes ($\Delta t > 0$ implies that the XUV pulse arrives at the atom earlier than the NIR pulse). The authors also explained the mechanism to trace the tunneling ionization in time, as shown in Figure 1 (d). The binding energy W_2 is much larger than W_1. The electron with low binding energy could be removed at low laser intensities, where multiphoton ionization dominates, so there was no sub-half-cycle structure that was caused by tunneling ionization. By contrast, the electron with high binding energy was liberated by tunneling ionization, leading to sub-half-cycle steps in the integrated ionization profile.
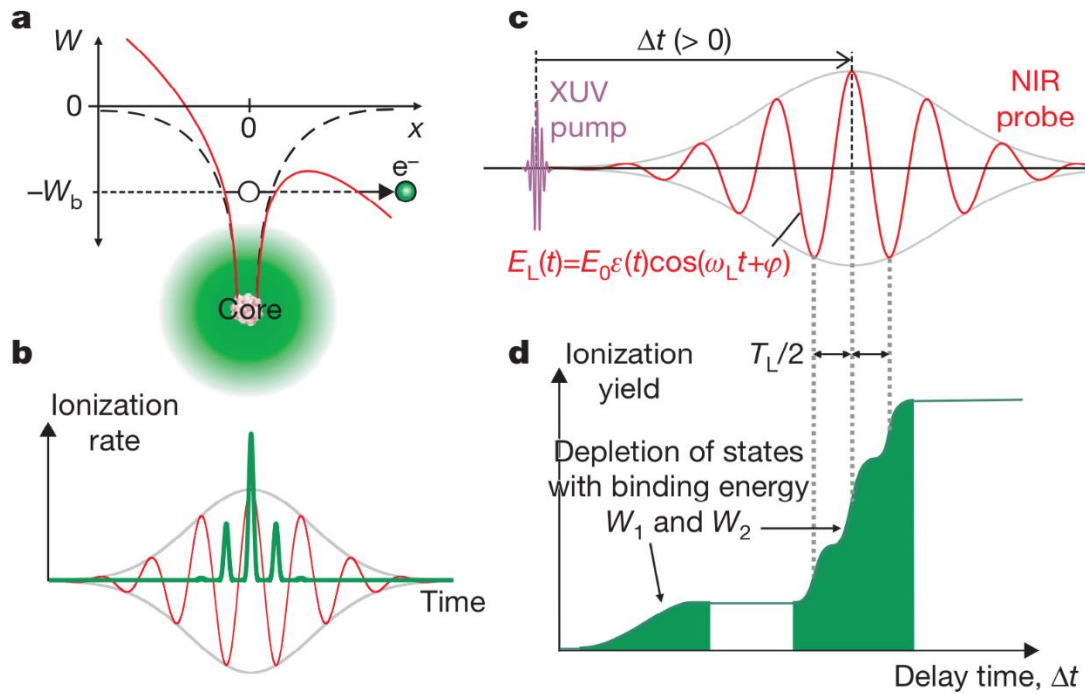
Figure 1: Schematic of strong-field tunneling ionization and pump-probe setting to observe it in real time. (a). Exposing an atom to a strong NIR laser field will result in a modified potential (solid red curve), which is the addition of the Coulomb potential (dashed curve) and the instantaneous electric potential of the laser pulse. (b). The red curve represents the oscillating electric field of an IR laser pulse. The thick green line represents the time interval in which tunneling ionization is restricted, near the maximum oscillating electric field of the laser pulse. (c). An XUV pulse generates ions in excited (shake-up) states, from which a time-delayed NIR few-cycle probe pulse liberates electrons to produce doubly charged ions. (d). The yield of cations as a function of delay Δt between the XUV pump and the NIR probe, for the case of electrons being excited into two shake-up states with different binding energy ($W_2 \gg W_1$) and then being freed via strong-field ionization. (Adapted from ref. [12])

In strong laser field, when an electron tunnels through the lower side of the modified Coulomb potential, there are other possible consequences besides being ionized, depending on the phase of the laser pulse at which tunneling ionization happens, as shown in Figure 2. At the tunneling exit, the electrons can be accelerated away from the ion core and driven back toward the atom/molecule when the direction of the laser electric field changes. The migration could be several tens of angstrom, much further than the radius of an atom or a small molecule. Elastic scattering with another electron could knock this

electron out with high kinetic energy. The returning electron could recombine with its

ground-bound state and emit a high-energy photon (HHG). This process is shown in the

elliptical inset of Figure 2, corresponding to process (ii). The electron could rip off another

electron when it is accelerated back, which is called non-sequential double ionization.

Alternatively, it could excite another bound electron with inelastic scattering. These

processes are shown as (i), (ii), (iii), and (iv) in Figure 2.
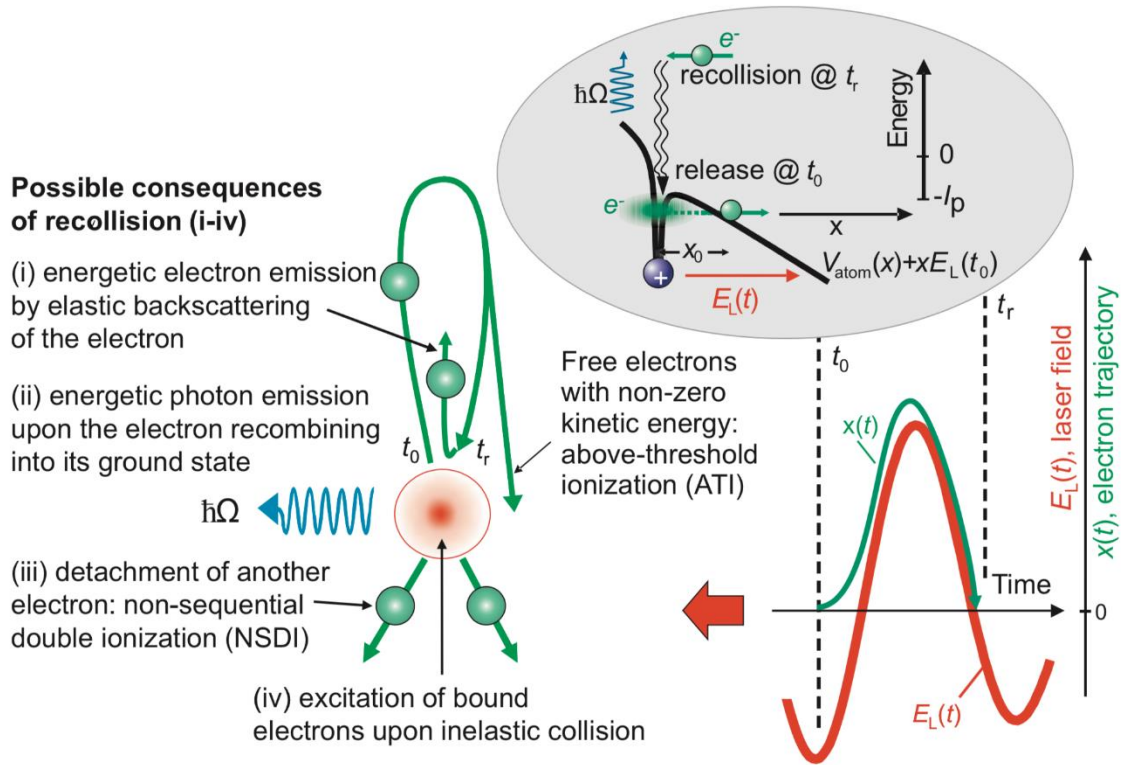
Figure 2: Strong field tunneling ionization of an atom at moment t_0 and subsequent returning of the detached electron at moment t_r to the parent ion in a linearly polarized ultrashort laser field. Possible consequences of the recollision are shown as i-iv. Inset: Release and recollision of a detached electron with the parent ion with the highest energy, leading to the emission of high-energy photons via process ii. (Adapted from ref. [13])

1.2.2.1 Attosecond pulse train (APT)

After a bound electron tunnels through the deformed Coulomb barrier in strong

laser field and is accelerated back to the ion core, the electron can recombine with the ion

core, generating high-energy photons with very short time duration (several tens to hundreds of attoseconds), which is called attosecond pulse train (APT). The temporal spread of the APTs could be characterized through several methods. Exploiting XUV-pump-XUV-probe technique requires a high XUV intensity and thus can only be applied at relatively low harmonic orders. [14] Attosecond streak camera method measures the relation between the kinetic energy of photoelectrons ionized by an XUV pulse and the phase of the laser field at the ionization event. [15-17] Another method is the resolution of attosecond beating by interference of two-photon transitions (RABITT), which is based on photoelectron detection through two-color ionization with one XUV photon and one driving laser photon (IR). Two ionization processes, absorption of a XUV photon and a prob IR photon ($q\omega_{IR} + \omega_{IR}$) and absorption of a higher-order XUV photon and emission of an IR photon (($q+2$) $\omega_{IR} - \omega_{IR}$), could lead to a same sideband with kinetic energy in-between two neighboring peaks originated from direct ionization with XUV photons, $q\omega_{IR}$ and ($q+2$) ω_{IR}. These two ionization pathways leading to the same sideband can interfere constructively or destructively, and this interference can be controlled by the time delay between the APT and IR filed. The sideband signal is proportional to $\cos (\phi_{q+2} - \phi_q + 2\omega_{IR}\tau + \Delta\phi_{atomic}^f)$, where ω_{IR} is the IR field frequency, τ is the time delay between two laser beams, $\Delta\phi_{atomic}^f$ is atomic phase. This phase can be obtained from theoretical calculations and is a small value. With recording the sideband intensity as varying the delay τ and performing a cosine fitting to the obtained data, the phase difference between two neighboring harmonic peaks ($\phi_{q+2} - \phi_q$) can be determined. [18-19] The RABBIT scheme, in turn, can control photoemission from atoms and molecules at attosecond time scale. A mixing even and odd harmonics generated by combining 800 nm and 400 nm laser beams and a following weak

800 nm IR pulse were used to generate asymmetric electron emission along the polarization direction (up and down direction), shown in Figure 3. [20] When employing mixed odd and even harmonics, the photoemission showed strong asymmetry along up and down direction (Figure 3 (b) and (d)), and the symmetry is unobservable when using odd harmonics only to ionize the target atom (Figure 3 (a) and (d)). The favored emission direction can be controlled by changing the time delay between the two laser fields. On the other hand, the asymmetry emission has relation with the relative phase of the odd and even harmonics trains, allowing the measurement of the relative phase of consecutive odd and even harmonics.
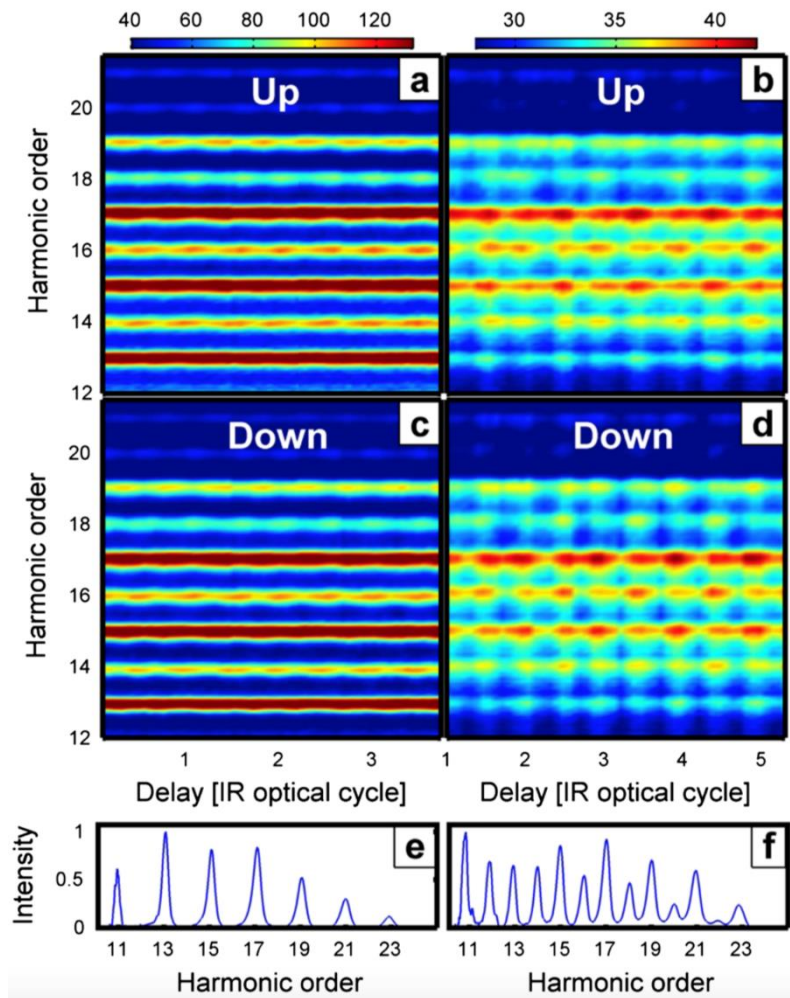
Figure 3: Photoelectron energy spectra as a function of the time delay between the APT formed by harmonics in (e) and (f) and IR pulse. (e), (f). Harmonic spectra for (e) odd harmonics only and (f) mixed odd and even harmonics. (Adapted from ref. [20])

1.2.3 Above-threshold ionization (ATI)

At laser intensity above 10^{13} W/cm^2, one or more extra photons (hv) could be absorbed above the ionization threshold of an atom/molecule, and the kinetic energy of the released electron will be nh$v$ + E$_0$, where E$_0$ is the kinetic energy of an electron ionized with minimum number of photons to ionize the atom/molecule, and n is the number of extra photons absorbed. This process is called above-threshold ionization (ATI). Figure 4 shows a schematic of the ATI process in Xe ionized with intense Nd-doped yttrium-aluminum-garnet pulses at 1064 nm. [21] The peaks labeled from S1 to S8 are ATI peaks ionized from P$_{3/2}$ core level of Xe after absorbing 11 + N photons. The kinetic energy of peak S0 is E$_0$ as defined above.
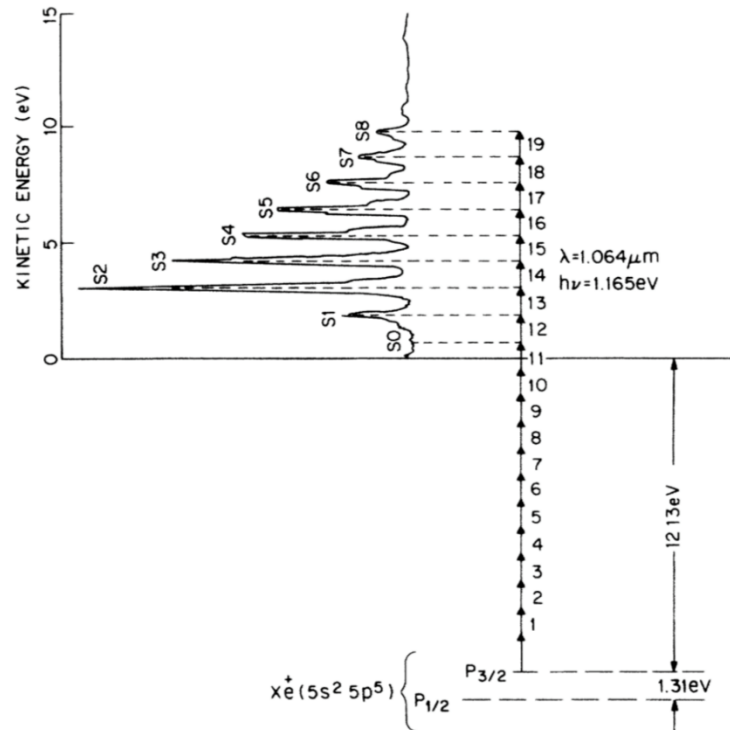
Figure 4: A schematic of the ATI process for xenon ionized by an intense Nd:YAG laser beam at 1064 nm. The (doublet) peaks are labeled by SN where N is the number of photons absorbed beyond the ionization potential of xenon. The Y-axis is the kinetic energy of the free electron. [21]

Zipp et. al. employed a new phase measurement technique to explore the intrinsic time delay in ATI process. [22] They observed asymmetry distribution in photoelectron spectrum when varying the relative phase (delay) between a 400-nm strong field and 800-nm weak field to ionize Argon, which is similar to the RABBIT scheme. The interfering signal of sidebands indicates the relative phase of neighboring ATI channels (one photon difference), corresponding to a resolution of a few attoseconds. These relative delays depend on the laser intensity and approach zero at high laser intensity. They illustrated that one of the most noticeable features is the ATI peaks and sideband peaks are roughly π out of phase (~500 *as*) and the phase dispersion of main ATI peaks is much larger than that of sidebands.

1.2.4 Bond softening and above-threshold dissociation

In 1990, theoretical calculations were performed to understand above-threshold dissociation process. A set of field-dressed energy states of H_2^+ is shown in Figure 5. $2p\sigma_u$ is a repulsive H_2^+ electronic state and is asymptotically degenerate with the ground state of H_2^+ $1s\sigma_g$. Figure 5 (a) shows these two states were combined with up to ±5 photon states. At a wavelength of 329.7 nm, the three-photon vertical transition from $v = 0$ state of $1s\sigma_g$ to the dissociation continuum of the repulsive $2p\sigma_u$ state could take place. [23] The three open channels $|d> = |u, n=1>$, $|g, n=2>$, $|u, n=3>$, were the dominant photodissociation pathways, with low possibility of tunneling into the n = 1 channel (Figure 5 (b)). The authors raised a paradoxical result that the n = 3 channel was dominant only at low intensity (7×10^{12} W/cm^2). This channel was suppressed, and n = 2 channel begun to dominant when

laser intensity increased, despite the 3-photon ionization process (I^3 dependence). They explained that the atoms "return" one quanta of photon energy to the laser field through stimulated emission after the separation fragments passed through the |g, n = 2> and |u, n = 3> channel crossing at R ≈ 3.5 a. u. along the |u, n = 3> channel. They further proposed that the dissociation "borrowed" energy from the radiation field to initiate the decay of the resonance, but finally "return" energy to the field through simulated emissions, which led to low fragments with low kinetic energy.
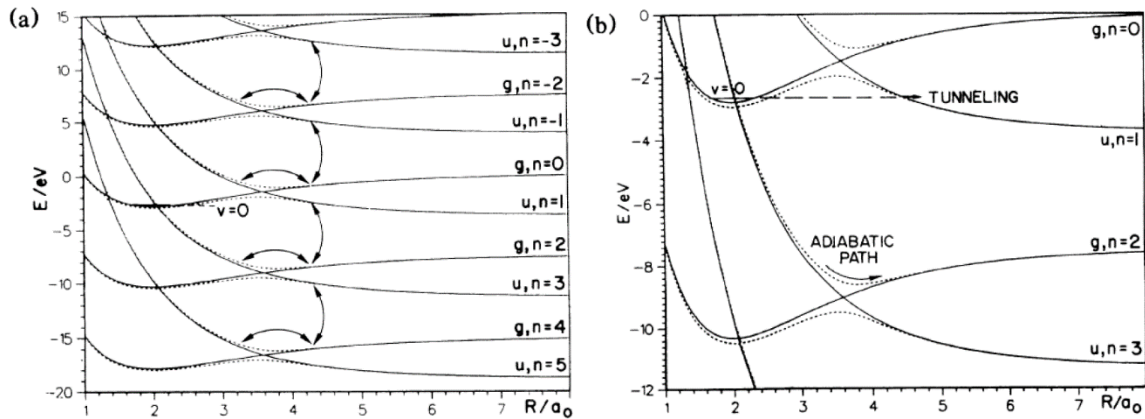
Figure 5:   (a) Potential-energy curves of the two electronic states of H_2^+ ($1s\sigma_g \rightarrow 2p\sigma_u$) dressed with ± 5 photons of wavelength 329.7 nm. The solid lines represent the ten interacting diabatic channel states. Arrows indicate direct radiative couplings. The dotted lines represent the field-dressed "adiabatic" curves after diagonalizing the radiative interaction at 1.4×10^{13} W/cm^2. (b) Zoomed in (a) in the region of the curve crossing points which dominate the dissociation process. (Adapted from ref. [23])

Bucksbaum et al. also studied above-threshold dissociation. They demonstrated that when laser intensity is comparable to internuclear binding fields (≈ 3 V/Å, or ≈ 10^{14} W/cm^2), the internuclear potentials become gently repulsive, but without any electron being removed.[24] The molecular bond is "softened" in this way. They also utilized H_2 as an example to illustrate the general dissociation process: A H_2 molecule was ionized to the $v = 5$ vibrational state of the H_2^+ ground state $1s\sigma_g$ (Figure 6). The $v = 5$ vibrational state

became unbound, with an opening gap at the adiabatic crossing ($R \approx 4a_0$), when the axis of H_2^+ aligned with the laser polarization. The H_2^+ dissociated and generated H^+ with kinetic energy ($E_{v=5} + h\omega - E_{diss}$)/2. They observed three peaks separated by half of the photon energy in the energy spectrum of H^+ and attributed this to the excess absorption of photons than the minimum requirement for dissociation instead of ionization, so they named this process as above threshold dissociation to differentiate from ATI. In this process, many photons are absorbed but finally "returned" to the laser field through stimulated emission, leading to ion fragments with low kinetic energy. At the conical intersection of two surfaces (resonance point), one molecular/ionic state could move adiabatically to another potential surface, which lead to absorption or emission of photons in this process. The gap of the avoided crossing near $R = 4a_0$ became wider when the laser intensity increased from 3.5 TW/cm^2 to 56 TW/cm^2, leaving most vibrational states in $1s\sigma_g$ electronic state unbound.
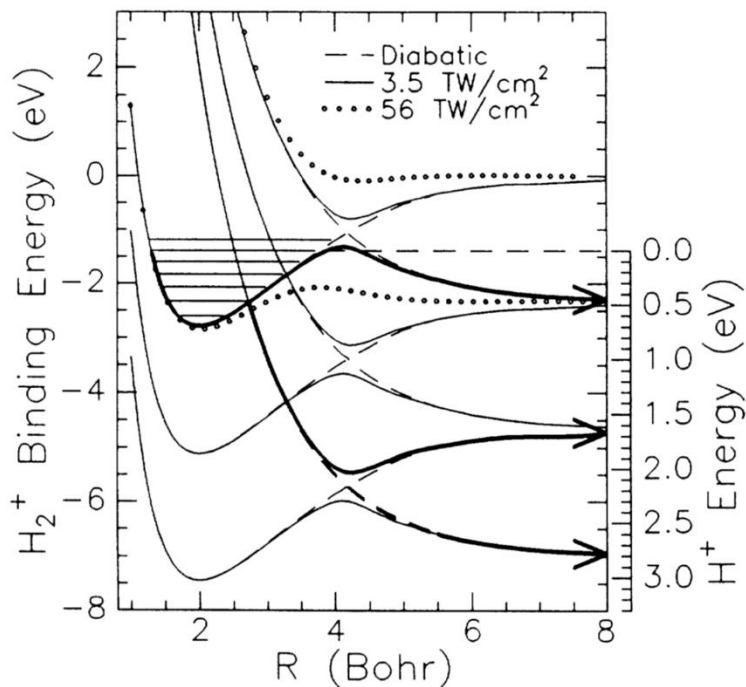
Figure 6: A Floquet calculation shows that the H_2^+ molecular potential is modified by intense light polarized along the internuclear axis. At 3.5 TW/cm^2, the vibrational state v

= 6 is not bound. At 56 TW/cm^2, most vibrational levels in the $1s\sigma_g$ electronic state are unbound. The bold lines indicate the adiabatic and diabatic channels for dissociation of the H$_2$ molecule. (Adapted from ref. [24])

1.3 Introduction to condensed phase studies

A. Relation between energy levels in solids and the kinetic energy distribution of electrons excited by photons with energy hv.

B. Hemispherical deflection analyzer.
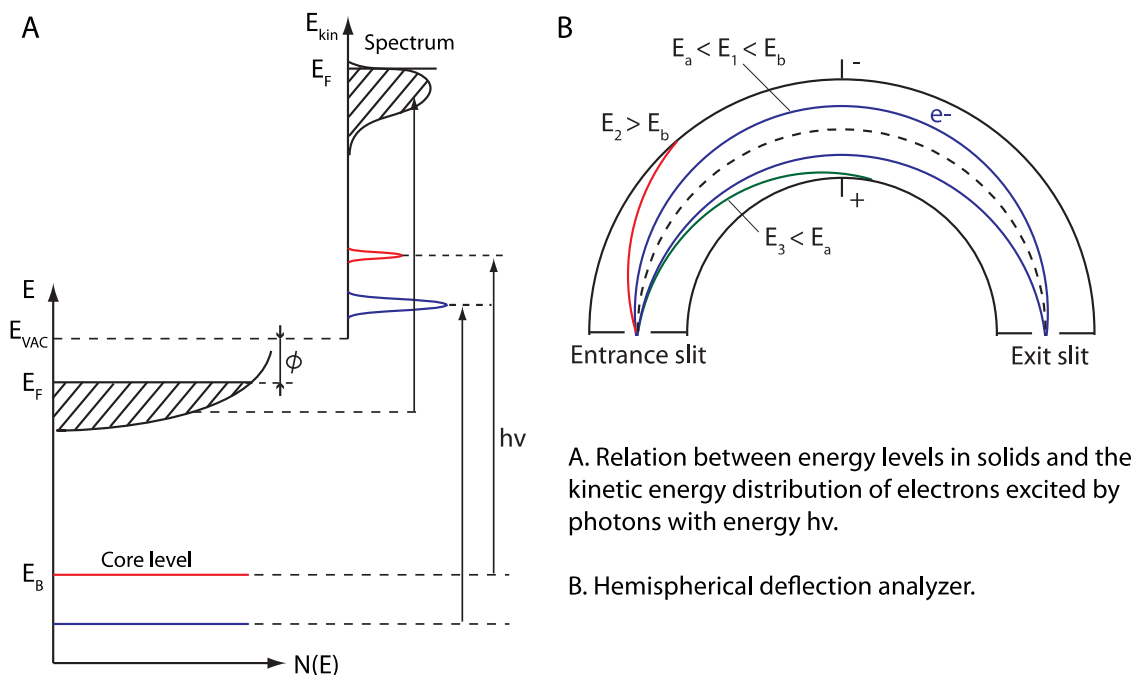
Figure 7:   (A) Relation between energy levels in solid and the kinetic energy distribution of emitted electrons. The red and blue colors represent core level electrons and the corresponding peaks in a KE spectrum. The shaded areas represent valence electrons close to Fermi level and the corresponding peak. (Adapted and modified from [25]).

Figure 7 shows the relation between the energy levels in a solid and the kinetic energy spectrum by exciting core and valence level electrons with photon energy of hv. Binding energy (E$_B$) is the energy of electrons relative to Fermi energy (E$_F$), which is the highest occupied energy level in a material at absolute zero Kelvin. Work function is the minimum energy required to remove an electron from Fermi energy to vacuum level and it is labeled as Φ in Figure 7 (A). With an incident beam that has photons energy hv, electrons in a solid sample are excited and liberated to vacuum. When the photon energy is high enough, core level electrons can be ripped from the sample and be detected with

kinetic energy $E_{kin} = h\nu - \Phi - |E_B|$. The peaks in the KE spectrum represent electrons from different core levels and the conduction band. The core level marked as red has lower absolute binding energy than the one marked as blue, so photoelectron originated from this level has higher kinetic energy. The electrons emitted from Fermi level (E_F) should have the highest KE (the binding energy of E_F is 0). The emitted photoelectrons from a surface are normally investigated by angular-resolved photoemission spectroscopy (ARPES). By studying the KE distribution of the detected photoelectrons, PES can study the electron energy distribution inside a solid sample, i. e. the band structures.

Ultra-high vacuum level (lower than 10^{-9} torr) is required to lower the absorption rate of background atoms/molecules (such as H_2O) on surfaces and obtain accurate results for surface studies. The incident beam to excite electrons could be x-ray, ultraviolet (UV), synchrotron radiation source, and focused electron beams from electron guns. The photoemission process from 2D surface or bulk solid material is normally interpreted with a three-step model: First, an electron is excited by an incident photon or electron. The second step is that this excited electron travels to the surface. The third step is that the electron escapes from the surface to vacuum and be detected.

The kinetic energy of emitted electrons can be detected by different kinds of energy analyzer, such as electrostatic and TOF analyzer. An electron analyzer is compatible with all excitation sources, which include plane mirror analyzer, cylindrical mirror analyzer, cylindrical deflection analyzer and hemispherical analyzer. Among these analyzers, hemispherical analyzers are widely used. It consists of two concentric hemisphere electrodes. The electrode with a smaller radius has higher electric potential than the other one to guide electrons to pass through. Only electrons with selected energy range can exit

this analyzer. As shown in Figure 7 (B), the electrons (blue color) with kinetic energies that are in the range of [E_a, E_b] pass through the analyzer. Electrons with higher energy than the maximum pass energy will hit the outside electrode, and the ones with lower energy than the minimum pass energy will hit the inside electrode. The pass energy range can be adjusted by the voltages applied on the two hemispherical electrodes. A retardation stage (lenses) is normally used prior to the entrance slit to decelerate (accelerate) electrons without changing the absolute energy spread and improve the energy resolution. [25] At an early stage of development, electron multipliers were used to detect electrons that passed through the exit slit. The input aperture size of an electron multiplier is normally below 20 mm. 2D MCPs was widely used to replace electron multiplier in PES. It is position-sensitive and has a larger acceptance area (~75 mm in diameter). It is worth mentioning that the TOF analyzer only works for pulsed excitation beams.

With the ability to detect kinetic energies of emitted electrons from solid surfaces, ARPES can map the band structures of the materials by varying the relative angle between surface normal direction and the acceptance slit of an energy analyzer. These polar angles can be transformed to lattice momentum and the kinetic energies can be converted to binding energies through the relation shown in Figure 7 (A). An example of mapping the band structure of graphite is shown below in Figure 8. Panel A shows the energy distribution curves at different polar angles using HeI incident light (45°) and the inset illustrates the Brillouin zone of graphite. [26] The spectra in A shows that the binding energy shifts toward the Fermi energy at a larger polar angle. Panel B shows the comparison between the measured band structures and theoretically calculated values.
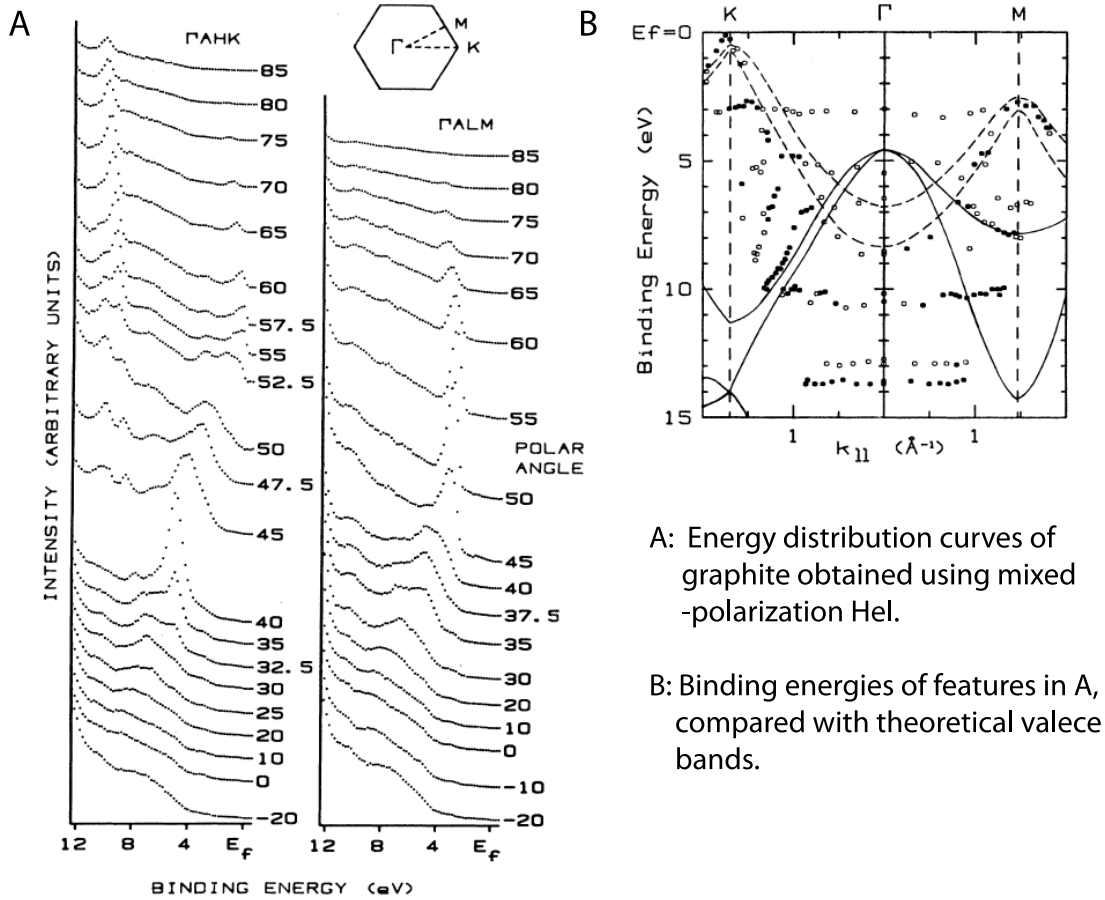
Figure 8: Energy distribution curves of graphite and comparison with theoretical valence bands. In panel B, filled dots represent strong or distinct features and hollow circles are weak features. Dashed lines are calculated π bands. Continuous lines are calculated σ bands. [26]

1.3.1 Multiphoton photoemission and image potential states

The emergence of ultrafast laser allows time-resolved studies of electron dynamics on surfaces through ARPES in extremely short time scale, femtosecond or subfemtosecond time domain. Photon energies of ultrafast lasers, such as Nd:YAG and Ti:Sapphire laser, are lower than the work function (~ 4.5-5 eV) of metals, such as Cu, Au, Ag, and Al. Multiple photons are needed to liberate an electron from Fermi sea, i.e. multiphoton photoemission.

An electron at a distance z in front of a metal surface could experience an attractive force $F(z) = -e^2 / (2z)^2$ applied by a positive charge (mirror image) inside the surface at the same distance, shown in Figure 9 (A). An electron below Ev could be trapped by this potential well, which is formed by the Coulomb-like attractive image potential $V(z) = -e^2/4z$ and the repulsive surface barrier. This leads to a series of Rydberg-like quantized electronic states close to E_v with energies E_n: $E_n = -0.85 \text{ eV}/(n+a)^2$, n = 1, 2, 3…. [27] These states are called image potential states (IPSs).

A Ti:sapphire laser beam with a pulse duration of 70 fs and frequency-tripled 95-fs beam have been exploited as pump and probe beams in time-resolved ARPES to study the lifetime of IPSs. [27] As shown in Figure 9, one UV photon with energy $\hbar\omega_a$ excites an electron below Fermi surface to an IPS, and a fundamental IR photon with energy $\hbar\omega_b$ excited the electron to the energy above vacuum level (E_V). This method is referred as time-resolved two-photon photoemission spectroscopy (TR-2PPE). The UV laser has a bandwidth ~14 meV and can excite a specific low-order IPS (n=1, 2, and 3) that is relatively widely separated from its neighboring state. As the energy gaps of higher-order IPSs (n ≥ 4) become smaller, the bandwidth of the UV laser becomes comparable of the energy separations and can excite several states simultaneously. The interference of adjacent eigenstates and quasi-classical motion of the coherent electron wave packets can be measured with a probe beam. They observed quantum beats in photoelectron spectrum, arising from the interference of neighboring eigenstates, after coherent excitation of three IPSs (n=4, 5, and 6, $E_B \simeq 40$ meV) of Cu. They also displayed the time and spatial evolution of the generated coherent states from IPSs centering around n=7 ($E_B \simeq 15$ meV) within the first 2 ps. It clearly showed that the electrons excited to these states can travel more than

200 Å away from the Cu surface and oscillate back and forth toward the surface with a
period of ~800 *fs* (Figure 9 (c)).
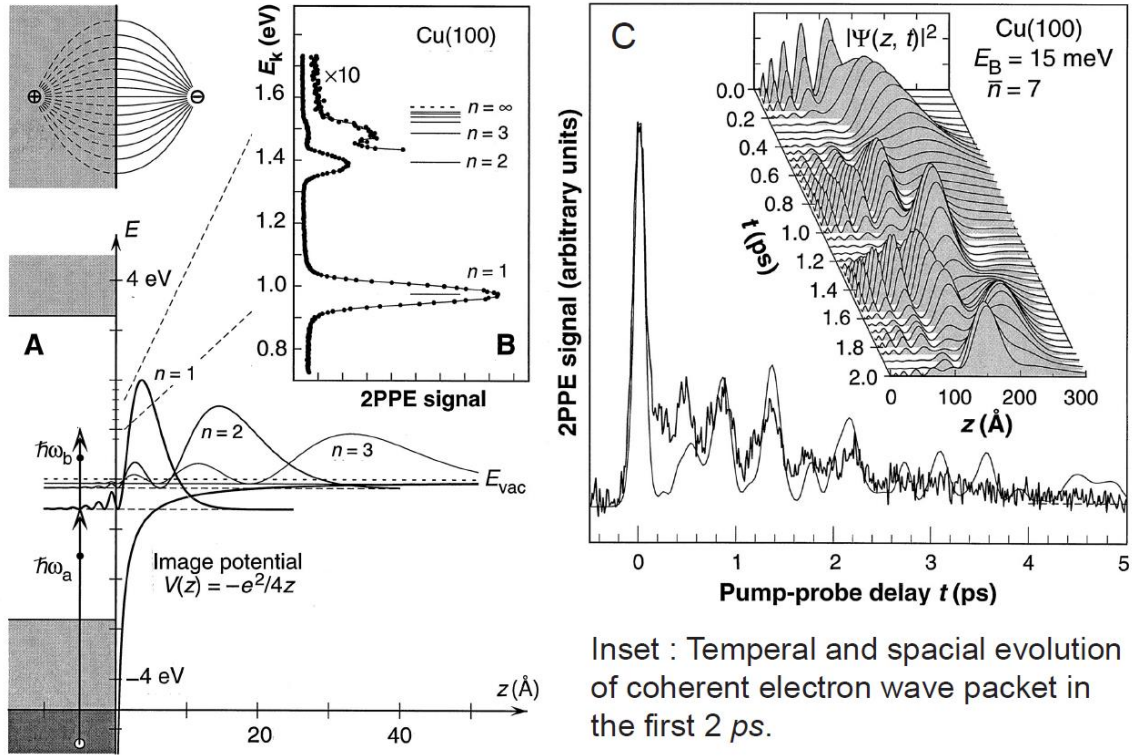
Figure 9: (**A**) Electric field and energy diagram of an electron in front of a Cu(100)
surface. A series of discrete hydrogen-like electronic states are formed due to the potential
well generated from the *sp* band gap (unshaded area) and the Coulomb tail, which are called
image-potential states. The probability densities of the lowest three image-potential states
are shown (n=1, 2, and 3). (**B**) The 2PPE spectrum obtained from employing a pump beam
with photon energy $\hbar\omega_a$ and probe beam with photon energy $\hbar\omega_b$. (Adapted from ref. [27])

The development of HHG has brought the duration of a laser pulse from
femtosecond to attosecond time domain. With such short pulses, time-resolved
experiments could achieve higher time resolution. Electronic states with very short lifetime
can be investigated. Thus, attosecond techniques have not only been applied in studying
gas-phase atomic/molecular dynamics, but also to explore the electron lifetimes at different
states in photoemission process on surfaces of condensed-phase materials. XUV beam with
photon energy of ~91 eV from high-harmonic generation of Neon and a weak IR dressing

field have been used to measure the delay time between photoemission originating from 4f core level and conduction band of a tungsten (110) crystal sample, which was 110 ± 70 as. [28] The different group velocities of these two electron wave packets traveling to the surface was considered to explain the observed delay.

1.3.2 The application of VMI on surface experiments

VMI and TOF techniques are traditionally employed in photoionization and dissociation of gas-phase atoms/molecules. They have the capability of measuring momentum, energy and angular distributions simultaneously. The acceptance angle VMI is 4π solid angle, while ARPES normally have an acceptance angle of $\pm 15°$. Extending the application of VMI and TOF techniques to explore electron dynamics with relatively low kinetic energy (typically < 100 eV) in condensed phase materials becomes very meaningful in this scenario. Field-free TOF tubes and delay line detectors have been exploited to detect the photoelectrons emitted form Cu(111) crystalline surface with frequency-quadrupled femtosecond laser pulses at a photon energy of 6.2 eV. The incident beam is on the same side of the detector and has an angle with the surface normal. The acceptance angle of photoelectrons was 22°.[29] Photoemission from a 400 nm thick Au film has been velocity mapped and the 2D transverse velocity distribution (in detector plane) has been imaged by an MCP detector. [30] It adopted a similar reflective geometry with "traditional" ARPES; the incident beam has an angle of ~84° with respect to the surface normal. Berglund-Spicer three-step photoemission model was used to interpret the experimental data. This model was derived for single photon photoemission process early, when the ionization sources normally had much higher photon energies than the work function of metals, such as X-ray, XUV or synchrotron radiation. The authors accommodated this model to multiphoton

photoemission process by implying that an electron absorbs enough photon energies instantaneously instead of sequential, which implies that the parallel momenta do not change as it does in sequential absorption of photons due to possible electron-electron, electron-photon, and electron-impurity scatterings. An electron temperature of 6000 K gave the best fit to the reconstructed experimental velocity distribution.

$$N(E)dE \propto \frac{K\,C(E)\,\alpha}{\alpha + 1/l(E)}\,dE \times [1 + 4(\frac{E-E_f}{nhv} - 1 + \ln\frac{nhv}{E-E_f})] \qquad (1)$$

where E_f is the Fermi energy of Au, L(E) is the electron-electron scattering length, C(E) is a semiclassical threshold function, α is the absorption efficiency and taken as a constant, independent of electron energy, and K is a correction factor related to C(E) and α l(E) (0.5-1). [30]

Besides the 2D surface material, nanoparticles have also attracted extensive interests and efforts to explore their properties. A technique called scanning photoionization microscopy (SPIM) has been employed to study the local electric properties from nanostructures in metallic films and nanoparticles. [31] The sample was grounded, and a Faraday cup was placed 5 mm above the sample and applied a voltage. The Faraday cup can also collect photons, so this technique can generate both fluorescence and photoelectron microscopy images. In this paper, spatial imaging capability was demonstrated by imaging a patterned Ag surface. Two following studies showed the plasmonic-enhanced SPIM images of Au nanoparticles deposited on a Pt film and an indium-tin-oxide (ITO) film. Due to the electric near-field enhancement on these nanoparticles when they were exposed to lasers, the photoemission yield showed a strong dependence on the polarization angle of the incident laser pulses. The influence of laser wavelength on photoemission yield was studied. The result showed that individual particles

have different responses at different laser wavelengths. Photoemission intensity of some nanoparticles went up, while some other nanoparticles had an opposite trend. A relatively weak upward trend was observed as the wavelength for the averaged emissivity increased in all cases. [32]

CHAPTER 2. APPARATUS DEVELOPMENT

2.1 Introduction

2.1.1 Velocity mapping imaging

Velocity mapping imaging (VMI) is an effective tool to measure momentum distributions of charged particles arising from photoionization/photodissociation due to its capabilities of 4π solid angle collection and velocity focusing. It consists of several parallel-placed cylindrical electrodes, which are normally 1 ~ 2 mm in thickness. When appropriate voltages are applied on these electrodes, an inhomogeneous electric field is generated. The equipotential lines of this electric field are close-to-parallel to the electrode plates. These electrodes have round openings in the center to allow charged particles to pass through, but they cause the equipotential lines to have a little bit distortion close to the edge of the openings. In such electric field, charged particles experience forces mainly along the axial direction (perpendicular to the electrode plates), while transverse momenta are close to conserved. The photoionization position is in the center between the first (i.e. repeller) and second electrode. The spatial distribution of nascent charged particles is affected by molecular beam size (expansion after a skimmer), and the beam waist size of focused laser beam and momentum. VMI can focus charged particles with same initial velocity but different generation locations (within ~3 mm) to the same point on a detector, making the arrival positions of charged particles independent on their initial positions. This velocity focusing of VMI can improve velocity resolution when studying ionization/dissociation dynamics through initial momentum distribution. The ionized parent ion or/and dissociated fragments expand in 3D space with different initial velocities. Meanwhile, they are accelerated by the electric field toward the detector.

Conventional VMI apparatus accumulates 2D position distribution of ions on a detector. It does not measure the TOF of each charged particle. Only the TOF of zero-momentum charged particles (time zero) is recorded by a single anode photomultiplier tube (PMT).

The modern technique was first implemented by Eppink and Parker in 1997 [33], who introduced the open-electrode design. Wiley and McLaren's setup has similar configurations, but the extractor (the second electrode) and ground plate (the third electrode) are made of girds. [34] The two grids could distort ion trajectories significantly and lower the transmission of ions. Reducing one grid had been executed to reduce the distortion and increase the transmission of ion/electrons, but this setup still had limitations. In order to minimize the distortion of equipotential lines between the grid wires, fine grids were needed, which however could further reduce the transmission. The open-electrode design exploited by Eppink and Parker allows 100% transmission and eliminated the blurring caused by different origin positions.

Slicing velocity mapping imaging (SVMI) technique was developed to improve the velocity resolution, in which an MCP detector was gated by a high-voltage pulser to obtain relatively thin temporal slice (~40 or 50 ns) of an ion Newton sphere. Gebhardt et. al. first displayed different TOF slices of $^{35}Cl^+$ ion cloud in the dissociation of Cl_2. [35] They used delayed extraction to allow the Newton sphere to expand more. The narrowest gate time was about 50 ns. Only when the TOF of ion cloud is relatively long comparing to this gate limit, thin TOF slice can be achieved. They demonstrated one advantage of slice imaging is that it could eliminate the noise along the symmetry axis when using inverse Abel transform. However, the time lag between the ionization and extraction is not necessary

when the spread of TOF is long enough, such as hundreds of μs. Townsend et. al. employed different electrode configurations to implement slice imaging.[36] They increased the expansion of the ion cloud by adding one more electrode to traditional "three-lens" assembly and using long TOF tube (~ 1 m). The velocity resolution ($\Delta v/v$) was improved from 5% to 2.8% comparing with unsliced images. Lin et. al. developed a different ion optics strategy to allow the application of low extraction field and to have wider TOF spread (hundreds of ns). [37] This goal is consistent with that of the above work, because avoiding delay extraction is important to obtain high mass and velocity resolution. The ion optics they developed was quite different from the traditional configuration. There were 29 cylindrical electrodes in total. They were equally spaced (1 cm) and connected by precise resisters to generate two sections of homogeneous electric field. This is analogous to that "lens 1" and "lens 2" contain several electrodes and each of them is several centimeters in thickness. The voltages applied on "lens 1" and "lens 2" were divided by resisters. They reported the achieved velocity resolution in transverse plane is 1%. This ion optics design triggered interests to carry out studies described below. Ryazanov et. al. developed an ion optics set that includes 14 apertures in total; and similarly, they divided these apertures into two effective field regions. [38] The TOF region is relatively long, 63 cm. They added an Einzel lens set to bend the ion trajectory gently, compressing the Newton sphere without affecting the spatial focusing of VMI. When the focusing lengths of ion trajectories are long, this method is helpful because it can control the size of the Newton sphere not to grow larger than the detector size without affecting the spatial focusing. In other words, it can increase the upper limit of kinetic energy that the ion optics and detector can detect.

The recent development of laser technology has raised the need to detect high-energy electrons up to keV. Femtosecond intense laser pulses could generate high-energy electrons through ponderomotive acceleration. Meanwhile, it can produce HHG pulse trains with photon energy from a few tens to hundreds of eVs. On the other hand, free-electron lasers that generate X-rays also have high energy photons up to keV. When using these light sources to conduct photoionization and dissociation studies, the obtained photoelectrons could have keV kinetic energy. To detect these high-energy electrons, Kling et. al. developed an electron optics that can accept 1 keV electrons with a Φ80mm MCP detector when applying -30 kV to the repeller. [39] They also adopted a "thick lens" strategy to build the ion optics, which consisted of 11 electrodes. The TOF region was short (~6 or 7 cm) to accept high-energy charged particles, because the other two methods have limitations. Increasing the size of MCPs is not ideal because the MCP (Φ80 mm) they used in the spectrometer was already expensive. They did not update the detector because of the high cost. The other way is to increase the voltages applied to repeller. They stated it was hard to apply voltages higher than 30 kV due to the necessary insulation. The best energy resolution they could achieve is 1.4%. Another team also reported velocity mapping high-energy charged particles up to keV regime by applying moderate voltages (~20kV) [40]. They designed an improved version (4-lens) of the Eppink-Parker setup, with an extra electrode and very short TOF length (4 cm).

2.1.2 Electron-ion coincidence measurements

Coincidence measurements provide comprehensive information on dissociative photoionization events by detecting both ion fragments and electrons in coincidence. Earlier, photo-ions and photoelectrons in coincidence were extracted in a relatively simple

way; only two or three electrodes were utilized to generate an electric field. [41-42] Because it is relatively difficult to obtain good velocity mapped imaging on both sides simultaneously, some scientists pulsed the electric field of double-side VMI apparatus to obtain good spatial and temporal resolution. [43] Because of the comprehensive information that coincidence measurements can provide, it is advantageous to find new reaction pathways/mechanics. Cao et. al. confirmed a new bond-breaking pathway of Deuterium molecule with UVU pump (16.95 eV) and IR prob beams. They interpreted this process as predissociation of the diatomic molecule into two atoms and following photoionization of one dissociated atom by the IR pulse. By combining electron-ion coincidence technique with 3D detection, the detected final fragments and electrons could give comprehensive information to identify different dissociative ionization pathways. As shown in the ion-electron coincidence map (Figure 10 (d)), D^+ ions with KE around 0.08 eV and 0.4 eV originate from two competing pathways. D^+ with higher KE is from the pathway illustrated above and lower KE is from the generation of D_2^+ by the UVU pulse and excitation to a repulsive excited electronic state that leads to a D atom and D^+ ion. Besides these merits, coincidence measurements are also helpful to remove background electrons, such as those from water, N_2, and O_2, by selecting electrons in coincidence with interested ions.
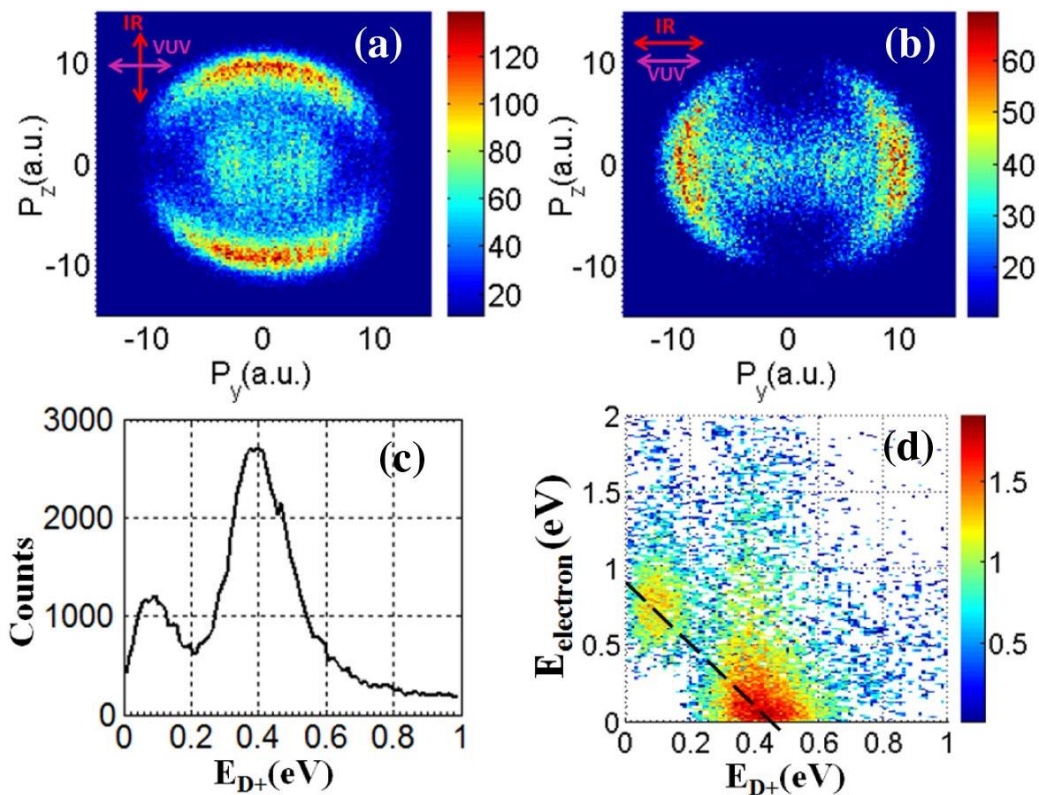
Figure 10: D^+ momentum distribution with 11th harmonic pulse (17.45 eV) as the pump and the polarization of the prob IR beam (a) perpendicular and (b) parallel to the VUV polarization; (c) Kinetic energy release of D^+; (d) D^+ and e^- energy correlation map (logarithmic scale). Measurements (c) and (d) are almost identical for the two polarization configurations. The perpendicular polarization configuration was chosen for presentation. (Adapted from [44])

2.2 Machine building

2.2.1 Design goals

Many ultrafast dynamics studies focus on atomic and relatively small molecules because the energy levels become complicated very quickly as the number of atoms increase. Small molecules are normally in gas phase, so the beam line is normally designed for gas phase atoms/molecules. Some relatively big molecules have very interesting properties, such as charge migration dynamics in 2-Phenylethyl-*N*, *N*-Dimethylamine (PENNA). In order to study big molecules in liquid or solid phase, we need to construct a gas line that can be heated to transfer gas-phase big molecules.

Our design goal is to build a machine that can implement electron-ion coincidence measurements of relatively large molecules in solid or liquid state at room temperature. We attended to employ VMI and 3D detection technique to plot the 3D angular, momentum, and energy distributions of photoionized parent/fragment ions as well as electrons in coincidence with them. The VMI apparatus combined with the TOF tubes need to achieve good spatial and temporal resolutions. The temporal resolution depends on the TOF spread of ion/electron Newton sphere, the sampling rate of a digitizer, and the extent to which the jitter of laser pulses could be corrected. The spread of TOF is mainly decided by the voltages applied to ion/electron optics and the length of the TOF tube. Commercial available high-speed digitizers have different acquisition speeds, from hundreds of MSample/second to 10 GSample/second with different costs. The spatial resolution is mainly decided by the velocity mapping capability of the ion/electron optics, so the design is critical.

2.2.2 Ion/electron optics

2.2.2.1 Simion Simulation
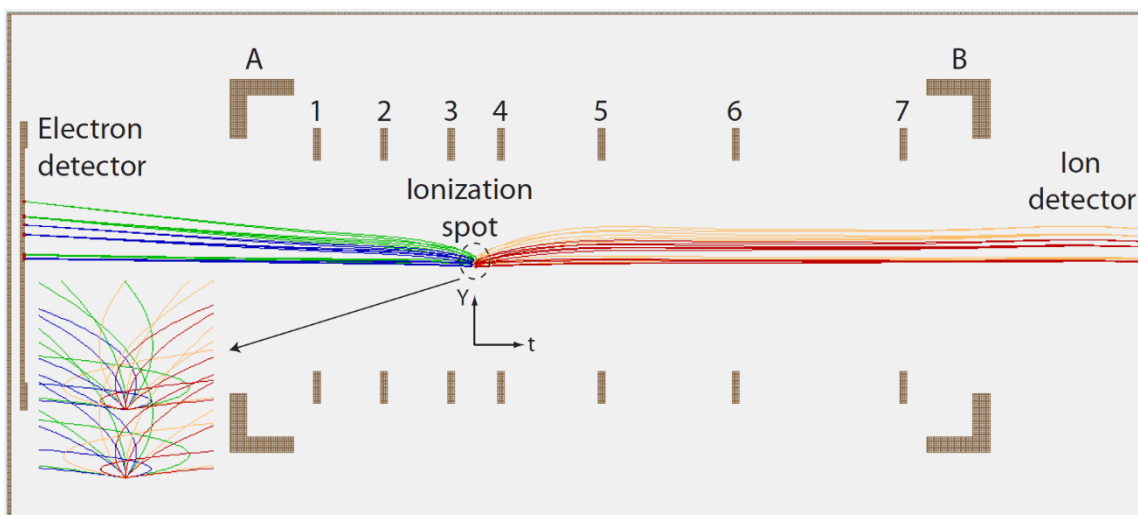
Figure 11: Simion simulation of ion-electron coincidence measurement that features two detectors at two opposite sides.

We employed an ion/electron trajectory simulation packet Simion 8.0 to design ion/electron optics. Double side VMI apparatus is relatively more difficult than single side VMI to design, because adjusting the position, inner diameter, and applied voltage of one electrode could affect the velocity focusing of both sides. It is not unusual that achieving good focusing on one side while messing up with the other side in test trials.

Ideally, ions/electrons with different velocities and trajectories should have the same focusing length, which leads to a focusing plane. When an MCP detector is placed at this plane, best velocity resolution can be obtained for ions/electrons going through different trajectories. In reality, however, the focusing lengths vary, especially for high energy electrons. Thus, this is one of the most important standards to approach when designing ion/electron optics. As shown in Figure 11, two detectors are placed at two opposite sides of the TOF tube, indicated as electron and ion detector, respectively.

The designed ion/electron optics (1-7) have different distances from one electrode to the adjacent one, which are 20 mm, 20 mm, 15 mm, 30 mm, 40 mm, and 50 mm from left to right. The ionization spot where molecules are ionized/dissociated in a strong laser field is in the center between optics 3 and 4. Different voltages are applied to these electrodes to generate an inhomogeneous electric field for velocity mapping both ions and electrons simultaneously. Electrode 7 has the lowest voltage (-2000 V) and the voltages increase gradually on each electrode. Electrode 1 is grounded (0 V). With the electric field generated by this voltage settings, electrons fly from low potential to high potential and are accelerated toward the electron detector; oppositely, ions will be accelerated toward the ion detector. Blue and green colors represent electron trajectories with initial kinetic energy

(KE) of 1.4 and 3.5 eV, respectively. Red and yellow colors are the ion trajectories with initial kinetic energy (KE) of 1.4 and 3.5 eV. To show the velocity focusing ability of this ion/electron optics, we put the ion/electron origin positions 2 mm away from each other, as shown in the inset of Figure 11. At each origin position, there are 10 ions and 10 electrons pointing at 5 angles: 10°, 50°, 90°, 130°, and 170°. Five ions have initial KE 1.4 eV (red) and five ions have initial KE 3.1 (eV). Likewise, blue and green colors are electrons at 1.4 and 3.1 eV. When these particles arrive at two detectors, the ions/electrons originating from different positions but pointing toward the same angles are focused to the same spots on the detectors. Particles with the same KE but towards different direction are not focused to the same Y position because of the different initial momenta alone Y-axes. The different t momenta decide that they arrive on the detectors at different time. If plotting the Yt distribution, particles with the same initial KE form a ring. Since only Y distribution is shown here, it is like a ring in XY plane being projected on a detector, so particles pointing at different directions do not come all together.

2.2.2.2 Materials for UHV

Electrode plates were made from oxygen-free copper sheets with an outer diameter of 82 mm and an inner diameter of 56 mm. The two supporting rings and the four rods were made from stainless steel 304 and 316. Some metal elements need to be avoided due to their high vapor pressure, such as Cadmium, Zinc, Magnesium, Lead, Sulfur, and phosphorus. For example, the compositions of S and P in stainless steel 303 are 0.2% and 0.15%, but they are 0.045% and 0.03% in other grades of stainless steel, so grade 303 is generally avoided in UHV application. Some small parts were made from aluminum (alloy 6063) because it is much easier to machine than stainless steel. Macor is a machinable

ceramic material, which does not have porosity and will not outgas and deform at high temperature. It is also a good insulating material when high voltages are applied, so it was used as insulating bars to assemble the electrodes together. Even though PEEK (polyetheretherketone) is a kind of plastic, it is a high-performance engineering material with good properties, such as high strength, easy-to-machine, and resistance to harsh chemicals. At the same time, it has relatively low outgassing value in UHV environment.

2.2.2.3 Constructing ion/electron optics

The inner diameter of the main chamber is ~ 6.5", so the supporting rings (A and B in Figure 11) to hold the ion optics together were made of Φ 4-3/8". The ion/electron optics was assembled in the way introduced by Ryazanov et al.[38] The copper electrodes were inserted into the shallow groves (~2 mm in width and 1.5 mm in depth) in four ceramic bars to clamp the electrodes. The two stainless steel supporting rings (A and B) are connected by four Φ¼" stainless steel rods. These rods push the pins in supporting ring A against the chamber wall. The other sides of these rods are threaded and are secured by 4 nuts on ring B side. Four set screws with peek heads go through the wall of ring B to push against the chamber wall. The ion optics is then axially centered in the main chamber. A short TOF length (~10 cm) was adopted on electron side to allow detection of high-energy electrons.
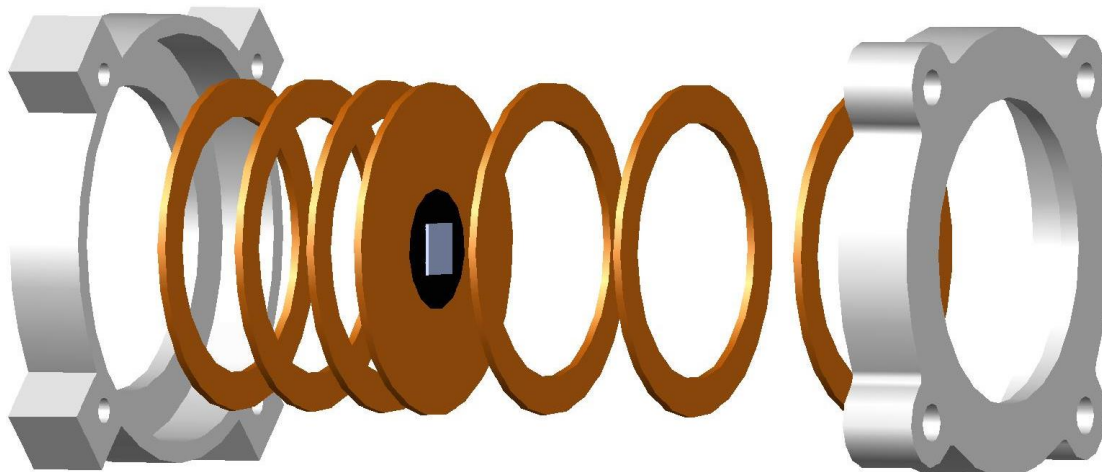
Figure 12: The assembly of ion/electron optics.

2.2.3 3D momentum-imaging detection system

2.2.3.1 Microchannel plates (MCPs) / phosphor screen detector

Microchannel plate (MCP) is an assembly of millions of micro glass tubes that work as secondary electron multipliers. It is widely used to image particles that are projected to the detector. When an incident particle hit the wall of one microtube, an electron will be emitted from the wall and accelerated by the electric field applied to the MCP to hit the tube wall again, which can generate more secondary electrons. By repeating this process, one incident particle could give rise to thousands of secondary electrons at the exit of the glass tube. Two MCPs are usually stacked together in experiments (sometimes even three) to achieve better multiplication of an incident particle. The secondary electron pulse from the first MCP could hit several glass tubes on the second MCP and further intensify the signal. The number of generated secondary electrons from the output of the second MCP can reach 10^8 or even higher (Data from Del Mar Photonics). Following MCPs, a phosphor screen could be utilized to execute imaging function by generating photons when

secondary electrons from MCPs hit it. A camera can be placed after the phosphor screen to capture the position of a hitting event.
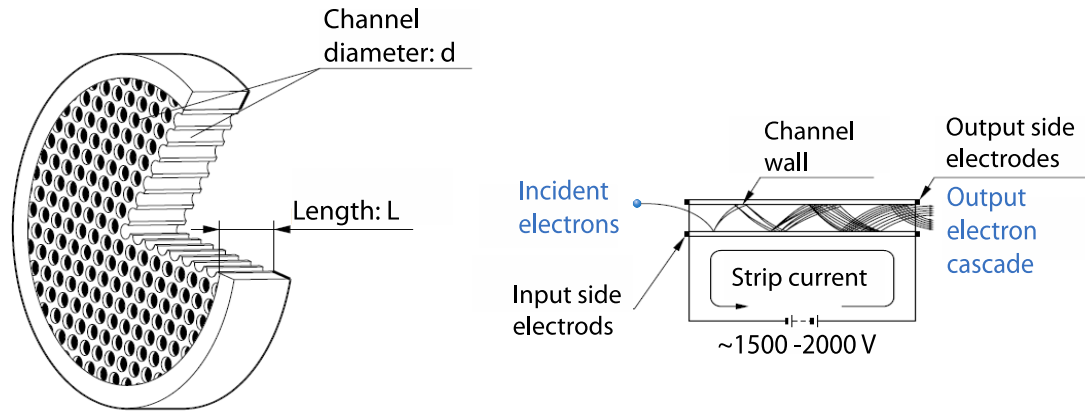
Figure 13: MCPs and the schematic of electron multiplication process inside one microtube in an MCP (adapted and modifies from Hamamatsu Photonics).

CCD (charge-coupled device) cameras normally have low frame rates. They can match with lasers running at a relatively low repetition rate, such as 10 Hz. An ultrafast Ti: Sapphire laser, however, normally runs in the range of 1-100 kHZ. Normal CMOS cameras can have maximum frame rate up to several KHZ, so they can remove the barrier of frame rate, making high-speed imaging possible.

2.2.3.2 Scheme of 3D imaging detection system

The 3D detection system that was developed recently in our lab consists of an MCP (microchannel plate)/phosphor screen detector, a fast frame complementary metal-oxide semiconductors (CMOS) camera, and a high-speed digitizer. After charged particles are accelerated by electrodes and fly through a short field-free time-of-flight (TOF) region, they hit on the MCP detector and generate bright flashes on the phosphor screen. The COMS camera records the position of these flashes on the detector (x, y coordinates) through centroiding algorithm; the corresponding electric waveforms generated by the hitting events go through a signal-decoupling box and then are picked up by the digitizer

to provide TOF information. The post-analysis coincidence algorithm gives 3 coordinates (x, y, t) that enable the detection system to measure the 3D momentum and angular distribution of electrons/ions simultaneously. The schematic of 3D momentum-imaging detection system is shown in Figure 14. If only one particle hit the detector within a laser cycle, there is no doubt to associate the three coordinates: x, y coordinates from the camera and t from the digitizer. For multiple-hitting events, it has been demonstrated that the camera pixel intensity and the digitizer waveform amplitude have a positive linear correlation,[45-46] so brighter image pixels correspond to stronger digitizer waveform amplitude.

The 3D detection system has very good spatial (< 1 mm) and time resolution (32 ps), so it can record electron TOF with high time resolution and the electron Newton sphere can be sliced along TOF axis very easily in the post-analysis algorithm. [46] Figure 15 shows the electron slices along the TOF axis of Xe arising from strong field ionization. Each slice has a time duration of 32 ps. The observed shortest dead time is 0.64 ns by applying a new peak analysis algorithm to the digitizer waveform. [47] The developed 3D detection system has lower cost than delay line detectors as well.
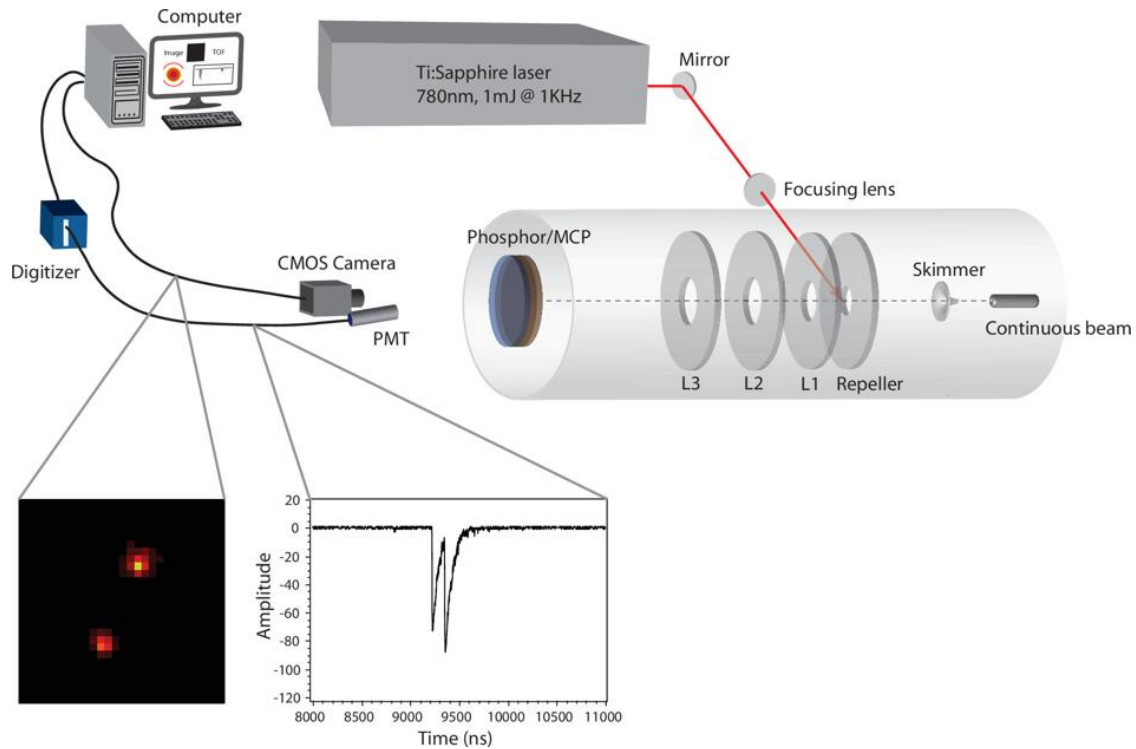
Figure 14:   Schematic of 3D momentum-imaging detection system. [45]

2D MCP detector has been gated to obtain the sliced VMI,[36-38] because a central slice of ion cloud gives a sharper feature of angle and momentum distributions. This method, however, can only be applied to ions because the TOF of ions extends long enough (tens to hundreds of µs) to be gated to obtain the center slice. Electron mass is much lighter than ions and thus electrons can be accelerated to much higher velocities in the electric field generated by the ion/electron optics. As a result, the TOF of electrons is much shorter than ions, in the range of several nanoseconds. There is no way to gate electron cloud with such short TOF. Comparing with the conventional slicing VMI, the 3D detection system has very good time resolution (~30 ps) for electrons and records the whole Newton sphere[46], which can be sliced in XY plane (parallel to detector) or the YZ plane (perpendicular to the detector) freely at different positions, not only the center slice through gating the detector in conventional slicing VMI. Because the good time resolution that the

3D detection system can achieve, this method can also be applied to electrons, while conventional slicing VMI only works for ions.
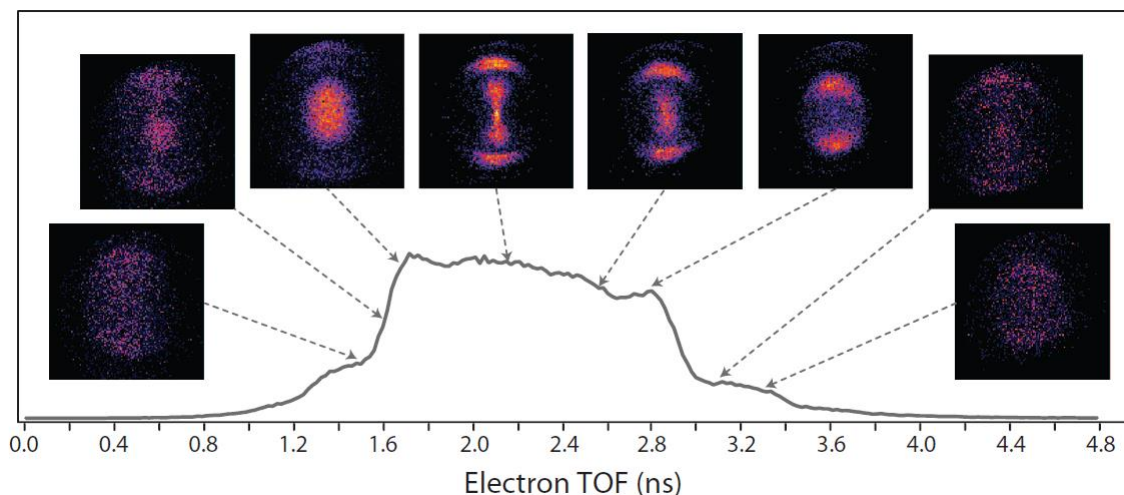
Figure 15: Electron slices along the TOF axis arising from strong field ionization of Xe.[46]

The high-speed digitizer was purchased from National Instruments and model number is PXIe 5162. The maximum sampling rate of this digitizer is 5 GHz. One CMOS camera was bought from Basler with model number of acA640-750μm. The other CMOS camera was from XIMEA brand with model number of MQ013MG.

2.2.4 Gas line

Condensed phase sample is placed in a bubbler and can be heated outside of the chamber. If the temperature of the gas line is too low, the sample will condense again before it enters the main chamber. We chose a flange with Cu feedthrough (1/4" outer diameter) and this Cu tube is isolated from the stainless-steel entity by a ceramic tube, so it becomes easier to heat the tube without allowing too much heat to dissipate into the flange. Inside the source chamber, an aluminum tube is used because it has very good thermal conductivity. A skimmer with 0.5 mm orifice is installed between the main

chamber and the source chamber. After molecules are ejected from the gas nozzle (diameter 20 µm) and expanded, the skimmer extracts only the center part of the gas beam.

2.2.5 Mounting surface samples

As shown in Figure 12, the 4th plate from the left has a threaded hole in the center with a diameter of Φ 30 mm. The surface sample could be loaded on a stainless plate (Φ 30 mm) that also has threads on the side to be installed on the 4th electrode. This allows the machine to study gas-phase molecular dynamics as well as surface dynamics without modifying the machine too much. With this layout, we can adopt both transmission and reflection geometry to carry out surface experiments. When implementing a gas phase experiment, we just need to remove the surface sample.

2.2.6 Magnetic coils

Two stacks of Helmholtz coils are placed outside of the main chamber to generate a weak magnetic field, indicated in Figure 16. The flux of the magnetic field points oppositely to the earth magnetic (in microtesla range) so that they can cancel out. The reason for these coils is that electrons are very light ($9.10938356 \times 10^{-31}$ kg) and can be deflected by the earth magnetic field when flying through TOF region.

2.2.7 Baking the chamber

The main chamber is heated by rubber tapes to get ultra-high vacuum (UHV, $\sim 10^{-9}$ torr). At 10^{-8} torr, the residue gas in a vacuum is mainly water. It becomes "sticky" to the chamber wall and is hard for turbo molecular pumps to pump out. Heating the chamber is critical for lowering the vacuum further, so UHV could be reached.
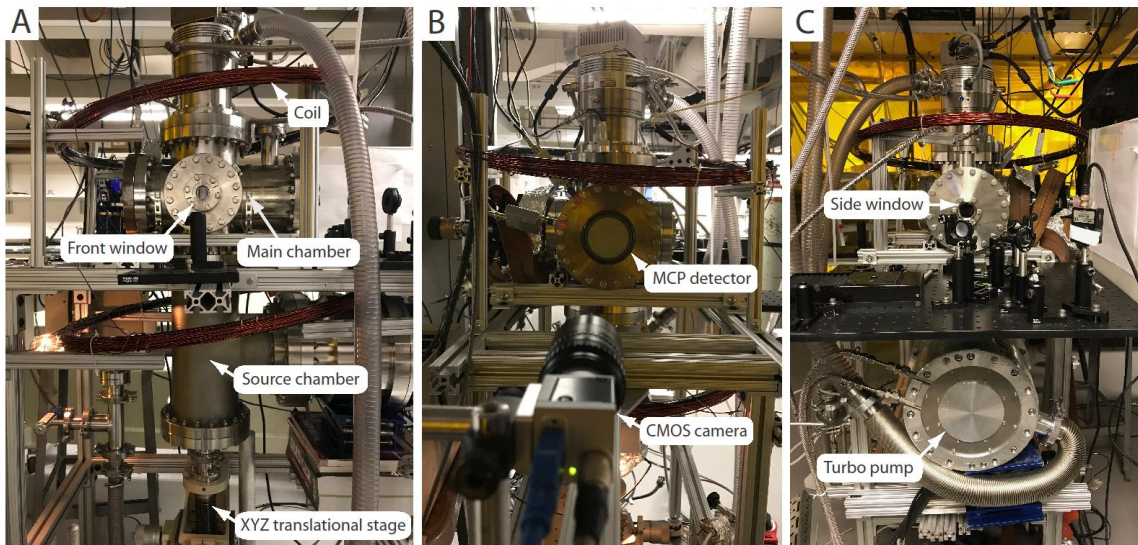
Figure 16: The front view and two side views of the built machine.

Figure 16 shows the built machine with main parts being indicated. The front window is to send laser beam into the main chamber perpendicular to the molecular beam and the TOF axis. Ionization spot is shown in Figure 11. Side window allows a laser beam to be sent into the chamber normal to a surface sample. XYZ translation stage under the source chamber allows adjusting the molecular beam line finely. In Figure 16, only one CMOS camera is showed. The other one is placed after this camera, slightly deviated from the detector normal direction.

2.3 Test the machine functioning

2.3.1 Test with methyl iodide

After finishing building the machine, the first task should be testing whether it can function properly and correctly. The first polyatomic molecule we chose is methyl iodide, which is a well-studied molecule. Exposure to intense femtosecond laser field could cause methyl iodide to lose more than one electrons and subsequently dissociate through Coulomb explosion ($CH_3I^{n+} \rightarrow CH_3^{p+} + I^{q+}$, n=p+q). Velocity distributions of fragment ions from different dissociation channels were plotted and the energy distributions are analyzed.

Liu et. al. found that the KERs of the dissociated ion pairs are independent of the laser intensity and the measured KERs are much lower than the calculated values. [48] They attributed this to the meta-stable state in CH_3I^{2+} and the covalent forces between the two fragments. They also found that the KER of CH_3I^{3+} is surprisingly lower than that of CH_3I^{2+}, and they proposed that the distance between C and I moved apart further in the transition from CH_3I^{3+} to CH_3I^{2+}. Here, we applied mid-intensity strong field ionization on this molecule to test the velocity mapping capability of the machine and to calibrate the parameters that are needed to calculate momentum and energy distribution of parent and fragment ions.

At laser intensity higher than 8×10^{13} W/cm^2, field ionization takes place. The laser intensity was about 10^{13} W/cm^2, so multiphoton ionization was the dominant pathway. It takes 7 photons to produce parent ion with two spin-orbit states of $^2E_{3/2}$ and $^2E_{1/2}$ [49], but takes one or two more photons to go through ionization barriers that lead to ionic products, so in the mass spectrum, parent ion had much high intensity than CH_3^+ and I^+. There were three possible dissociation pathways at laser intensity for multiphoton dissociation:

$CH_3I + 8h\nu \rightarrow CH_3^+ + I\ (^2P_{3/2}) + e^-$ 12.18 eV (1)

$CH_3I + 9h\nu \rightarrow CH_3 + I^+\ (^3P_2) + e^-$ 12.90 eV (2)

$CH_3I + 9h\nu \rightarrow CH_3^+ + I^*(^2P_{1/2}) + e^-$ 13.12 eV (3)
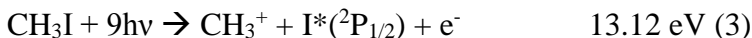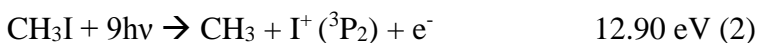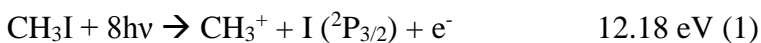
The potential for channel 1 is 12.18 eV and 13.12 for channel 2, and it takes 8 or 9 photons to pass through these two potentials and obtain the dissociated products.
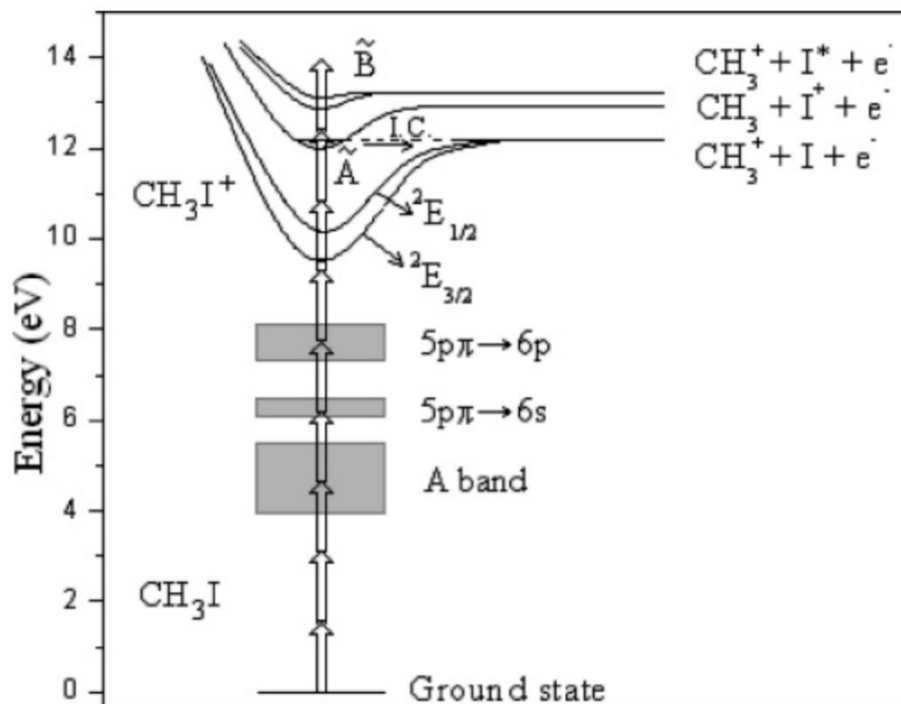
Figure 17: Energetic diagram of CH_3I, CH_3I^+, and following dissociation channels. (Adapted from reference [49])

In our test, the laser polarization was along the TOF axis, perpendicular the detector (XY) plane, so the distribution is isotropic in XY plane, as shown in Figure 18 (a). In Figure 18 (b), the velocity distribution of CH_3^+ has three sub-structures: the center ellipse, two half-spherical distributions, and an outside ring. The intensity of the last two structures is much lower than that of the center ellipse, so the center is saturated (in this color map) to show all three structures clearly. A slice was taken with a thickness of 40 pixels (~ 7 mm) along the X-axis to show the two hemispherical structures more clearly. The outside ring is from double ionization, which has lager kinetic release, ~4.3 eV. The center elliptical shape distribution is from single ionization, through channel 1 described above. The two hemispherical structures may arise from dissociation channel 3 that leads to CH_3^+ and $I^*(^2P_{1/2})$. This channel has a potential barrier of 13.12 eV and it takes 9 photons to

overcome this barrier. The kinetic energy release should be around ~1 eV. The calibrated kinetic energy release of CH_3^+ has very high intensity around zero, as well as two small peaks at ~1.35 eV and ~4.3 eV. These three peaks should correspond to the three sub-structures in the velocity distribution shown in Figure 18 (b).
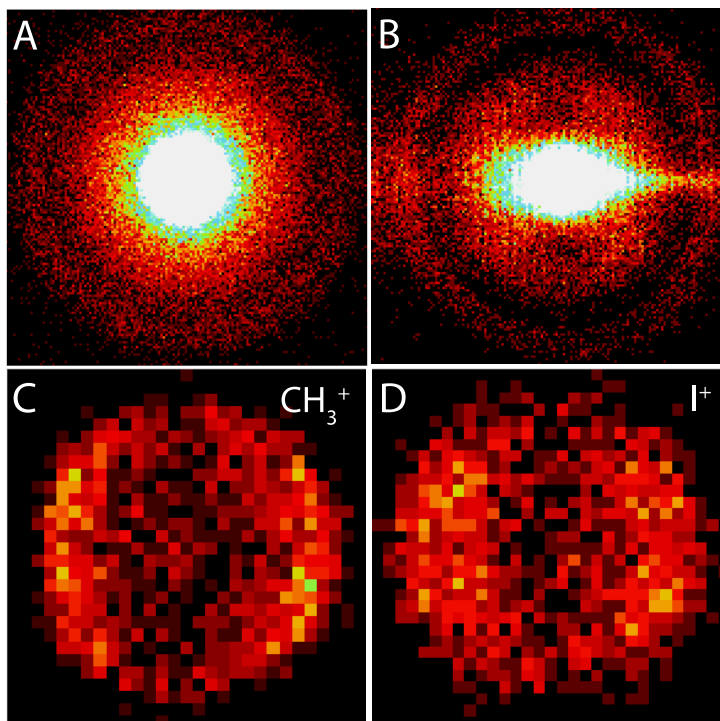
Figure 18:   Velocity and momentum distribution of products from strong field ionization of CH_3I. (a) XY velocity distribution of CH_3^+ and I^+. (b) Slice of YZ velocity distribution of CH_3^+. (c). YZ momentum distribution of CH_3^+ from double ionization. (d). YZ momentum distribution of I^+ from double ionization.

Double ionization also took place at the employed laser intensity. The diagonal structure for CH_3^+ (y-axis) and I^+ (x-axis) was shown in Figure 19 (a), indicating the coincidence between them in double ionization. The momentum distributions of CH_3^+ and I^+ arising from double ionization are shown in Figure 18 (c) and (d), which are in the plane perpendicular to the detector. The laser polarization direction was along the horizontal axis. Both CH_3^+ and I^+ ions have stronger intensity on the left and right sides of the sphere due

to the laser polarization. The difference is that the CH_3^+ has a narrower distribution than I^+. This may because the TOF of I^+ is much longer than CH_3^+, the Newton sphere and velocity distribution along the TOF axis spreads more before it arrives at the detector. The total kinetic energy of CH_3^+ and I^+ ion pairs was calibrated according to the previous results reported in reference [45], shown in Figure 19 (b). Two peaks are center around 4.37 and 5.13 eV, in good agreement with the previous results.
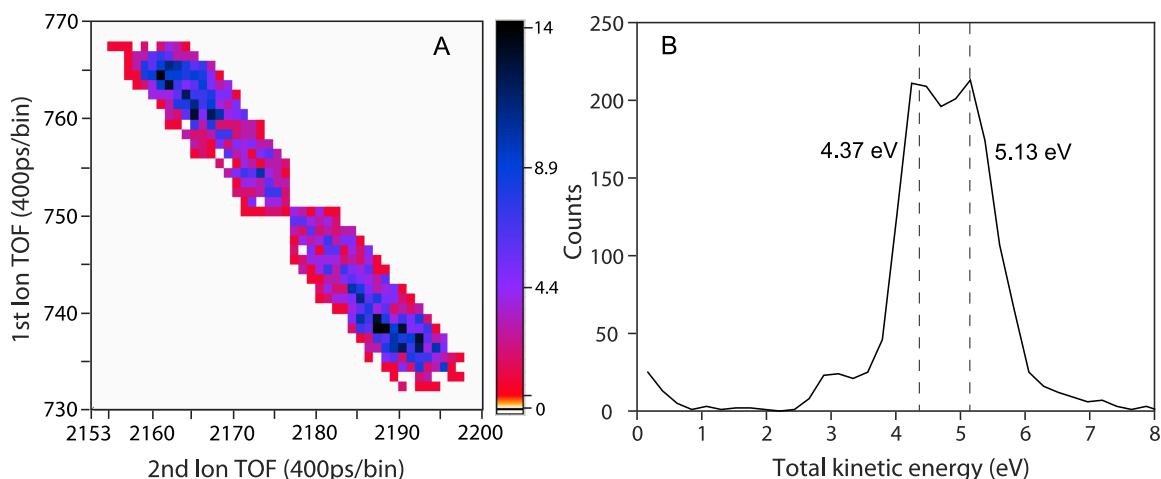
Figure 19:   (a). 2D TOF plot. (b). Total kinetic energy release of CH_3^+ and I^+ from double ionization.

2.3.2 Test with argon

We also tested the machine functioning through strong field ionization of argon. Electron distributions in Figure 20 (a) were collected at voltages: -100V, -70V, 0V, and -300V, -280V, -150V, and 0V for electron distributions in Figure 20 (b). Since there is no velocity mapping effect along the TOF axis, the ATI peaks are clearer to observe at low voltages. As shown in Figure 20 (a), there are up to 5 ATI peaks on the left side. We attempted to check the general effect of electric field applied, so the voltage settings were not fully optimized in Figure 20 (a) and it caused a little bit distortion on the right side. The electron TOF we used was short (~ 10 cm) comparing with traditional TOF instruments,

which normally have TOF tubes around several feet. The voltages on lens two and three needed to be raised (smaller voltage gradient) to shorten the focal length of electrons. For the voltage settings we used in Figure 20 (a), electrons with initial velocity against the detector have larger Y value (along perpendicular direction) than those towards the detector, especially at higher initial KE. The counts before and after time zero are a little different: 377531 and 337150. Besides, there is a cutoff on the right side. These suggest that some high-energy electrons might collide on the repeller. Another possibility is that the voltages applied was low, so the Newton sphere grew to large size, close to the edge of the openings, where equipotential lines are slightly distorted. Electrons on the right side of the sphere fly oppositely to the detector and then are reversed back. Their trajectories are closer to the edge than the forward electrons and might be accelerated more along both TOF and transverse directions due to the distortion of the equipotential lines. The electron distribution in Figure 20 (b) was collected at higher voltages.
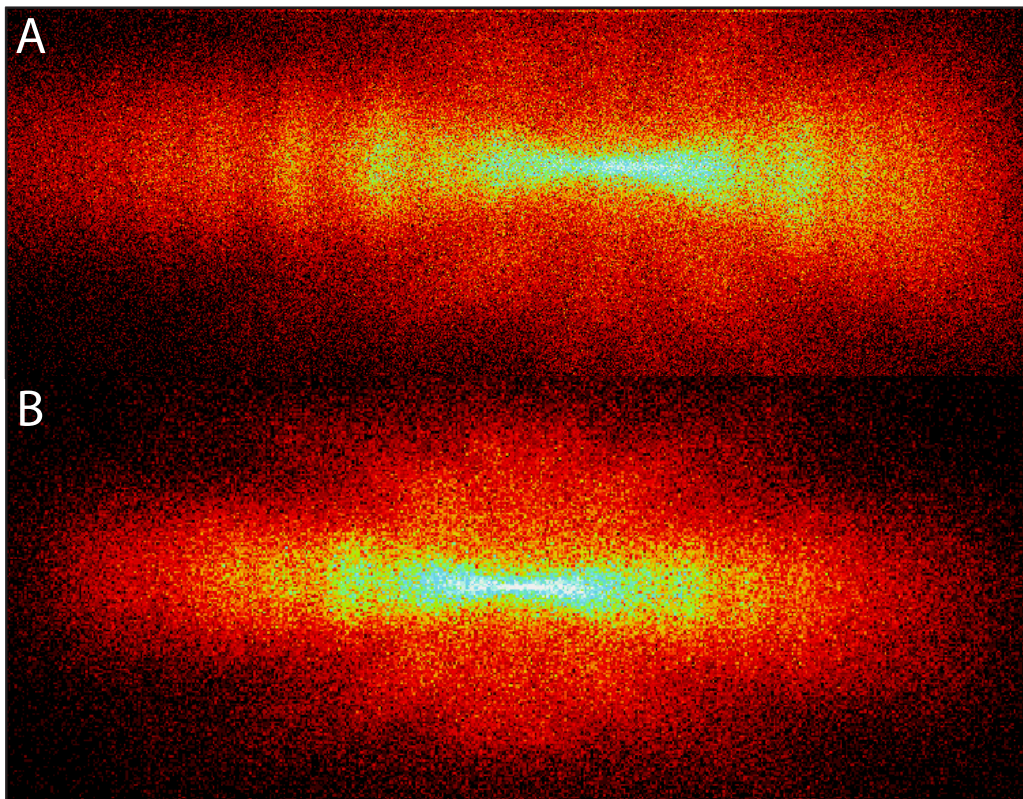
Figure 20:   YZ images at different voltage settings on electrodes.

The momentum distributions in detector plane are displayed in Figure 21 (a) and (b). The counts are 537008 and 420245, respectively. Electrons in Figure 21 (a) were collected at voltage settings: L1 = -300V, L2 = -280V, L3 = -150V, and L4 = 0V. Then we kept the voltage on the repeller same and decreased the voltages on lens 2 and lens 3 to -290V and -180V, to check the effect of fine voltage tuning on VMI. The electron distributions are similar at different VMI conditions, but minor differences are still observable. The ATI peaks in Figure 21 (b) are narrower than those in (a), especially the leftmost two peaks, which means lower voltage gradient could lead to better focusing resolution for electrons with relative-high KEs. These illustrated the fine-tuning of the velocity mapping resolution by setting voltages on electrodes.
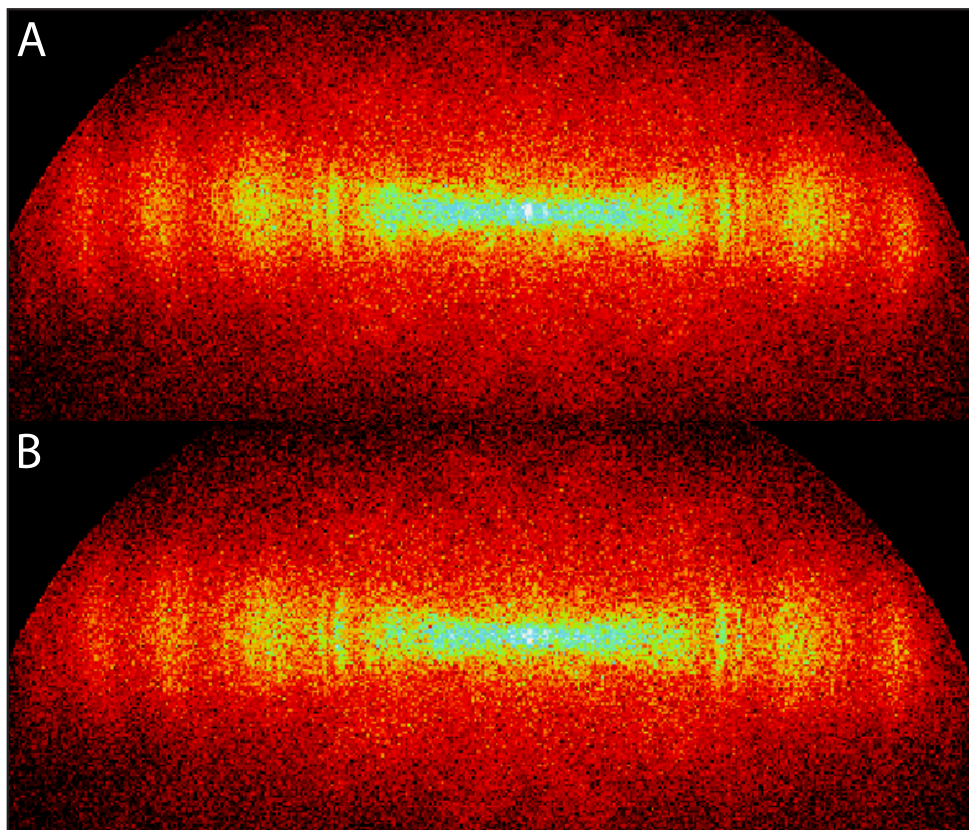
Figure 21: XY images of electron distributions of Ar at different voltage settings. Laser polarization is perpendicular to the TOF axis.

CHAPTER 3. PHOTOIONIZATION AND DISSOCIATION DYNAMICS OF GAS PHASE MOLECULES

3.1 Exploring double ionization/dissociation pathways and photoelectron circular dichroism of camphor enantiomers

3.1.1 Introduction

When chiral molecules are ionized in circularly polarized laser field, photoelectrons emitted forward and backward relative to the laser propagation direction tend to show an asymmetric distribution, which is called photoelectron circular dichroism (PECD). Asymmetry in photoelectron distribution from chiral bromocamphor molecules has been studied by employing circularly polarized vacuum ultraviolet (VUV) synchrotron beam. [50] In this study, two spectrometers were placed oppositely and had a 55° angle with the VUV beam line to collect forward and backward photoelectrons. A forward-backward asymmetry was observed in photoelectron angular distribution (PAD), even though bromocamphor enantiomers were unoriented. This was explained by that these chiral molecules lack mirror symmetry, and the dichroic effect still existed after averaging over all molecular orientations. Later, VMI technique was employed to obtain the full angular distribution of photoelectrons from chiral molecules. [51] These studies explored the photoelectrons stemming from the one-photon ionization of chiral molecules by VUV beam. Later, femtosecond intense laser field was used to examine the resonance enhanced multiphoton ionization of small chiral molecules including camphor, bromocamphor, and fenchone. ATI signatures were observed in PAD. [52-53] Quasi-circular HHG from the interaction of elliptical 410 nm pulses and SF_6 molecules was also demonstrated by inducing one-photon ionization of fenchone enantiomers and exploring the photoelectron

circular dichroism.[54] Beaulieu et. al. implemented attosecond-resolved self-referenced molecular interferometry to explore the asymmetry photoemission from chiral molecular potential of camphor enantiomers. [55] The interferometry was achieved by using a 400-nm UV field as pump beam and an 800-nm MIR field as probe beam. Sidebands could be generated when a state excited by UV photons absorbs or emits an IR photon, which is similar to the RABBIT strategy. By adjusting the polarization of the UV and IR beams (one was chosen to be circular polarized and the other one was linear polarized), they measured the forward/backward asymmetry in the Wigner time delays to be several attoseconds in direct ionization. The electron wave packet is strongly asymmetric in autoionization resonance vicinity.

Fragmentation of camphor and a double ionization channel leading to an ion pair of $C_2H_3^+$ and $C_3H_3^+$ were examined by Castilho et. al. with different synchrotron radiations (270 eV and 300 eV) and electron ionization source (70 eV).[56]

Here, we studied the strong field ionization of camphor in ion mode first to study the ionization/dissociation dynamics. Then we employed quasi-circularly and elliptically polarized laser to explore whether the asymmetric electron distribution can be observed along propagation direction and in polarization plane.

3.1.2 Ionization and dissociation dynamics of camphor

3.1.2.1 Experimental details

The amplified ultrashort pulses from Ti:sapphire laser was linearly polarized for ion mode, and circularly and elliptically polarized for electron mode. The wavelength was 800 nm and the laser intensity was around 1×10^{13} W/cm^2. (1S)-(-)-camphor and (1R)-(+)-camphor were purchased from Sigma, and the enantiomer purity is higher than 95%. The

sample was heated to ~40°C to vaporize the solid-state sample. Helium was employed as carrier gas to send camphor samples into the UHV main chamber. The gas jet was heated to about 70°C to guarantee the camphor molecules were in gas phase in molecular beam line until they were sprayed into the main chamber.

3.1.2.2 Results

The mass spectrum of R-camphor arising from mid-intensity strong field ionization is shown in Figure 22. The yield of camphor parent ion was the highest, indicating parent ions were relatively stable at this laser intensity. The mass 41 fragment is $C_3H_5^+$ from single ionization of camphor. It has comparable peak intensity with that of the parent ion. Fragments with relatively high intensities, such as mass 108, 95, 81, 69, all stem from single ionization, with little kinetic energy release. The identifications of the structures of these fragments are listed in Table 1. From the mass spectrum, it is straightforward that camphor molecules were highly fragmented through many different single and double dissociation pathways even in mid-intensity field.
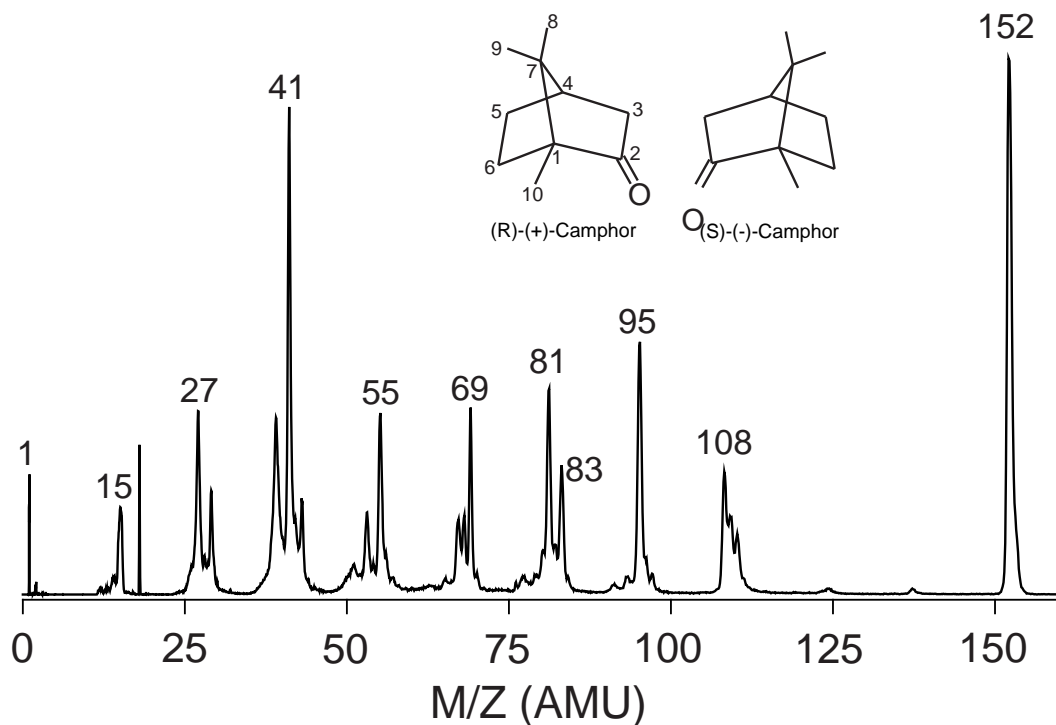
Figure 22: Mass spectrum of S-camphor in mid-intensity strong field ionization.

m/z	TOF (bin)	Fragments	Yield relative to parent ion
1	180	H^+	19.5
2	257.5	H_2^+	2.5
14	695.5	CH_2^+	8.9
15	720.5	CH_3^+	36.7
27	968.5	$C_2H_3^+$	60.5
28	985.5	CO^+	11.3
29	1003.5	$HCO^+ / C_2H_5^+$	29.0
39	1164.5	$C_3H_3^+$	79.8
40	1181.5	$C_3H_4^+$	11.0
41	1194.5	$C_3H_5^+$	109.3
42	1207.5	$C_2H_2O^+$	17.0
43	1223.5	$C_2H_3O^+ / C_3H_7^+$	22.6
51	1332.5	$C_4H_3^+$	20.1
53	1359.5	$C_4H_5^+$	25.1
55	1385.5	$C_4H_7^+$	41.9
67	1529.5	$C_4H_3O^+ / C_5H_7^+$	18.8
68	1540.5	$C_4H_4O^+ / C_5H_8^+$	14.8
69	1551.5	$C_4H_5O^+ / C_5H_9^+$	29.3
81	1681.5	$C_6H_9^+ / C_5H_5O^+$	41.2

83	1702.5	$C_6H_{11}^+$/ $C_5H_7O^+$	29.4
95	1822.5	$C_7H_{11}^+$ / $C_6H_7O^+$	53.4
108	1943.5	$C_8H_{12}^+$ / $C_7H_8O^+$	20.0
109	1952.5	$C_8H_{13}^+$ / $C_7H_9O^+$	17.6
110	1961.5	$C_8H_{14}^+$ / $C_7H_{10}O^+$	13.4
152	2306.5	$C_{10}H_{16}O^+$	100.0

Table 1: Fragmentation yield of S-camphor in mid-intensity strong field ionization.

To confirm the fragments arising from double ionization and dissociation of camphor, we plotted the 2D TOF intensity graph, i.e. photoion-photoion coincidence map, shown in Figure 23. The insets show the zoomed-in diagonal signatures of ion pairs arising from double ionization and dissociation. The ion pair $C_2H_3^+$ (27) + $C_3H_3^+$(39) has the strongest coincidence intensity, shown in Figure 23 inset I. Castilho et. al. also observed this double ionization feature when exploiting electron and synchrotron radiation sources to ionize camphor molecule.[56] They proposed a dissociation mechanism for this double ionization leading to the generation of ion fragments $C_2H_3^+$ and $C_3H_3^+$. They assumed two electrons are removed from bond C1-C2 and the methyl group C8 transferred to C2 and left a positive charge at C7 (the numbers of carbon atoms are labeled in Figure 22). Carbon bond cleavage happened at C4-C7 and C5-C6, and a new bond was formed between C6 and C7, which lead to a neutral C_5H_8O fragment and $C_5H_8^+$ cation. The cation $C_5H_8^+$ dissociated into $C_3H_3^+$ and $C_2H_5^+$. The $C_2H_5^+$ cation then became $C_2H_3^+$ by losing an H_2.

Besides this ion pair, double ionization of camphor could lead to other ion pairs that have not been reported to our best knowledge. $C_3H_3^+$ and $C_3H_5^+$ is another ion pair from double ionization that has relatively strong intensity and is shown in Figure 23 inset II. The diagonal structure of ion pair HCO^+ (29) + $C_7H_{11}^+$(95) is shown in Figure 23 inset III. Besides these ion pairs with relative strong intensity, there are much more coincidence features with relatively low intensity but are clear to observe when zooming in the 2D TOF

intensity graph. These coincidence features are checked very carefully by rows of the 2D graph and listed below. Ion pairs $CH_2^+(14) + C_2H_3^+$ (27) and $CH_2^+(27) + C_3H_3^+(39)$ with very low intensity showed up at TOF 695.5 (y axis). Diagonal structures of ion pairs $CH_3^+ + C_2H_3^+$, $CH_3^+ + HCO^+$ (very weak), $CH_3^+ + C_3H_3^+$, $CH_3^+ + C_3H_5^+$, $CH_3^+ + C_3H_5^+$ (very weak), $CH_3^+ +$ mass 77, $CH_3^+ +$ mass 79, and $CH_3^+ +$ mass 91 were observed at TOF 720.5. Besides, ion pairs $C_2H_3^+$ (27) + $C_3H_5^+(29)$ (very weak), $C_2H_3^+$ (27) + $C_3H_5^+(41)$, $C_2H_3^+$ (27) + 1333, and $C_2H_3^+$ (27) + $C_4H_5^+(53)$ were also observed at TOF 968.5. Ion pairs HCO^+ (29) + $C_3H_3^+(39)$, HCO^+ (29) + $C_3H_5^+(41)$, HCO^+ (29) + $C_4H_5^+(53)$, HCO^+ (29) + $C_4H_7^+(55)$, HCO^+ (29) + $C_6H_9^+(81)$, and HCO^+ (29) + $C_7H_{11}^+(95)$ are clear to observe at TOF 1003.5. Further, ion pairs $C_3H_3^+$ (39) + $C_3H_5^+(41)$, $C_3H_3^+$ (39) + 1333 (very weak), $C_3H_3^+$ (39) + $C_4H_5^+(53)$, and $C_3H_3^+$ (39) + $C_4H_7^+(53)$ have clear diagonal structures at TOF 1164.5. Ion pair $C_4H_7^+(53) + C_4H_5O^+(69)$ is also observable.

Then we deduced the possible dissociation pathways leading to these ion pairs. We began with ion pairs that have larger total mass due to the loss of small neutral fragments, because it is relatively easier to deduce the structure of the neutral fragments and then ion pairs. For ion pair mass 29 and mass 95, the lost mass is 28, which could be C_2H_4 or CO. There is only one oxygen atom in a camphor molecule. It can only appear in one of the three fragments. The three possible dissociation pathways are:

$C_{10}H_{16}O \rightarrow C_2H_5^+$ (29) + $C_7H_{11}^+$ (95) + CO (28)   (1)

$C_{10}H_{16}O \rightarrow HCO^+$ (29) + $C_7H_{11}^+$ (95) + C_2H_4 (28)   (2)

$C_{10}H_{16}O \rightarrow C_2H_5^+$ (29) + $C_6H_7O^+$ (95) + C_2H_4 (28)   (3)
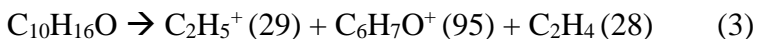
The different bond strengths in camphor could give hint on which bond is relatively weak and easier to break. Castilho et. al. calculated the Wiberg bond indices for camphor

neutral molecule, monocation, and dication with density function theory B3LYP and 6-311+G(d, p) basis set.[56] The bond indices are close to zero for C1-C10 in camphor monocation and C1-C2 in dication, indicating these are the weakest bonds and electron(s) are most likely to be removed from them in single and double ionization events. For these three possible dissociation pathways, the first step would be that two electrons are removed from C1-C2 bond and leave a positive charge on C1 and C2. For the dissociation pathway (1), the electron pair forming C2-C3 bond moved to C2 and formed a new bond between C2 and O, leading to a neutral fragment CO. A methyl group (C9) transfer to C3 that have a positive charge and electron pair forming C3-C4 bond attack the positive charge C7, forming a double bond between C4 and C7. This results in two charged fragments $C_2H_5^+$ and $C_7H_{11}^+$ in pathway (1). For the dissociation pathway (2), proton transfer could happen because there are electron pairs on oxygen. The dissociation process is similar to the pathway (3), but a proton transfer happens in the process, which leads to a charged fragment HCO^+ and neutral fragment C_2H_4. The fragment $C_7H_{11}^+$ is not affected, which means the proton is from either C3 or the transferred methyl group C9. There is no obvious dissociation pathway that could lead to products $C_2H_5^+$ (29) + $C_6H_7O^+$ (95) + C_2H_4 (28), so pathway (3) is ruled out.
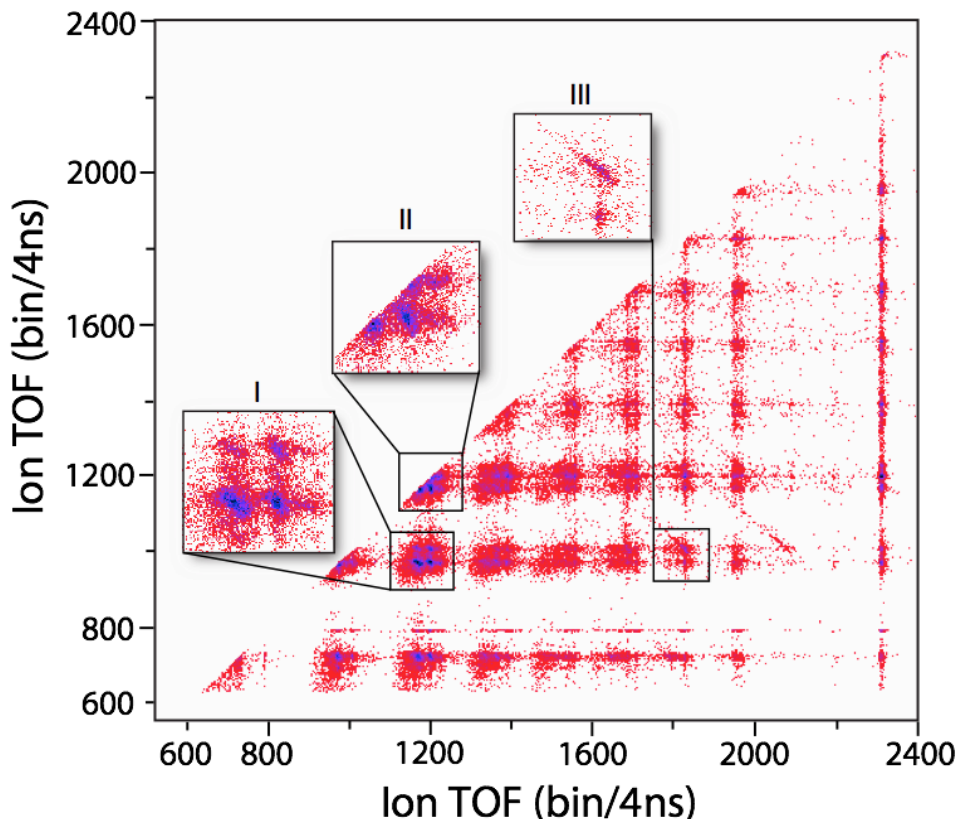
Figure 23: 2D TOF of S-camphor, i.e. photoion-photoion coincidence map. Blue color represents higher intensity than red.

3.1.3 Electron distributions for R and S camphor enantiomers

After studying the single and double ionization/dissociation dynamics of camphor in ion mode, we switched to electron mode to examine photoelectron angular distributions. We attempted to find the asymmetric distribution of forward and backward scattered photoelectrons relative to the propagation of circularly polarized laser with unaligned camphor enantiomers. In the experiment, the laser propagation direction is parallel to the horizontal axis in detector, which is defined as XY plane. The difference between 2D projection images of different enantiomers (R(+) − S(-)) with a fixed helicity was not obvious enough. We also tried ionizing one enantiomer with left and right circular

polarized light, but still did not observe obvious difference between those XY images (these XY images are not shown here).

We then considered the possible asymmetry in the laser polarization plane. Chiral enantiomers have chiral Coulomb potentials. The ionized electrons might interact with these chiral potentials and result in asymmetric distribution in the laser polarization plane.
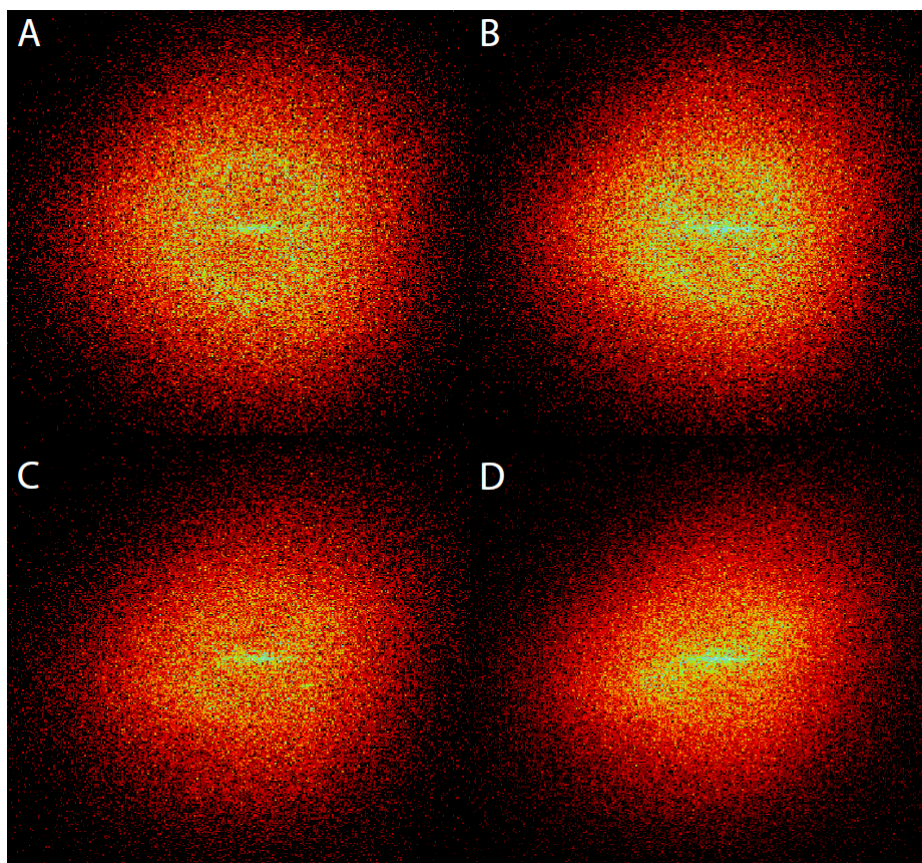
Figure 24: Electron distributions in YZ plane ionized by laser light with different ellipticities. The ellipticity of A: 0.68; B: 0.5; C: 0.36; D: 0.25.

We measured the 3D electron distributions at different ellipticities and displayed the distribution in the polarization plane in Figure 24. The distribution is close to isotropic at higher ellipticity (Figure 24 (a)), but the slightly stronger intensities in second and fourth quadrants of the inner layer of the image were still visible. As the ellipticity decreased, the

intensities in the second and fourth quadrants became stronger and stronger while the intensity in the other two quadrants kept decreasing. Images became anisotropic but with a symmetry with respect to the origin. From the image, it is hard to recognize the forward and backward asymmetry in the laser polarization plane because the left side and right side of the image have symmetry over the origin.
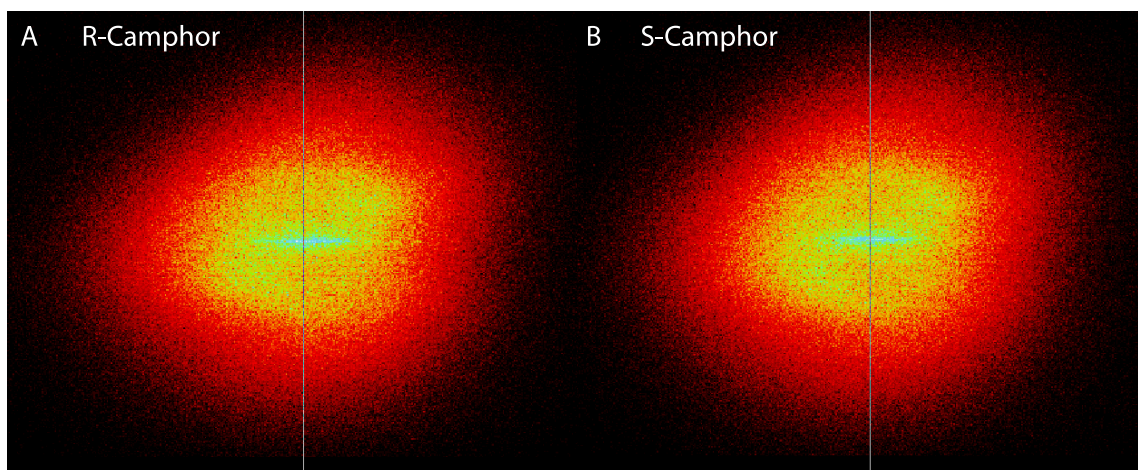
Figure 25: Electron distributions of S-camphor and R-camphor at ellipticity of 0.37. White lines indicate the TOF of zero-momentum electrons.

We measured anisotropic electron distributions for two camphor enantiomers at ellipticity 0.37. The deduction of Yt distributions (polarization plane) of R and S camphor did not show obvious asymmetric signature. Then we checked the asymmetry along TOF axis because this is the major axis of polarization ellipse. The previous study calculated the circular dichroism parameter of electron angular distribution using the formula $A_{CDAD} = I(\theta) - I(\theta+180°)/ I(\theta) + I(\theta+180°)$, which represents the ratio of the difference of forward and backward electron intensity over the total intensity. [50] In their experiment, "forward and backward" referred to directions along laser propagation. The acceptance angles of the hemispherical analyzers were ±5°. Here, the photoelectrons were collected by VMI

electrodes, allowing 4π solid angle acceptance. We used the above formula to calculate asymmetry parameter but in the polarization plane. Differently, the left side electrons are the ones with initial velocity toward the detector in YZ plane, arriving the detector earlier than zero momentum electrons (indicated by white lines in Figure 25), and the right-side electrons arrived later. We obtained the asymmetry parameter by using the difference of the left-side and right-side electron counts over the total counts. The calculated asymmetry parameters are -2.28% for R-Camphor over 359725 total single-hit events, and 1.93% for S-Camphor over 365968 single-hit events. This difference is very little, and a variance of 0.05 bin of TOF could lead the asymmetry parameter to close to zero.

When the strong field studies of camphor were carried out, the electron-ion coincidence measurements through pulsing electrodes had not been implemented; background electron signal (such as water, even though the intensity is very weak relative to camphor) could not be removed effectively according to coincidence with ions. To minimize background electron signal, the laser intensity was not high enough to generate ATI peaks, which have been observed in previous studies with employing femtosecond laser pulse at 398 nm [53].

Unlike the asymmetry along the laser propagation direction that is observable for unoriented molecules showed in previous studies, the asymmetric feature arising from the interaction between ionized electrons and chiral Coulomb potential could be diminished after accumulating enough electrons from unoriented molecules. If plotting the photoelectrons in the molecular frame, it is possible to observe asymmetric distribution. Our group has showed recoil-frame electron distribution by coincidence detection of electron and I^+ arising from single ionization and dissociation of CH_3I. [57] If there is a

way to reconstruct chiral molecular frames, such as using three ion fragments or more from Coulomb explosion, it would be possible to check whether the 3D electron distribution in this molecular frame is chiral or not.

3.1.4 Conclusion

We studied the strong field ionization and dissociation dynamics of camphor. Camphor molecules were highly fragmented through many single and double ionization and dissociation pathways (more than ten) at laser intensity $\sim 1 \times 10^{13}$ W/cm^2. The difference of asymmetries for forward and backward photoelectrons along propagation direction and in polarization plane arising from ionization of camphor enantiomers with elliptical laser beams were not obvious enough to extract any clear conclusion. In future studies, increasing the TOF of electrons might help distinguish asymmetric electron distributions along TOF axis in the polarization plane better. Besides, implementing electron-ion coincidence measurement could help remove background electrons. More importantly and innovatively, reconstructing chiral molecular frame and plot 3D electron momentum in this frame may visualized the asymmetric signature in polarization plane, but possible there will be difficulty to implement 3 ion - 3 electron coincidence.

3.2 A New Electron-Ion Coincidence 3D Momentum-Imaging Method and Its Application in Probing Strong Field Dynamics of 2-Phenylethyl-*N*, *N*-Dimethylamine

3.2.1 Introduction

The detection of coincidence photoelectrons and photo-ions generated from a single molecule/atom is a very effective method to explore the ionization and dissociation dynamics taking place through multiple reaction channels. The initially developed ions/electrons coincidence detection instrument only measured the kinetic energies of

charged particles by exploiting time-of-flight (TOF) spectrometer. [58-61] The arising of various position- and temporal-sensitive detectors, such as a delay-line detector, allow the measurement of positions as well as timing information of all particles and thus enabled 3-dimensional (3D) momentum detection. [41, 43, 62-65] Successful coincidence detection requires the count rate of the experiment to be less than one event per driving pulse (electron/ion/photon) to suppress false coincidence events. Traditional velocity mapping imaging (VMI) technique does not provide TOF information with a high resolution of every single particle. It only measures the TOF of zero-momentum ions in the range from nanosecond to one microsecond, which provides the mass of the detected ion cloud. On the other hand, VMI is capable of measuring momentum and angular distributions simultaneously and relatively easy to be adopted, so it is still widely used in many research fields, like atomic/molecular dynamics, ultrafast spectroscopy. Recently, a new type of 3D momentum imaging system has been developed through using a conventional MCP detector in combination with VMI apparatus. [45-46] The standard video camera used in conventional VMI was replaced with a CMOS camera and the electric pulses generated by MCPs are picked up by a high-speed digitizer through a signal decoupling circuit. The method to obtain 3 coordinates (x, y, t) and the capabilities to execute multi-hit detection and slicing electron Newton spheres with high time resolution have been introduced in Chapter 2. With this 3D momentum imaging system, sliced velocity mapping of photoelectrons alone TOF axis was achieved for the first time with an imaging detector. The demonstrated time resolution for this system is excellent (~30 ps). It was also demonstrated that 3D photo-ion-photoelectron coincidence measurement could be achieved by accelerating both ions and electrons in the electric field generated with double-

side VMI electrodes towards two imaging detectors placed at the opposite ends of the apparatus. [66-67] Is it possible to achieve photo-ion-photoelectron coincidence detection with one side VMI spectrometer and one imaging detector? Two problems that need to be solved are that both ions and electrons can be accelerated to the same detector in time and that the image pixels and digitizer pulses of electrons and ions can be separated completely. Here, we achieved 3D photo-ion-photoelectron coincidence measurement with a one-side featured VMI spectrometer and one single imaging detector by solving those two problems and without the need to significantly modifying the apparatus.

PENNA has two functional groups where a positive charge can reside: the chromophore group (phenyl) and amine group; these two groups are connected by a -CH_2-CH_2- saturated ethylene bridge. PENNA has attracted a lot of attention and enthusiasm to study its photoionization dynamics because a new type of charge transfers process that happens within an ultrafast time scale (from hundreds of attosecond to several femtoseconds) has been found in PENNA.[68-73] PENNA cation has two low-lying excited states that have energies 0.6 and 1.0 eV above the cation ground state, respectively. The ground state cation has a hole (positive charge) on amine side while the two excited states have holes on phenyl side. For a typical ultrafast pulse from Ti:sapphire laser that has photon energy of about 1.6 eV, these three cation states can be easily accessed simultaneously, so it can form a coherent superposition of these three states and thus the electronic density beats between the functional groups of PENNA.[74] Great efforts have been made on studying the photoionization dynamics and charge transfer mechanism of PENNA. Resonant two-photon ionization (R2PI) and Rydberg fingerprint spectroscopy have been employed to explore the slower intramolecular charge migration that happens

around 80 fs at different laser wavelengths. [68, 71, 75-76] However, such studies were limited to tens of femtosecond time resolution. A strong field IR-pump-IR-probe method has been proposed to observe the ultrafast charge migration with a resolution of few femtoseconds.[73] So far experimental investigations on the photoionization dynamics of PENNA under intense laser field have been scarce. Furthermore, the dynamics of dissociation following ionization (single and double) are crucial for measuring molecular/recoil frame ionization rates because they show whether the axial recoil approximation is valid or not. With the axial recoil approximation, the recoil-frame ionization rate measurement is much simpler than those methods that require pre-alignment of molecules.

Here, we apply a new 3D electron-ion coincidence technique that accelerates both ions and electrons toward one detector by pulsing the electrodes to study the photoionization and the following dissociation process of PENNA. This result will provide background information for future time-resolved studies.
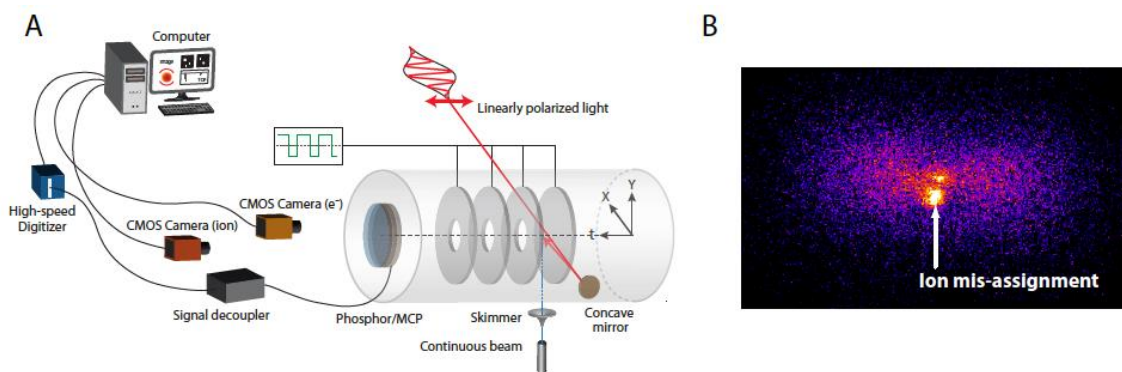
Figure 26: (A) The schematic of the two-camera based 3D momentum-imaging detection system that can conduct ion-electron coincidence measurement by a single detector. (B) The image obtained from utilizing one camera to capture both ion and electron flashes on the detector. This image has mixed electron and ion features arising from strong field ionization of PENNA with circularly polarized light.

3.2.2 Experimental setup

PENNA molecules are ionized with an amplified 800 nm Ti:Sapphire femtosecond laser in mid-intensity strong field ($\sim 8 \times 10^{13}$ W/cm^2). The pulse duration of this ultrafast laser pulse was ~30 fs and the laser run at 1.5 KHz. The laser beam was linearly polarized, and the polarization was along the time-of-flight axis. For the one-camera setting, the experiment was carried out with a circularly polarized laser. PENNA (purity 98%) was purchased from Sigma-Aldrich. Helium was used as seed gas to send PENNA into the source chamber by a gas jet with a 20μm orifice. The PENNA sample and the gas jet were heated to ~30°C and ~70°C from outside of the source chamber, respectively, to get PENNA vaporized and make sure it will not become condensed phase again when sending it through the gas jet. A skimmer with 0.5 mm orifice then skimmed the ejected molecular beam from the gas jet, so only the center part of the beam entered the main chamber. The laser beam was sent through the front window of the main chamber, perpendicularly with the molecular beam and the TOF axis, and it was focused onto the molecular beam tightly by a concave mirror ($f = 5$ cm) inside the main chamber. A four-plate electron-ion optics was built to velocity map the electrons and ions arising from strong-field ionization. A short TOF length (~10 cm) was adopted to allow detection of high-energy electrons. The timings of electrons and ions hitting the detector were picked off from the front MCP plate by a high-speed digitizer through a signal-decoupling circuit. The positions of electrons and ions hitting the detector were recorded from the phosphor by two CMOS cameras separately. The two cameras are set ~65 cm and ~120 cm away from the detector. The electron camera points at the center of the phosphor screen with a normal angle, while the ion camera slightly deviates from the detector normal (~6°). The justification for the use

of two cameras is discussed in the Results and Discussion section. A schematic of the experimental setup is shown in Figure 26 (A).

3.2.3 Computational methods

Density functional calculations were executed with the development version of Gaussian using the ωB97xD functional.[77] 6-31G(d) basis set was used to carry out the initial electronic structure optimization, relaxed potential energy surface scans, and transition state location. The obtained electronic structures including the ground state of neutral PENNA, cation, dication, transition states, and dissociated products were further optimized with larger basis set 6-311++G (d,p) to improve the accuracy. SCF energies of all structures were calculated with this larger basis set and all wave functions were tested for SCF stability. Open-shell singlet and triplet structures of PENNA dication were identified with spin-squared expectation values ($<S^2>$) and spin density populations. GaussView[78] was used to visualize isodensity plots of the spin populations (isovalue = 0.004 au). Relaxed potential energy scans were carried out by stretching the C-C bond coordinates and optimize other coordinates, to explore the dissociation reaction pathways of PENNA dication. Normal mode vibrational analysis was applied to all optimized geometries. For the transition states on open-shell singlet and triplet dissociation energy surfaces, it is confirmed that they only have one imaginary vibrational mode. The closed-shell singlet dication is an excited state. Its geometry was obtained by vertically exciting the ground state of neutral PENNA. The relaxed potential energy scan of closed-shell singlet state was carried out following and the dissociation was tracked by Damped Velocity Verlet (DVV) reaction path. The closed-shell singlet structure had a closed-shell to open-shell instability and the wave function optimized to open-shell singlet after C-C

bond length increased longer than that of the transition state of the open-shell singlet.

The photoelectron spectrum was calculated by modeling the excitation and ionization dynamics of PENNA molecules at frozen geometry with a 22 fs 800 nm IR pulse with a field strength of 10^{12} W/cm^2. The time-dependent Schrödinger equation was numerically integrated using a basis of neutral and cationic electronic states.[74] The lowest 30 neutral states and 10 cationic states were calculated with time-dependent density functional theory (TDDFT) using ωB97xD functional and 6-311++G(d,p) basis set. A dense manifold of excited states is needed to accurately describe the multiphoton excitation and ionization of ground neutral PENNA molecules. The ionized states are described as the anti-symmetrized product of the field-free cationic electronic states and the wavefunction of the ionized electron that is described with a plane wave. This approximation, however, could affect the yield of electrons with low kinetic energy because the interaction between ionized electron and the ion core is neglected, and electrons generated from over-the-barrier and tunnel ionization are not included. The simulated ionization conditions are varied from different energies (0-25 eV) and angular distributions. In total, 18000 ionized states and 30 neutral states are included in the basis totally. The ionization dynamics for a set of 50 randomly oriented molecules were computed to simulate the random orientation of PENNA molecules in a real experiment. The photoelectron spectrum was computed averaged over different orientations according to the amplitudes of the ionized states.

3.2.4 Single ionization dynamics with ion mode
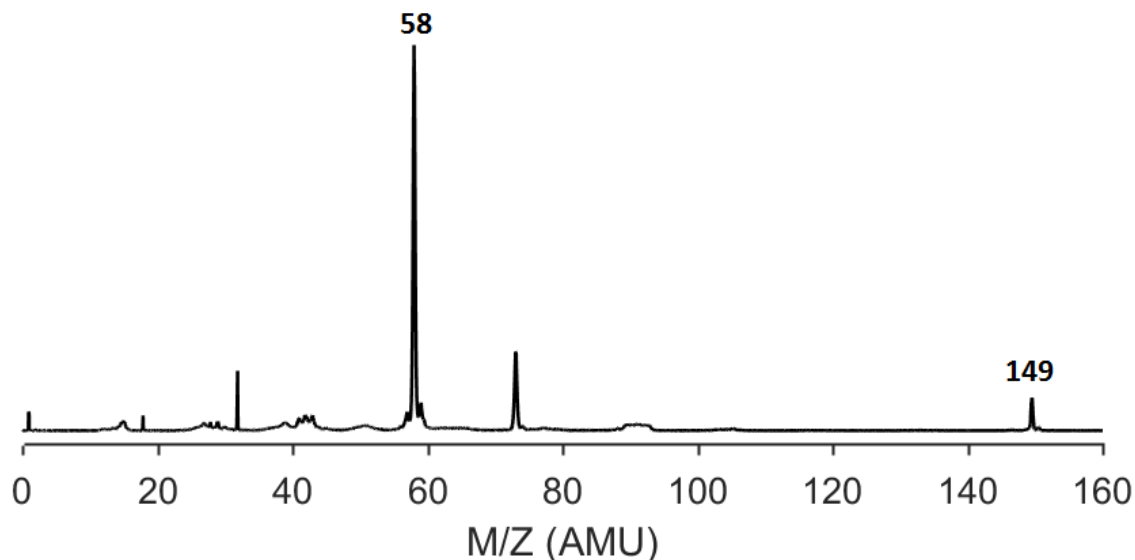
Figure 27: Mass spectrum of PENNA in mid-intensity strong field ionization.

Mass spectrum of PENNA in an intense laser field shows that the major product is dimethyl amine monocation ($N(CH_3)_2CH_2^+$, mass 58). The intensity of parent ion is much lower than that of mass 58 (~0.05), which suggests most parent ions are not stable and dissociated after strong field ionization. Even though the peak of mass 91 is small, it is still observable. The wide spread of this peak suggests the kinetic release of this fragment and it may arise from double ionization, which will be further confirmed by the 2D coincidence intensity map.
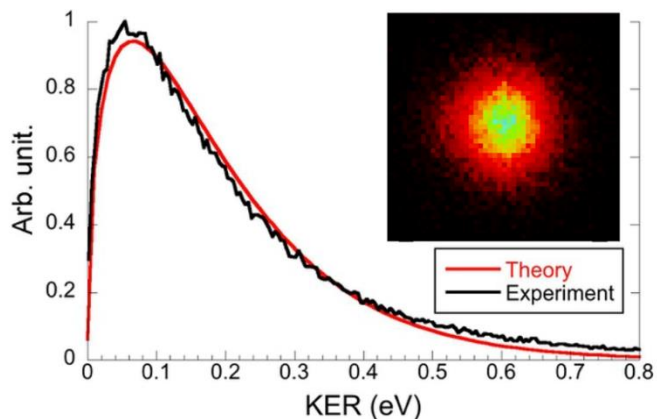
Figure 28: Kinetic energy release of $N(CH_3)_2CH_2^+$ fragment. The black color is the experiment data and the red color is the theoretical simulation. The inset is the velocity distribution in XY plane.
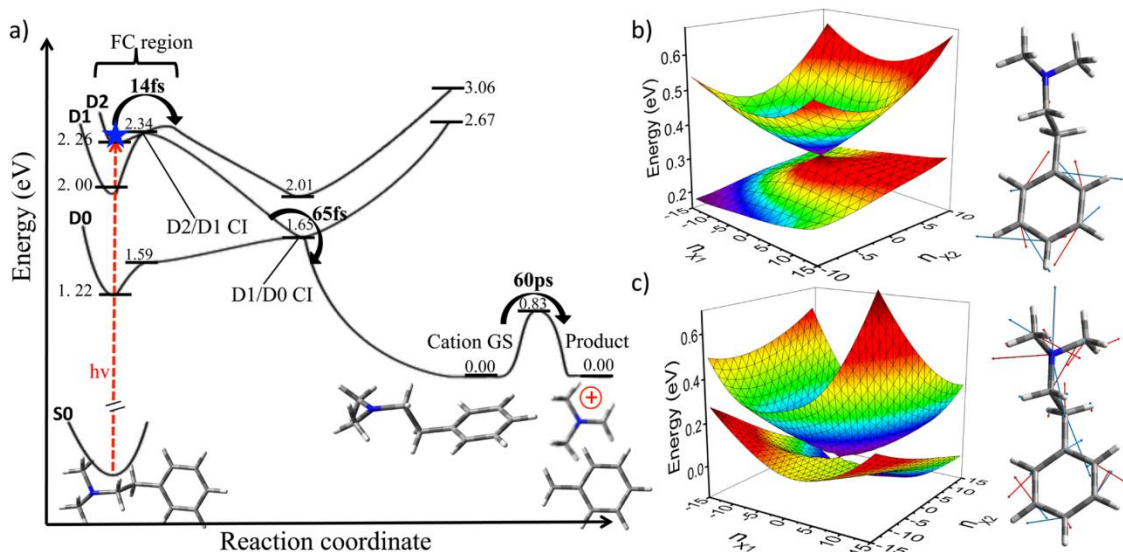
Figure 29: Dissociation pathways of single ionization of PENNA. (a) Potential energy surfaces. (b) and (c). Conical intersections of D1/D0 and D2/D1 pathways. (Adapted from ref. [79])

Sun et. al. explored the single ionization and dissociation dynamics of PENNA. [79] The neutral ground state PENNA molecule is ionized to three lowest cation states: ground state cation D0, and two lowest excited states D1 and D2 that have energy 0.8 eV and 1.0 eV above the ground state cation. The photon energy is 1.5 eV, which can excite the three lowest cation states simultaneously. There are two conical intersections between

D2 and D1 energy surfaces and D1 and D0 energy surfaces along stretching the C-C bond length. The excited D2 state transfers from the D2 surface to D1 surface through the D2/D1 intersection. The time it takes is about 14 fs. As C-C bond stretches further, D1 state transfers to D0 state in ~ 65 fs. The positive charge of D0 state is on amine side while the positive charge of D1 and D2 states are on phenyl side, the transfers between three lowest cation states caused the charge migration between phenyl and amide side of PENNA. The ground cation state D0 proceeds through an energy barrier of 0.8 eV and dissociates into two fragments: positive amine group $N(CH_3)_2CH_2^+$ and neutral phenyl group C_6H_5-CH_2. The time scale to proceed through the energy barrier is ~ 60 ps.

3.2.5 Achieving 3D coincidence measurement with a single imaging detector

To update a conventional VMI to a coincidence 3D momentum imaging apparatus, we need to address two issues associated with it. The first issue is the uni-directional spectrometer of a conventional VMI apparatus. It can normally be operated in either photoelectron or photo-ion mode by applying different voltages on the electrodes. To image both ions and electrons with the same detector, the voltages of electrodes should be switched very quickly to accelerate both kinds of particles toward the same direction. This has been demonstrated by Janssen and coworkers to pulse the electrodes and employing a delay line detector.[80] Owing to the large mass difference between electrons and ions, the electron can maintain the same imaging condition as with non-pulsing electrodes while ions suffer minimum momentum blurring (SIMION simulation ~1%). Once ions and electrons arrive at the imaging detector, they both produce flashes on the phosphor screen, which are then captured by the camera in the same frame. However, how to associate the positions and measured TOFs is not trivial. It has been shown in the previous study that

the brightness of camera spots has a strong linear correlation with the amplitude of digitized waveforms in either ion or electron mode.[45] This correlation is exploited to associate the positions and TOFs in a multi-hit event. The correlation slopes, however, are different for electrons and ions. When using one camera to capture both ions and electrons in pulsing mode, linear correlation scheme cannot separate ions and electrons completely when associating camera and digitizer signals arising from both electrons and ions (Figure 26 (B)).

The timing information of electrons and ions from digitizer can be separated completely because electrons arrive on the detector much earlier than ions. If we add another camera to separate ion and electron spots, the problem of the incomplete separation between electron and ion images can be solved. All ions and electrons are accelerated to the same detector. The way to separate them is according to the large TOF difference between them. Electrons have much smaller mass than ions, and the TOF is much shorter (<100 ns) than ions (> 1 us), so electron camera can be triggered to only expose for the first 200 ns after the laser pulse while the ion camera starts to expose with 500 ns delay to only image ions. This two-camera configuration (Figure 3.5(A)) makes the association between the time and position of the charged particles become quite easy and self-evident: the position information in the electron camera is associated with the electron TOFs while those positions in the ion camera with the timing information of ion. Since the electrons and ions are completely separated by the two-camera scheme, the linear correlation between pixel intensity and waveform amplitude can be applied to the electrons and ions independently. The difference between the electron and ion slope will not affect the result. With this new scheme, we can achieve ion-electron coincidence 3D imaging measurement

for the first time with a single MCP/phosphor detector. We estimated the spatial and temporal resolutions to be 6% and 1% for ions and 3% and 3% for electrons, respectively. We showed the results of ion-electron double coincidence arising from PENNA single ionization and electron-ion-ion triple coincidence resulted from PENNA dissociative double ionization in Figures 30 and 32.

3.2.6 Single ionization of PENNA
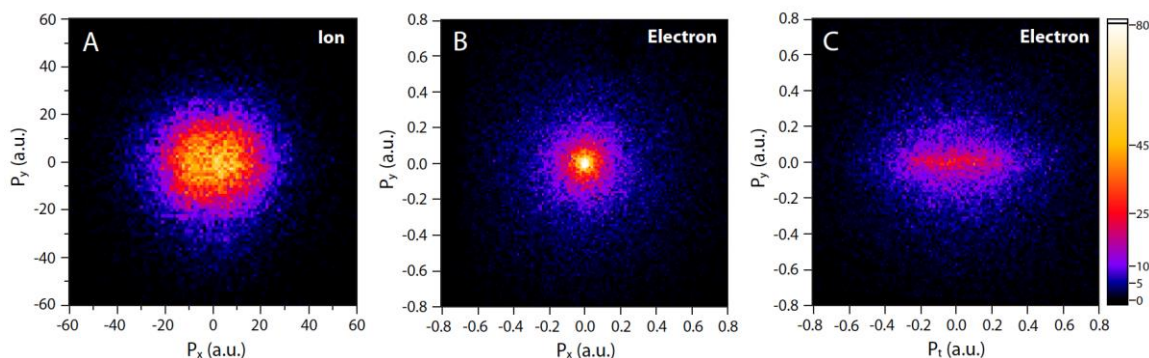
Figure 30: (A) XY momentum distribution (parallel to the detector) of dimethyl amine monocation ($N(CH_3)_2CH_2^+$). (B) XY and (C) Yt momentum distributions of photoelectrons in coincidence with $N(CH_3)_2CH_2^+$.

Figure 30 (a) shows the momentum distribution of $N(CH_3)_2CH^{2+}$ in the plane perpendicular to the laser polarization while Figures 30 (b) and 30 (c) show the momentum distributions of electrons in coincidence with $N(CH_3)_2CH^{2+}$ in XY and Yt planes (perpendicular and parallel to the laser polarization), respectively. The isotropic momentum distribution of $N(CH_3)_2CH_2^+$ in XY plane (Figure 3.2 (A)) indicated that the dissociation time scale is longer than the rotation period. The electron energy distribution and its comparison with theoretical calculations resulting from frozen geometry simulations of the electron dynamics of randomly oriented molecules are shown in Figure 31 (A). The agreement is good for high kinetic energy electrons (above 4 eV), but it shows a discrepancy at low kinetic electron energy. This discrepancy arises from the limitations

of the model used in the simulations. The model only includes the multiphoton photoionization process and ionization by the laser pulse, while it neglects low energy electrons generated from over-the-barrier or tunneling ionization. This result further suggests that in strong field ionization, the photoelectron spectrum alone is insufficient to identify the produced cation electronic states. A complete theoretical modeling of the strong field photoionization of big molecules such as PENNA is currently out of reach.

With the electron-ion coincidence measurement capability, we can produce the correlation map between the KER of the dissociated fragments and the electron kinetic energy (eKE) and this is shown in Figure 31 (b). Interestingly, an apparent correlation can be seen (the diagonal structure). However, because the energy scale is different between the KER and eKE, it is unlikely that an energy conservation mechanism (as in single photon ionization) is at play. Upon further investigation, such a structure persists even for non-dissociative channels such as water single ionization, which suggests that the observed feature is not true correlation. However, we did observe a significant difference in momentum distributions of electrons in coincidence with monocations and dissociative dications (see Figures 30 (c) and 32 (c)). This validates our method for detecting coincidence events.
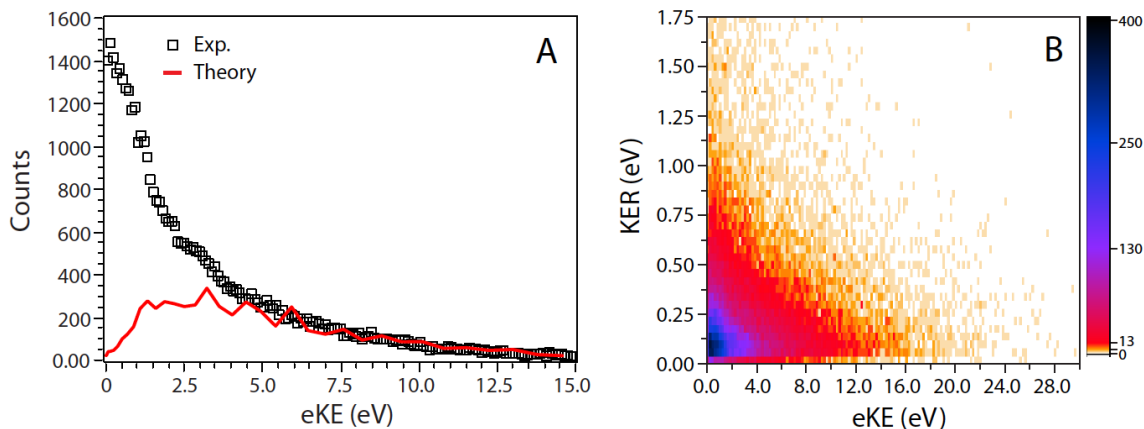
Figure 31: (A) The kinetic energy release of photoelectron from single ionization (black) and comparison with theoretical calculations (red). (B) The 2D energy correlation plot between ion KER and electron kinetic energy.

3.2.7 Double ionization and dissociation dynamics of PENNA
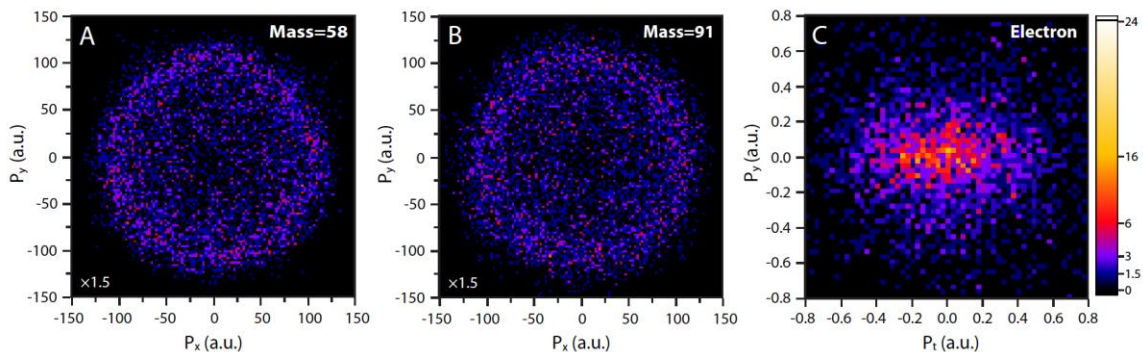
Figure 32: XY momentum distributions of coincidence ion pairs of (A) $N(CH_3)_2CH_2^+$ (mass 58) and (B) $C_6H_5-CH_2^+$ (mass 91). (C) Yt momentum distributions of photoelectrons in coincidence with the ion pairs.

PENNA dication did not appear in the mass spectrum. There are two possibilities: there is no double ionization or all dications dissociated. After checking the 2D TOF (Figure 33 (A)), we find that two fragments: dimethyl amine monocation ($N(CH_3)_2CH_2^+$, mass 58) and benzyl monocation ($C_6H_5-CH_2^+$, mass 91) showed a strong correlation (diagonal structure). The total mass of these two fragments equals the molecular mass PENNA. These demonstrated the appearance of dissociative double ionization of PENNA. Even though the 3D detection system is capable of detecting double-hit events of electrons,[47] triple coincidence (ion-ion-electron) was used to study the momentum, angular and energy distribution of the dissociated fragments because two-electron measurements do not provide further insight to this study while requiring much longer time to collect and analyze data. The momentum distributions of two fragments originating from double ionization of PENNA were shown in Figure 32.
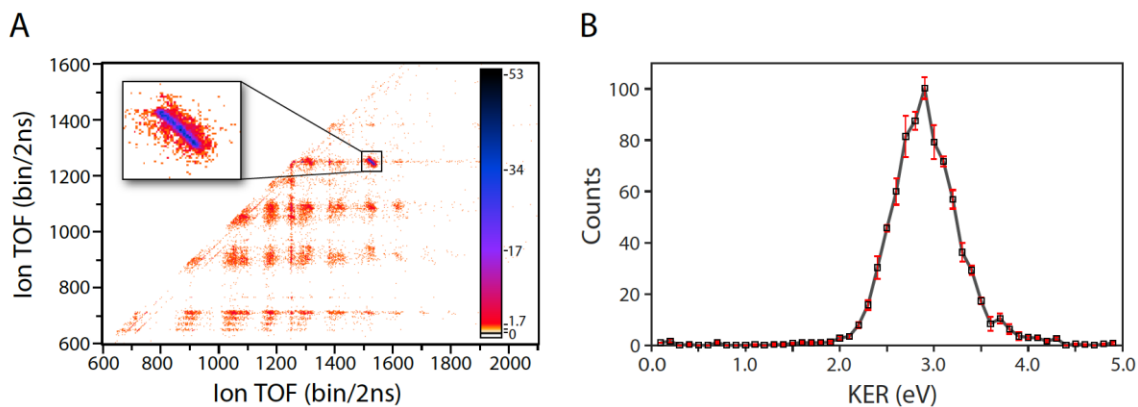
Figure 33: (A) 2D TOF of dissociative double ionization of PENNA. (B) The KE distribution of ion pairs from double ionization.

It can be readily identified from the photoion-photoion coincidence (PIPICO) map (Figure 33 (a)) that the major dissociation channel leads to the dimethylamine monocation ($N(CH_3)_2CH^{2+}$, mass 58) and benzyl monocation ($C_6H_5CH_2^+$, mass 91). Momentum conservation criteria can help remove false coincidence events. After applying momentum conservation criteria, we can cleanly select the ion pairs that arise from the dissociation of the PENNA dication. Figure 32 (A) and (B) show momentum distributions of ion pairs from double ionization after applying momentum conservation criteria in the XY plane. Figure 32 (C) is the Yt image of coincidence electrons. The angular distributions of both fragment ions are isotropic (spherical), suggesting that the dissociation time scale is longer than rotation period. The total KER of the ion pairs is around 2.9 eV and has a cutoff around 4 eV (Figure 33 (B)). The data points in the KER curve are the average values of four data sets.
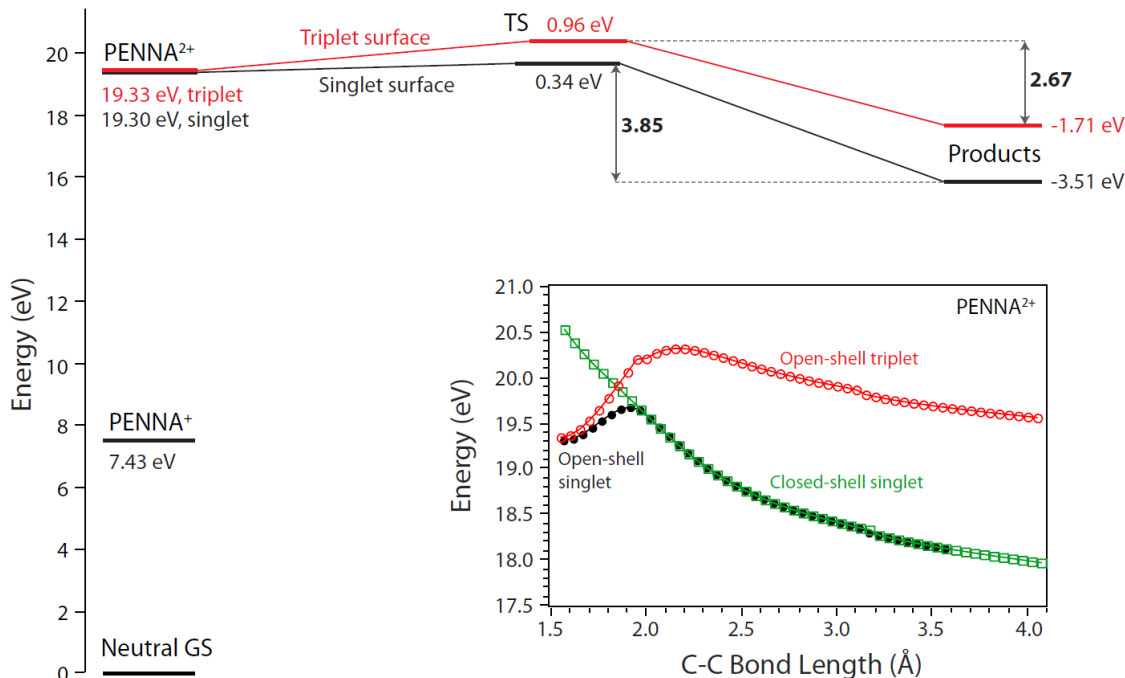
Figure 34: Relaxed potential energy surfaces along C-C bond.

Now we turn to the theory to help identify the dication states that are involved in the dissociation processes. There are three possible electronic structures of PENNA dication: closed-shell singlet (with two electrons removed from the same orbital), open-shell singlet (with two electrons removed from two different orbitals and the rest two single electrons have different spins), and open-shell triplet (with two electrons removed from two different orbitals and the rest two single electrons have the same spin). Density functional calculations were carried out to identify the dication state(s) generated in strong field double ionization. In previous studies, the ground state of neutral PENNA has been determined.[68, 74] We started with the geometry of neutral PENNA and adiabatically optimized the structures of PENNA cation and dication. The energy of PENNA cation is 7.43 eV higher than the neutral ground state. The energies of open-shell singlet and triplet dications are very close: 13.30 eV and 13.33 eV above the neutral ground state. The following relaxed scans by stretching the C-C bonds indicate that the potential energy

surfaces of closed-shell and open-shell singlet states overlap after the energy barrier of open-shell singlet and lead to the same products. The difference is that the open-shell singlet structure has an energy barrier and the closed-shell singlet is energy barrierless when stretching the C-C bond (Figure 3.6 inset). The potential energy surface of the open-shell triplet has higher energy when the C-C bond length is the same. It is also shown that the transition state of open-shell triplet has a longer C-C bond length (2.17 Å) than open-shell singlet (1.92 Å). The activation energy of the open-shell singlet is 0.65 eV lower than open-shell triplet, meaning this energy barrier is easier to be accessed. From transition state to products, open-shell singlet release 3.85 eV energy while open-shell triplet release 2.67 eV. Comparing with the KER of the ion pairs from double ionization, the reverse energy barrier of open-shell singlet is close to the cutoff energy (maximum energy) of KER of the ion pairs. These two facts suggest that the dissociation of metastable PENNA dication is dominantly through the open-shell singlet dissociation pathway and the electronic structure of open-shell singlet radicals are the main products in the strong field double ionization. Closed-shell singlet state could not survive in the structure optimization process, which means this electronic structure is unstable and is an excited state. The barrierless potential energy surface would lead to anisotropic distribution, which did not show up in strong field double ionization. Besides, the excitation of the closed-shell singlet is very high, so this electronic structure is not accessible.

3.2.8 Achieving 3D momentum-imaging of electrons at 10 kHz and beyond

Finally, another major improvement of the camera-based momentum-imaging system was demonstrated. For a typical coincidence measurement, because of the low count rate required for achieving true coincidence, it is preferred to have the whole system

running at a repetition rate as high as possible. The limiting factor is usually the laser system. While one kHz laser is very popular and suitable for the camera-based 3D momentum-imaging setup, higher repetition lasers running at 10 kHz or 100 kHz do exist and are being used in many strong field experiments. By exploiting a simple fact of all coincidence measurement, we can improve the repetition rate of the current imaging system by five to ten folds without upgrading the camera. The low count rate of a coincidence experiment means that not every camera frame has event-hits. For example, roughly 80% of the camera frames will be without event-hit if the camera frame rate is the same as the laser repetition rate and the count rate is kept below 0.2 events/laser shot. This suggests that the camera frame rate is not fully utilized in this way. A different way of running experiments is to expose a camera frame for more than one laser shots. As long as the average hit in the camera is close to one per camera frame, the camera event and digitizer event can be correlated to provide the three coordinates for 3D momentum imaging. Even if there are a few events in one camera frame, the brightness-intensity correlation will be able to correlate the times with the positions of the events. With this method, the camera frame rate can now be fully utilized while the system repetition rate is increased five to ten times beyond the highest camera frame rate. This was demonstrated using a 10 kHz laser located in the Kapteyn/Murnane group at University of Colorado of Boulder. The camera was running at 2 kFrames/second and the laser at 10 kHz. A standard VMI system with a three-lens spectrometer was used to detect the photoelectrons arising from strong field ionization of Krypton. Because only electrons were of interest, no electrode-pulsing was employed. Figure 35 shows the 3D momentum distributions of the electron Newton cloud.

The achieved spatial and temporal resolution was good while it took only five minutes to accumulate these events.
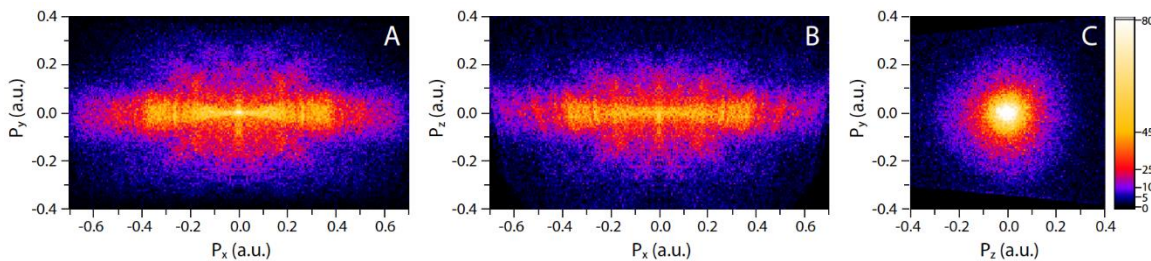
Figure 35: 3D momentum distributions of photoelectrons arising from strong field ionization of krypton. The laser beam was linearly polarized and run at a 10 kHz repetition rate. The camera-based imaging system runs at 2 kFrames/second.

3.2.9 Conclusion

We demonstrate a new method to convert a standard VMI apparatus to a coincidence 3D momentum-imaging setup without modifying parts inside the vacuum chamber or the imaging detector. It should be noted this setup is automatically capable of slicing the electron Newton sphere due to its excellent temporal resolution. The additional cost for adding a second camera is minimum. The current setup requires a high repetition laser in order to expedite the data acquisition. Further improvement of the multi-hit capability might enable this to be used with lower repetition lasers. Furthermore, we have shown that a high system repetition rate beyond the camera frame rate can be achieved.

With this new imaging setup, by measuring the KER of dissociative double ionization and comparing it with density functional calculations, we show the main products of strong field double ionization of PENNA are singlet diradicals, which dissociate into $N(CH_3)_2CH_2^+$ and $C_6H_5-CH_2^+$. The isotropic distributions of fragment ions suggest a long lifetime of the parent dications, which poses a challenge for future experiments that aim for molecular/recoil frame ionization rate.

CHAPTER 4. TIME-OF-FLIGHT BASED ANGULAR-RESOLVED PHOTOEMISSION SPECTROSCOPY

4.1 Introduction

Angular-resolved photoemission spectroscopy (ARPES) is a powerful tool to study surface or bulk structure of solids, like metals or semiconductors. The emitted photoelectrons are detected by an energy analyzer and a detector at the exit. Hemispherical energy analyzers are widely used to select electrons with kinetic energy in a certain range; acceptance angles are normally around $15° - 30°$. Great efforts have been made to detect photoelectrons from different angles simultaneously. A TOF analyzer can detect electron energies and accept emitted electrons from different angles in a larger range, compared to a hemispherical analyzer. The acceptance angles, however, still has a limited range. Rotating TOF analyzers and detectors to different directions relative to the sample have been employed to capture electrons in full range.[81] These methods increase the complexity and cost to build an instrument significantly.

Takahashi et. al. exploited frequency doubled ($2hv$) and tripled ($3hv$) laser beams of 810 nm fundamental beam with 200 fs duration to measure the multiphoton photoemission (MPPE) spectra of graphite at normal emission geometry. [82] They observed peaks at 2.11 eV, 2.82 eV, and 2.94 eV (very weak) in the photoelectron energy spectrum when using $2hv$ to excite photoelectrons (Figure 36 (a)). The MPPE spectrum of $3hv$ beam shows a broad peak around 1.7 eV and a small peak at 3.65 eV. They described the binding energy of IPS states by the formula: $E_b(n) = 0.85/(n+a)^2$, where n is the quantum number and a is the quantum defect. The binding energies of IPSs could be deduced from the KE spectra shown in Figure 36. The measured binding energies lead to a quantum

defect of -0.07 ± 0.02. They found that the lifetime of electrons at IPSs decreases as the transverse momentum increases through intrinsic line-width analysis. The electrons at the bottom of the parabolic dispersion ($k_\parallel = 0$) have the longest lifetime ~16 fs. A similar study on IPS of graphite was carried out earlier in 1999 with different fundamental laser beams at different laser wavelengths and pulse durations. [83] Differently, they employed 2PPE to measure the lifetime of electrons at IPS, in which 3hv (267 nm) was exploited to excite electrons to IPS n=1 and 2hv (400 nm) was used to excite electrons at IPS. They obtained a lifetime of 40 ± 6 fs for IPS n=1 of graphite.
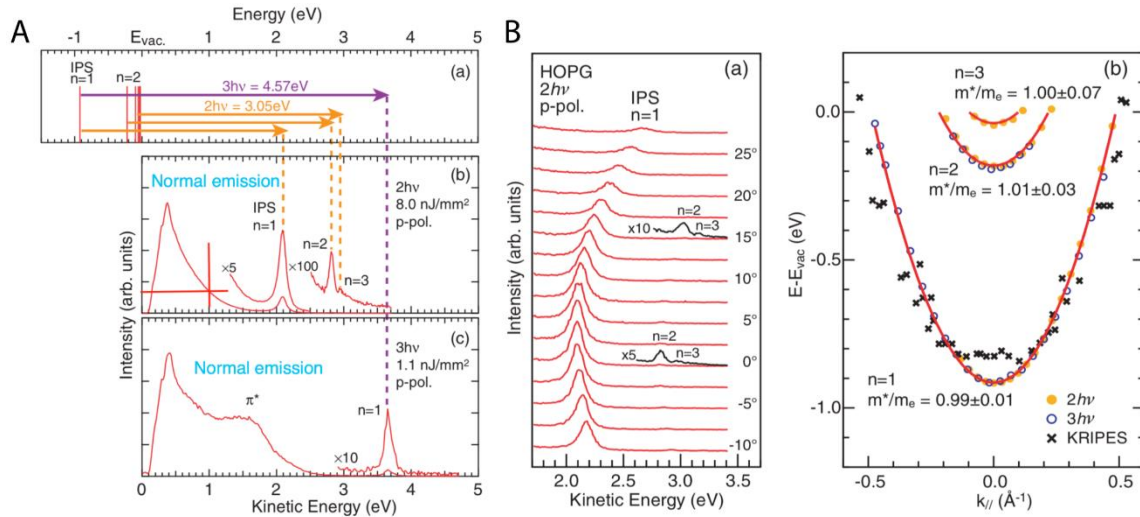
Figure 36: A. (a) Energy diagram of the electron excitation from the IPS by 2hv and 3hv pulses. (b) Normal emission spectrum excited with a 2hv pulse as well as (c) that with a 3hv pulse. B. (a) Angle-resolved spectra with 2hv excitation at polar emission angles from −10° to 27.5°. Five- and ten-times magnified spectra are also shown for emission angles of 0° and 15°, respectively. (b) Two-dimensional band dispersion of IPS with n = 1, 2, and 3 determined from the AR-MPPE spectra. (Adapted from [82])

4.2 Schematic of experiment

As described in Chapter 2, VMI technique accelerates charged particles along the electrodes' axis while the momenta parallel to electrodes are almost conserved. It allows

2π solid angle collection of emitted electrons (from -90° to 90° with respect to the surface normal). By combining the VMI spectrometer with the 3D momentum imaging detection system, we can measure the momentum, energy and angular distribution of photoelectrons simultaneously without the need to rotate the detector or the sample and to collect photoelectrons of different kinetic energies at once, unlike an energy analyzer that has a relatively narrow range of acceptance angle in ARPES.

The first electrode (electron side) of the VMI ion/electron optics has a threaded hole (Φ30 mm) in the center. A stainless plate with edge threaded was used to load thin film samples and then was installed onto the first electrode. These thin metal (~10 nm)/graphene films were deposited on fused silica plates (1 mm in thickness) through chemical vapor deposition (CVD) method. Figure 37 shows the schematic of transmission geometry we exploited for the surface experiments. A laser beam (red arrow) was sent perpendicular to a surface sample to excite photoelectrons (green hemisphere), which were then accelerated towards the detector.
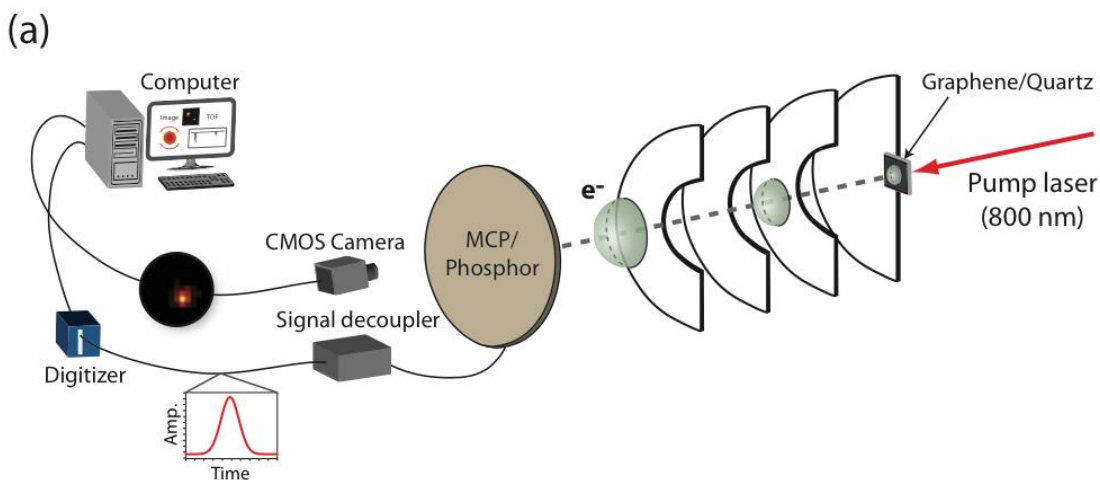
Figure 37: The schematic of surface experiment apparatus.

4.3 Photoemission from thin metal films

We explored photoemission from thin Al and Cu films, both of which have a thickness of about 10 nm. The fundamental laser beam was a mode-locked Ti:sapphire ultrashort pulse at 800 nm. Frequency doubled beam was generated with β-barium borate (BBO) crystal (type II). Two harmonic separators were used to filter out the fundamental light when using the 2nd HG as incident light. To obtain 3rd HG, the 2nd HG and fundamental beam need to reach the 3rd HG crystal simultaneously with the same polarization direction. Calcite was used after the BBO crystal that generates 2nd HG to compensate the time delay between the 2nd HG and the fundamental beam. Followingly, a zero-order half waveplate rotated the polarization of fundamental beam to be same with the 2nd HG. These two steps guaranteed the temporal and spatial overlap of fundamental and 2nd HG on the 3rd HG crystal. Four 3rd harmonic separators were used to remove the 2nd HG and fundamental residue mixed in the 3rd HG beam.

4.3.1 Multiphoton photoemission from metal surfaces

The emitted photoelectrons were detected with the 3D detection system introduced in Chapter 2. We employed a digitizer with a sampling rate of 2 GHz to measure the timing of electrons. The obtained electron distributions in Yt plane of Al film are shown in Figure 38. When Al film was irradiated by fundamental IR (red) and 2nd HG ($2 \nu_0$) beams, it generated two different kinds of electron distributions. Figure 38 (a) and (b) show the two types of distributions using red light. In Figure 38 (a), the stronger intensity at the front has a hemispherical-like distribution and it has "dress" outside that extends to longer time duration. We also observed an elliptical distribution at Yt plane using the red beam. Similarly, two different types of distributions were observed when employing frequency-

doubled UV beam, shown in Figure 38(c) and (d). For photoemission excited by 3rd HG, only one kind of distribution was observed. We then switched to a Cu film to examine whether it is unique to Al or general to different metal films. Similarly, we performed photoemission measurements on Cu film using red, frequency-doubled and frequency-tripled beams. We only observed one kind of distribution for each light, which was two ellipses with same intensity overlapped each other for Cu sample. The electron distributions generated from the Cu film are not shown here.

The different Yt images when exploiting the same laser beam could arise from the different laser intensities, different spots on the Al film that have different surface roughness and thickness, or detector was saturated, or the digitizer was unstable. To reach 2 GHz sampling rate, the two channels of the digitizer needed to be combined and synchronized. If the synchronization was not good, it could lead to poor temporal resolution or even incorrect YZ distribution after associating camera and digitizer signals.

4.3.1.1 Al sample
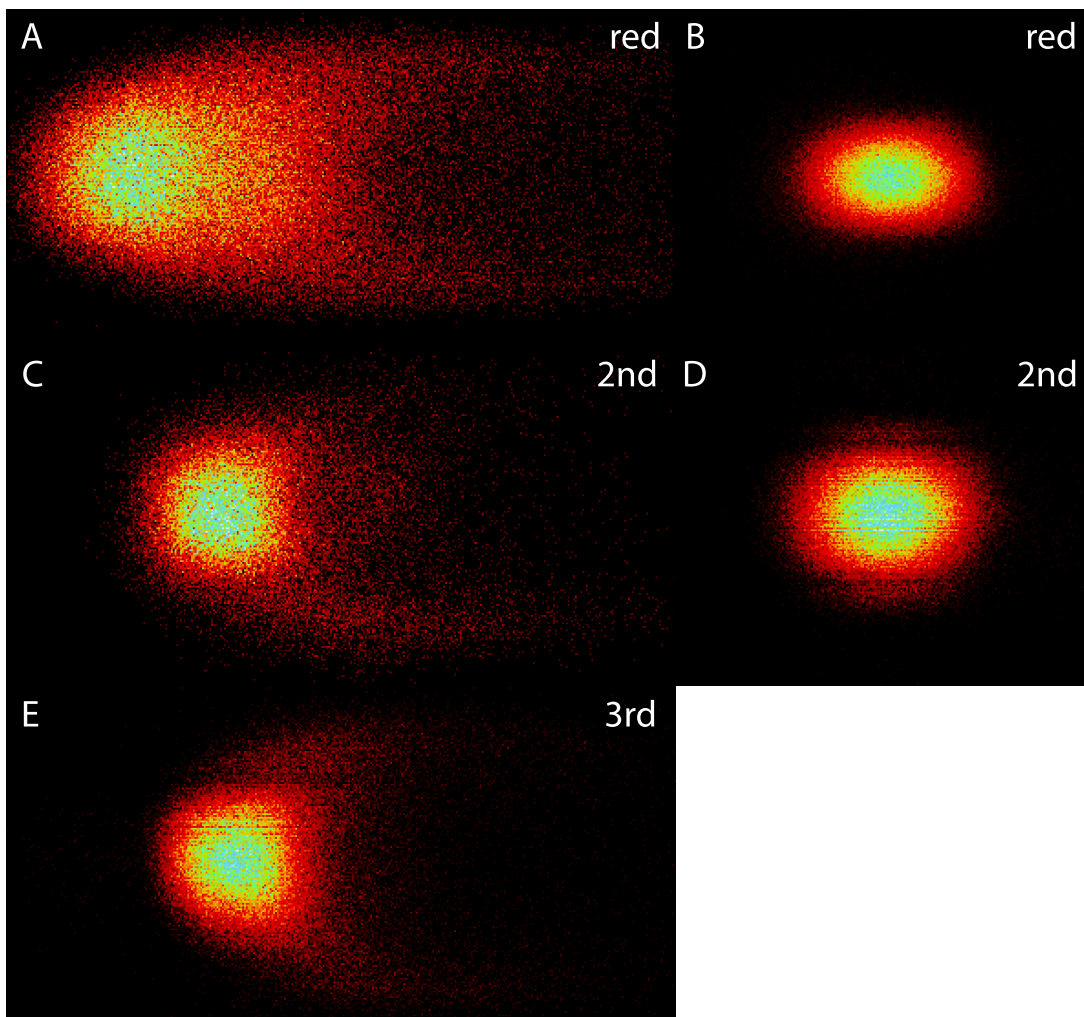
Figure 38: Yt image of Al sample excited with fundamental IR beam (800nm), 2nd HG and 3rd HG beams.

Electrons emitted from a surface can only have velocity components towards the detector and the zero momentum electrons give a clear cutoff, so the velocity distribution should be hemispherical like (Figure 37). Then we realized that the time resolution of the digitizer may not be high enough to detect electrons, which have very short TOF (several *ns*). The two channels of the digitizer needed to be combined to reach 2 GHz, so it is also possible that they were not synchronized well. We switched to a new digitizer that has a

sampling rate of 5 GHz, with which we immediately observed hemispherical-like electron

distribution from Cu film, shown in Figure 39.
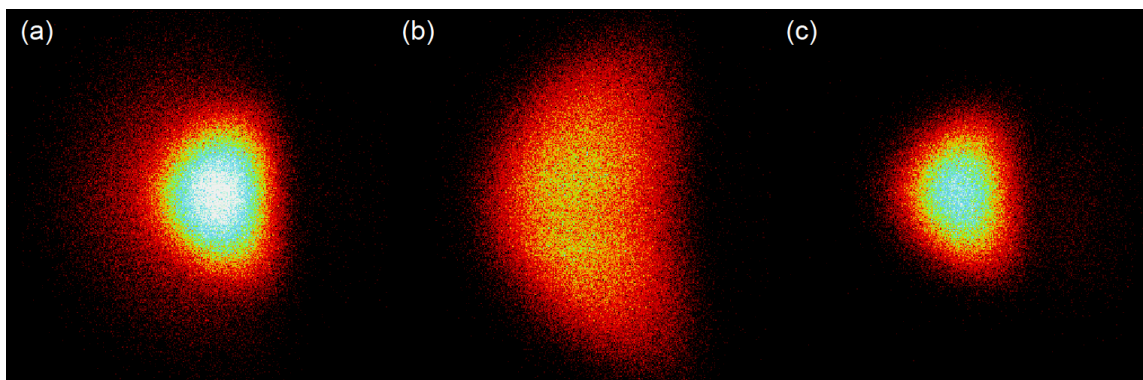
Figure 39:   Yt image of Cu sample excited with (a) fundamental (800 nm), (b) 2nd HG
and (c) 3rd HG beams. These images are shown in same scale.

Since these are all electrons, the velocity distributions are proportional to

momentum distributions. 2nd HG gave rise to larger momentum and KE release compared

with fundamental beam and 3rd HG. The work function of Cu is ~ 4.5 eV. The photon

energy of 2nd HG is ~3.2 eV, so it takes about two photons to emit one electron. The KE

release is around 1.9 eV. For the fundamental beam (~1.6 eV), it takes 3 photons to rip one

electron from the surface sample, the kinetic energy release would be ~0.3 eV. For 3rd HG,

the photon energy is 4.8 eV, so it takes one photon to ionize one electron and it should have

similar KE release with the fundamental beam. However, the image size of the electron

distribution arising from the fundamental beam (Figure 39(a)) is slightly larger than the

image size arising from 3rd HG. The fundamental beam might have higher order

multiphoton photoemission than 3-photon process. To demonstrate the multiphoton

process of photoemission from Al and Cu sample, we measured the yield of electrons as

increasing the laser power and plotted them in log scale (Figure 40). From these plots, the

linear fittings show that it is a three-photon process for the fundamental beam and two-photon process for the frequency-doubled UV beam.
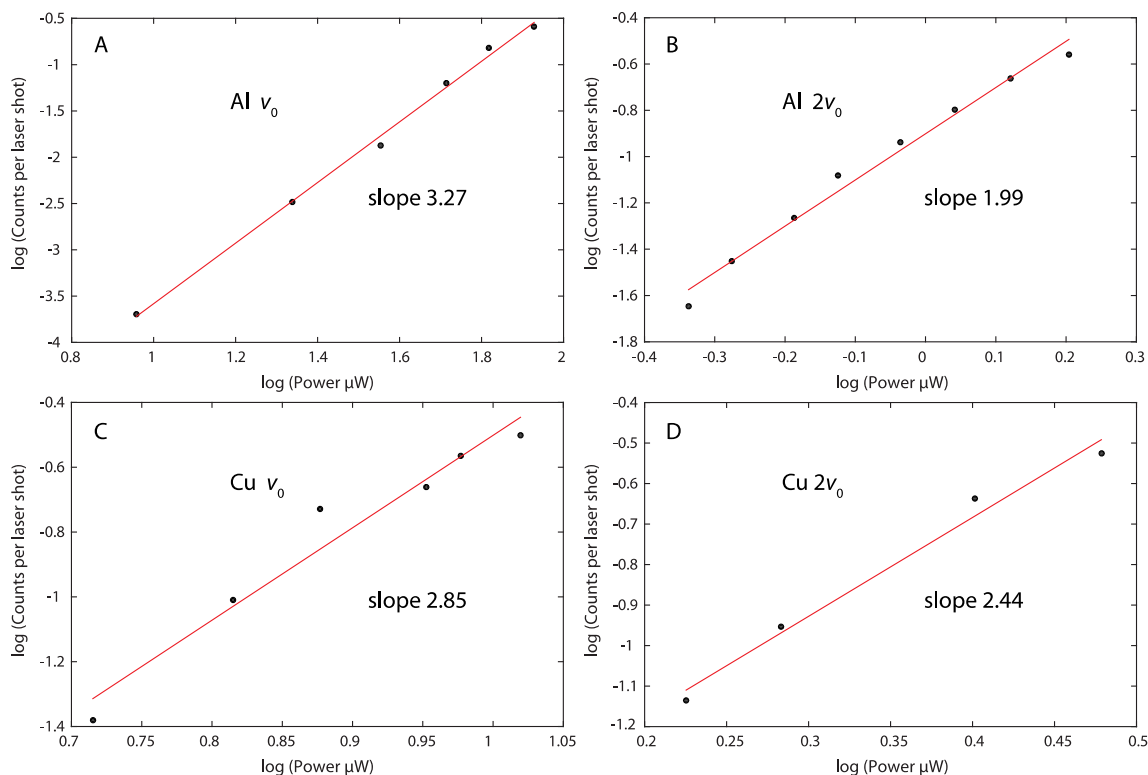
Figure 40: Log (power)-log (yield) plotting of Al and Cu samples. (a) and (b) Al sample irradiated by fundamental IR beam (frequency v_0) and frequency-doubled UV beam ($2v_0$). (c) and (d) Cu sample irradiated by IR (v_0) and UV beam ($2 v_0$). Red lines are linear fittings to experimental data points.

4.4 Hot carrier relaxation dynamics in graphene

4.4.1 Introduction

Graphene has attractive properties that have potential use in industrial applications, such as solar energy conversion and surface chemistry. Because of many attractive properties arising from its unique band-structure, graphene has been considered as one of the most promising materials for optoelectronic devices. Hot carrier dynamics in graphene receives much attention in the past decade. Theoretically, the lifetime of hot carriers in graphene should be quite long (hundreds of picoseconds to a few nanoseconds) due to a

high optical phonon energy (~200 meV) and restricted phase space for acoustic phonon emission[84]. Optical-pump terahertz/optical-prob differential transitivity spectroscopy has been exploited to study the hot-carrier relaxation dynamics.[85-94] Time- and angle-resolved photoemission spectroscopy (TR-ARPES) is another effective tool to probe the hot carrier dynamics in graphene. Multiple studies have been done to explore the thermalization and relaxation processes of hot carriers in graphene.[95-105] In these studies, the authors probed the hot carrier decay dynamics near K point because the photo excitations took place at K point (Dirac point), which has large parallel momentum (1.7 Å⁻¹). To excite the hot carriers at K point directly above vacuum level, they used relatively low energy photons (~1.5 eV) from ultrafast laser pulse as pump beam and high-energy photons (~30 eV) from HHG of fundamental IR beam as a probe beam. Theoretical calculations have also been carried out. These experimental and theoretical studies pictured the view of the hot carrier dynamics in graphene/graphite: (1) An optical pump pulse excites non-thermal distributed electrons; (2) These electrons get thermalized through carrier-carrier and carrier-phonon scattering in the timescale of ~30 fs; (3) Hot carriers cool down through optic phonon and acoustic phonon emissions afterwards within about 10 ps. One of the main reasons for a relatively short lifetime of hot carriers is that the excitation pulse energies are often high in the NIR and mid-IR region and extremely efficient carrier-carrier scattering can thermalize electron temperature to a few thousand Kelvins so that optical phonon emission becomes the dominant decay pathway. Supercollision involving multiple collisions between carriers and defects facilitating momentum transfer to acoustic phonons has also been proposed to explain the fast decay process when thermalized electron temperature is below optical phonon energy.[106-108] The fast decay of hot

carriers (similar to that of metal) and a very small bandgap seem to suggest that graphene might not be ideal for real applications. A recent study proposed to use tri-layer graphene with high carrier mobility to circumvent this problem [109].

Tielrooij et al. proposed a new intraband carrier multiplication process in doped graphene.[110] They suggested that an optical excited hot electron could generate secondary electron-hole pairs in the conduction band. Both excitation photon energy and beam fluence can affect this hot electron cascade generation. A recent study suggested a multiphoton thermionic photoemission from graphite.[111]

Thermionic emission takes place when electron temperature is high so that some electrons can overcome the work function of the surface to become free electrons. Because the thermionic emission is related to electron temperature, it is a good probe of carrier decay dynamics. Recent work has identified the pathways for thermionic emission from photo-excited graphite.[111]

Here, we employed the 3D momentum imaging system to detect the photoelectron momentum and angular distribution of graphene films deposited on fused silica, which shows directly the lifetime of hot electrons emitted by thermionic photoemission, without using time-resolved technique. We measured for the first time the decay of thermionic emission in graphene to the nanosecond range, which showed unexpected slow hot carriers dynamics.

4.4.2 3D momentum imaging system running at high repetition rate

The laser system we employed for this experiment is a mode-locked Ti:Sapphire laser with (the amplified beam repetition rate 2 kHz) and without an amplified system (a repetition rate of 80 MHz). The wavelength of the fundamental beam is 800 nm with 35 fs

pulse duration. Commercial chemical vapor deposition (CVD) graphene on fused silica surface (graphenesquare.com) was used without further modification or treatment. The sample was placed in a high vacuum chamber (~10^{-9} Torr) at room temperature. For comparison, we also performed experiments on a 10 *nm* thick copper film.

Inside the experimental chamber, we adopted a transmission geometry to measure photoemission from surface samples. The laser beam is introduced normally to the surface and the polarization is parallel to the sample surface. Photoelectrons emitted from the surfaces were accelerated with inhomogeneous electric fields (13 V/cm at the surface) towards the MCP detector, shown as a green hemisphere, and detected by the 3D imaging system (Figure 37). The obtained 3 coordinates (x, y, t) were used to calculate the 3D momentum of each electron, which could be then converted into energy and parallel momentum to produce a dispersion diagram. The details of the instrument were described in section 2. The VMI spectrometer can accept all the emitted photoelectrons, from -90° to 90° with respect to the surface normal, which helped achieve a high overall detection efficiency (>50%, limited by the quantum efficiency of MCPs) and enable single-particle detection at very low fluencies. Another benefit is that no need to rotate the sample or the detector to accept photoelectrons that have different polar angles with the surface normal. We would like to note that there have been great efforts[31, 112-113] in transferring the conventional VMI method from gas phase to surface studies. However, the 3D capability has been lacking until this work.

In the previous study, we demonstrated that the 3D momentum imaging system could be raised to run at 100 KHz from 1 KHz.[114] A coincidence experiment normally runs at a low count rate (0.1-1), so the camera was triggered for several laser shots instead

of being synchronized with a laser to increase the running rate to 100 KHz. In the new method, the camera run at 2 kHz and the exposure time covered the time window between two laser pulses. The digitizer was triggered by the electron signal from MCP. The difference between electron peak position and the laser pulse position that generated the electron(s) gives the electron TOF. In the post-analysis program, the built-in timestamps of camera and digitizer were compared to associate the digitizer traces and camera image pixels. In multi-hit events, the peaks were assigned by the linear correlation between the digitizer peak amplitude and camera image pixel intensity. [45]

The total average input power is 156 µW for the amplified laser beam and 71 mW for oscillator beam. The fluences of KHz laser is ~500 mJ/cm^2 and it is ~10 µJ/cm^2 for the oscillator beam. The thermionic emission is much stronger when the graphene sample was excited by oscillator beam (lower excitation fluence).

4.4.3 Results of graphene dynamics

The photoelectrons from the graphene surface have a semispherical-shape distribution but with tails compared to the electrons emitted from Cu (Figure 41). For a surface experiment with the transmission geometry we used here, electrons with backward velocity cannot be ejected from the surface, so there should no electron arrive later than zero-momentum electrons, and the momentum map should show clear cutoff at zero-momentum (shown as white line in Figure 41).
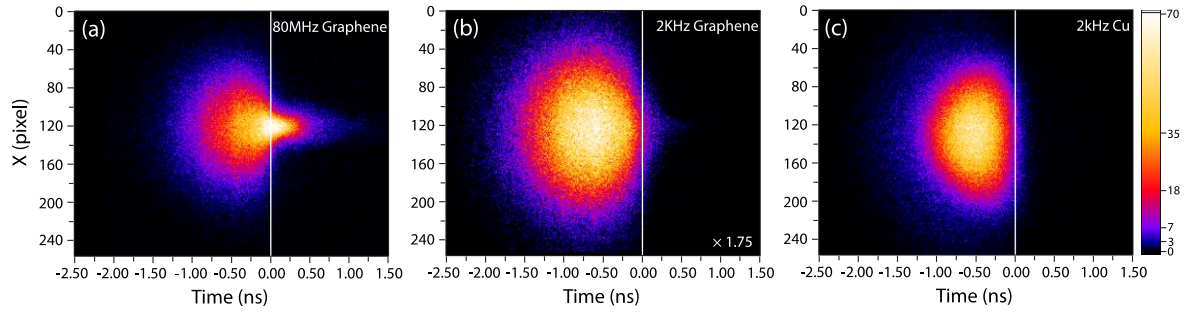
Figure 41: XZ images of electron velocity distributions: (a) Graphene at 80MHz, 10.4 $\mu J/cm^2$. (b) Graphene at 2kHz, 500 $\mu J/cm^2$ (c) Cu at 2kHz, 425 $\mu J/cm^2$.

In Figure 41 (a-c) we show the time-space (XZ) images of 3D electron Newton spheres. We define the TOF of electrons with zero momentum alone TOF as t_0, shown as white lines in Figure 41. In this case, the actual TOF is solely determined by the TOF tube length and electric fields. Other emitted electrons have momentum components along the surface normal towards the detector, so they arrive at detector earlier than t_0 and we indicate these electrons as minus sign in Figure 41. For a surface experiment with the transmission geometry we used here, electrons with Pz (P⊥) opposite to detector could not be ejected out of the surface, so the electron cloud is hemisphere like, with a clear cutoff at zero-momentum, as shown in Figure 41 (c), which shows electrons from thin Cu film at 173 $\mu J/cm^2$. The electron distributions of Graphene sample, however, have tails beyond t_0. Figure 41 (a) was obtained by exploiting the oscillator beam and the fluence was 10.4 $\mu J/cm^2$. Figure 41 (b) displays electrons pumped with the amplified laser beam, at fluence of 500 $\mu J/cm^2$. The image size of Figure 41 (a) is smaller than Figure 41 (b), indicating that the photoelectrons have lower kinetic energy release at lower laser fluence. The most intense electron distribution in Figure 41 (a) is around time zero, representing a lot of electrons have close-to-zero KE. On the other hand, the most distributed electrons in Figure 41 (b) have some "distance" from t_0, meaning more KE release and have a wider

momentum distribution than Figure 41 (a). Compared with the copper sample, graphene sample has electrons arriving after the time zero (positive time), especially at a low fluence. While positive time does not indicate momentum vectors inward the surface, such delayed arrival time can only be interpreted as delayed electron emission from the surface, *i.e.* an extended lifetime of hot carriers. At low fluencies, such a delay can be seen to go beyond one nanosecond. Such a slow decay of hot carriers in graphene is unprecedented at room temperature and indicates at low laser fluencies, a different decay or excitation mechanism is at play.
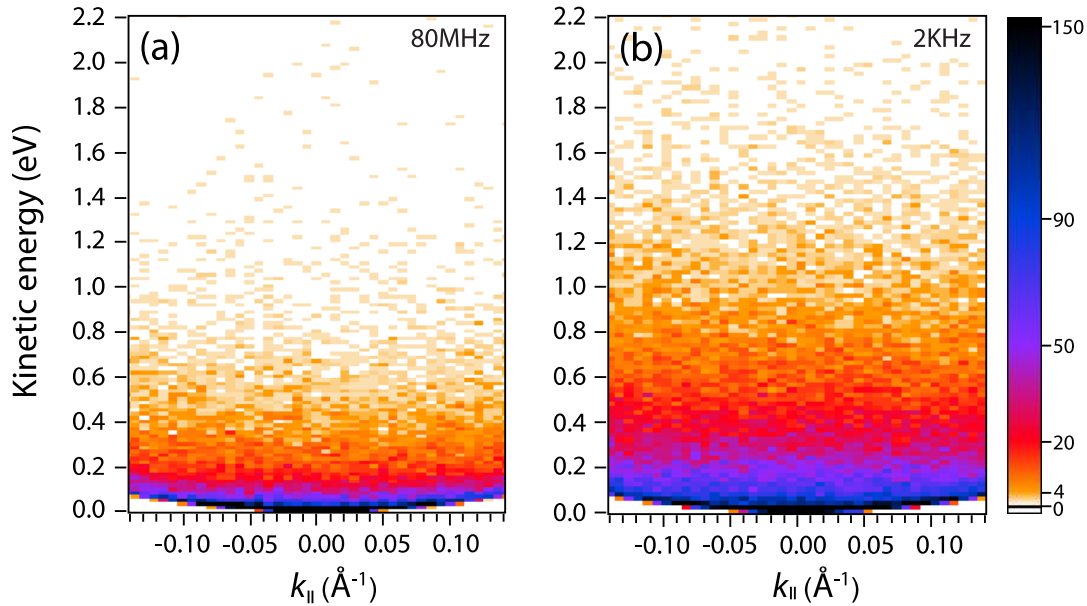
Figure 42: Energy dispersion graphs of graphene at different laser fluences: (a) 80 MHz, 12.3 μJ/cm². (b) 2KHz, 500 μJ/ cm².

By measuring the 2D positions of the electrons impacting on the detector and their TOFs, all three momentum vectors (p_x, p_y, p_z) can be calculated. The p_x and p_y can be used to compute the parallel momentum ($K_{//}$) to the surface, while all three momentum vectors are used to compute the kinetic energy using $KE = \sqrt{p_x^2 + p_y^2 + p_z^2}$. As with a conventional ARPES employing a hemisphere energy analyzer, these can be used to

construct the dispersion diagram to reveal band structures of materials. Figure 42 shows the energy dispersion diagrams at different laser fluences. We only displayed $K_\parallel$ in the range of -0.14 to 0.14 Å^{-1}. The amplified beam has higher energy per pulse (Figure 42 (b)), so the energy extends to higher values when comparing the same $k_\parallel$ value in these two figures. The reason is higher fluence gives a larger range of momentum and KE distribution; when $P_\parallel$ is same, larger Pz range gives a wide range of energy of dispersion. From the kinetic energy distributions, using a Boltzmann fitting, the electron temperature can be extracted to be ~3900 K and ~5300 K for Figure 42 (a) and (b), respectively. Figure 42 (b) and the fitted temperature are in good agreement with those of a previous multiphoton photoemission (mPP) measurement of graphite at a similar high fluence (500 $\mu J/cm^2$)[111].
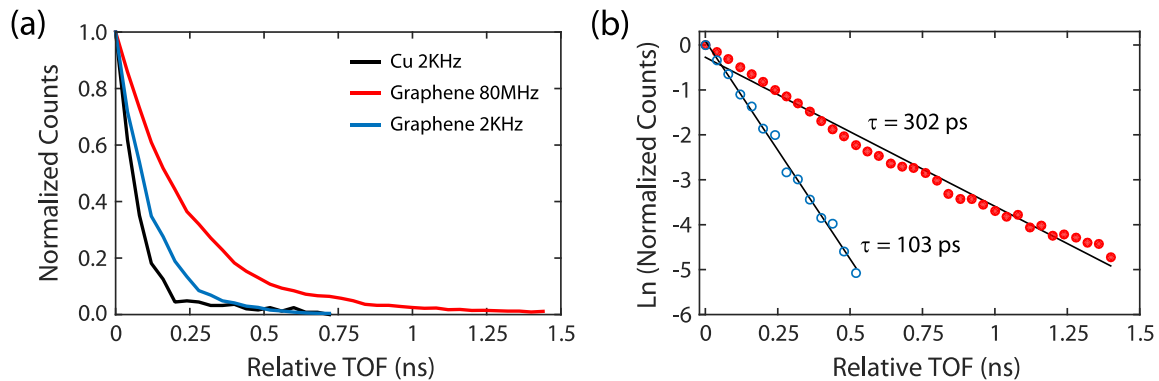
Figure 43: (a) TOF decay curve after t_0. 80MHz, 12.3 $\mu J/cm^2$, 2 kHz, 500 $\mu J/cm^2$. (b) Exponential decay fitting of graphene decay curves at different laser fluences. Red dots are natural log of normalized counts at 80 MHz. Blue circles are natural log of normalized counts at 80 MHz. Black lines are exponential fittings.

Figure 43 (a) shows the TOF decay curves after t_0. Counts are normalized to the highest intensity at t_0. This figure shows Cu has the fastest decay (mainly instrument response function and background). There are no long lifetime electrons for Cu at that fluence and little electron counts after t_0, barely seen in Figure 41 (c), so the baseline of Cu

decay curve looks noisy. An exponential decay fitting of the copper transient yields a decay rate constant of 64 ps, which indicates the lower limit of decay time measurement of our current method. It does not have a real physical meaning, so the exponential fitting of Cu is not displayed here. It can be seen that graphene at 80 MHz has a much slower decay rate (red curve in Figure 43 (a)) than at 2kHz (blue curve). The lifetime of hot electrons extends over 1 *ns* for graphene at 80 MHz. The exponential decay fitting of graphene shows that the lifetime of hot electrons in graphene at 12.3 $\mu J/cm^2$ have a decay constant of 302 ps. When using the amplified laser beam, the fitted decay constant is 103 ps. We note that the 100 *ps* is very close to the lower limit (64 *ps*) and suggests that this value might not be the real decay time of graphene hot carrier at high fluencies. Instead, this number could be an overall fitting result of background plus a very small contribution of the slow decay process. Indeed, at low fluencies, the signal after time zero contributes ~20% of the overall signal and increases as the fluence decreases, while for high fluencies, it is less than 4% of the total signal. Such a small signal level means that the decay dynamics at high fluencies can be easily overwhelmed by the background electrons. Therefore, from our current measurement, it is difficult to draw a conclusion on the decay time of carrier at high fluencies (~500 $\mu J/cm^2$). At lower fluencies, the fitted decay constants are reliable and show very little variation when fluencies are varied by about 200%. This suggests the slow decay dynamics do not change with fluence however its contribution to the total emission does change. A lot of previous studies have measured a lifetime of hot carriers in room temperature graphene to be a few *ps*, which is likely to be dominated by the fast decay processes due to employed higher fluencies. The observed lifetime of hot electrons by our high sensitive 3D detection system is orders of magnitude higher than the previous results.

Interestingly, a previous study pointed out that they observed two slow decay rates at a lower temperature (10 K) when the excitation energy was lower than optic phonon energy, 14~25 ps and ~300 ps.[92] The second time constant is very close to our result and was attributed to acoustic phonon scattering that leads to a very slow decay rate. In their study, when photon energy was 245 meV, the 300 ps decay component was unobservable. Here, the photon energy we used is 1.6 eV, so it is different decay mechanism at play.
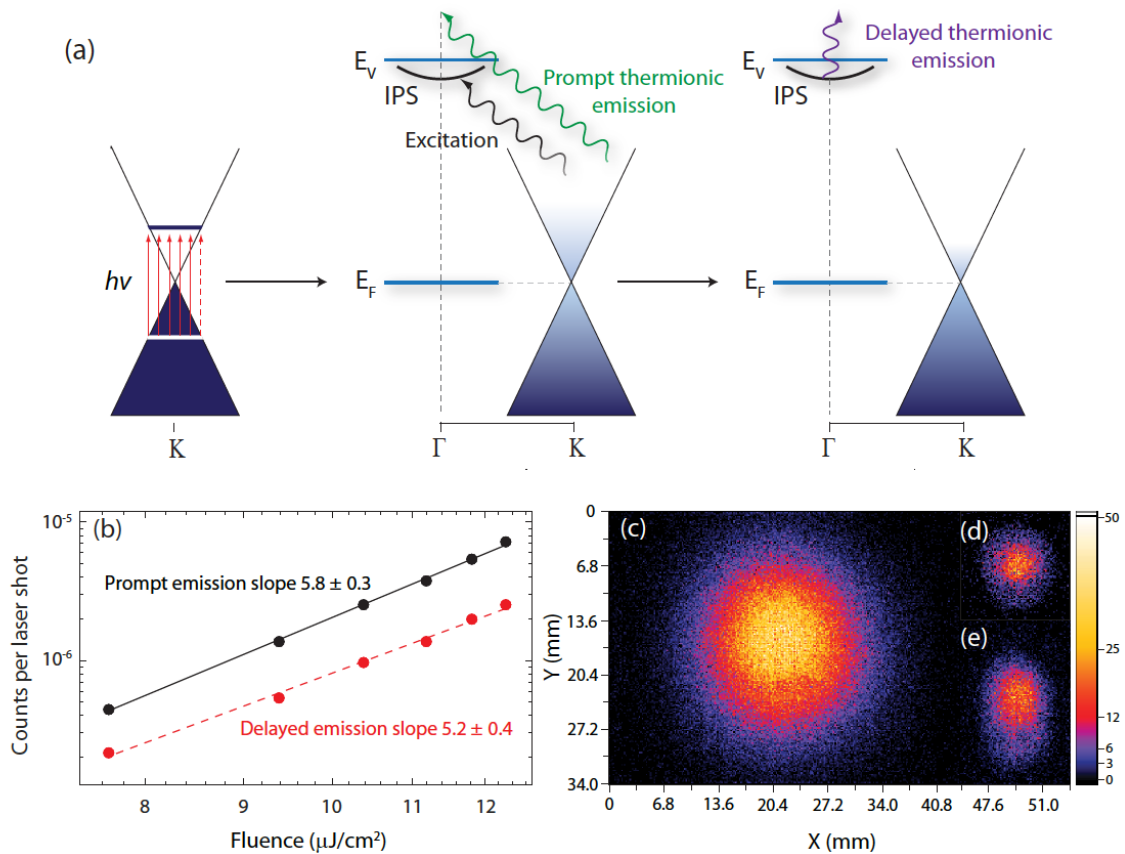
Figure 44: (a) Electronic excitation and decay processes in graphene. The red arrows in the left panel are the optical excitation at the K point. The green and black wavy arrows in the middle panel indicate the electron-electron scattering leading to prompt thermionic emission and excitation of IPS states, respectively. The main hot carrier distribution reaches a quasi-equilibrium through carrier-carrier scattering in the middle panel while quickly cools down through electron-phonon scattering in the right panel. (b) Fluence dependent photoemission yield at low fluencies. The prompt thermionic emission is for the electrons arriving before time zero while delayed emission is for electrons arriving after time zero. The slopes show the multiphoton orders of each process. (c) The XY distribution (spatial) of the prompt thermionic emission. (d) The XY distribution of delayed emission

with a round laser excitation spatial profile. (d) Same with (c), but with an elliptical laser profile. No size-scaling has been applied to (c) (d) (e).

Figure 44 (c) is an XY slice of electron distribution at 80 MHz. The slice range of TOF is from -1.25 ns to -0.5 ns (time axis in Figure 41(a)). The momentum distribution is isotropic. Figure 44 (d) and (e) show the XY sliced images of electron distribution after t_0, from 0.4 to 0.8 ns (Figure 41 (a)). The shapes of these XY images are originated from the different profile of the laser focusing spots. One is elliptical and the other one is round by adjusting the tilting of the focusing lens and reducing the beam size with an iris. The electrons before time zero were not affected, always isotropic regardless of different the laser profiles. This lead to the conclusion that the distribution of tail part electrons is spatial distributions instead of momentum distribution.

4.4.4 Estimating the work function of IPS states

Because the measured parallel momentum is very small, the emission has to proceed as thermionic emission at the Γ point while the excitation takes place at K point, which has significant parallel momentum. Strong electron scattering has been proposed to facilitate the electron energy thermalizing and transferring the excitation energy and momentum at K point to Γ point. This is shown as the green wavy arrow in Figure 3(a), middle panel. This is the excitation process of the *prompt* thermionic emission electrons (before time zero) in Figure 44 (a) and (b). Meanwhile, carrier scattering can also excite image potential states (IPS), from which electrons can easily escape to the vacuum level through thermionic emission. We believe these IPS states are the main source of the delay emission, which reflects the lifetime of IPS states. IPS states of graphene have been studied previously both theoretically and experimentally.[115-116] However, the lifetime of IPS states of graphene on fused silica has not been measured directly. Some previous work

measured the lifetime of IPS state of graphene on metal surfaces, which has been shown to be extremely short (~100 fs) due to the coupling between the IPS and surface states of metals. The current study employs fused silica as a substrate, which effectively decouples from the graphene and thus allows us to observe the inherent lifetime of IPS of graphene. Interestingly, delayed ionization was also observed in fullerene molecules, C_{60} and C_{70}, and was attributed to strong coupling between electronic and nuclear degrees of freedom.[117-118] Similarly, in graphene, the IPS state can couple to the lattice motion in the long-time scale and thus IPS electrons can be thermionically emitted. Here, the IPS state is also loosely coupled to the lattice motion and therefore a long lifetime is warranted. For thermionic emission, it is appropriate to use the Richardson-Dunshman equation[119],

$J = AT^2 e^{-\frac{\phi}{k_B T}}$, in which J is the current density, A is the Richardson constant (1.2×10^6 A·m^{-2}·K^{-2}), T is the temperature, Φ is the work function and k_B is the Boltzmann constant. If assuming a room temperature and using the measured electron count rate, a work function of ~1 eV is obtained, which is in reasonable agreement with previous results (0.85 eV).[115]

In order to use the Richardson-Dunshman equation[119]: $J = AT^2 e^{-\frac{\phi}{k_B T}}$, we need to calculate the current density from the measured count rate. We use the following equation to estimate the current density:

$$J = \frac{cts \cdot e}{area \cdot emission\ time}$$

in which *cts* is the count rate (counts/laser shot, 2×10^{-6} in our case assuming a 50% detection efficiency), *e* is the electron charge, *area* is the focused laser spot area and *emission time* is the decay time constant (302 *ps*). *Area* is computed with the measured

beam diameter of 70 μm. Because the decay of the delayed emission is exponential while conventional thermionic emission rates do not change with time, we assume the rate at time zero to be the thermionic emission rate. This leads to an effective emission time at the decay constant.

Using the computed the current density 3×10⁻⁷ A·m⁻² and assuming a room temperature, $\emptyset = 1.03$ eV is obtained. The use of a room temperature is justified by the large difference between the heat capacities of the electron (c_e) and the lattice (c_l) (c_e $< 10^{-3} c_l$) in graphene[120]. Even though the electron temperature can reach a few thousands of Kelvins, the lattice temperature increase is minimum.

Recently, a new thermionic equation was put forward by Liang et al., specifically for graphene[121]: $J = \beta T^3 e^{-\frac{\emptyset}{k_B T}}$, in which $\beta = 115.8\ A \cdot m^{-2} \cdot K^{-3}$. Using the same current density, we obtain $\emptyset = 0.97$ eV. The reasonable agreement between the estimated work function and previous measurements on IPS (0.8-0.9 eV)[115] confirms that delayed emission indeed arises from IPS.

We provide two more pieces of experimental evidence to support our interpretation: 1. the multiphoton orders of the direct and delayed emission were compared in Figure 44 (b), in which the power dependent electron yield is plotted in double-log axes and the slopes were extracted. We see both are between 5 and 6, which suggest 6-photon processes. The slight lower multiphoton order of the delay emission is likely to due to the fact that the energy of the IPS is lying just below the vacuum level for direct thermionic emission. 2. Because the IPS states are located near Γ point, the parallel momentum should be very small. In Figure 44, we compared the parallel momenta of *prompt* (Figure 44 (c)) and *delayed* emission (Figure 44 (d) (e)). Indeed, the parallel momentum of delayed emission

is quite small, less than 0.08 A^{-1}. Interestingly, due to this small momentum, we can now directly image the focused laser beam profile on the graphene surface. Figure 44 (d) is the case when the laser profile is made to be round with an aperture while Figure 44 (e) is when we send in an unclipped beam that is elliptically-shaped.

4.4.5 Conclusion

To conclude, we have employed a novel TOF-ARPES to investigate hot carrier dynamics. The TOF capability enables us to directly measure the lifetime of hot carriers in graphene at long timescale without a pump-probe setup. It is found that hot carriers in graphene can be excited to image potential states and have a long lifetime at low laser fluencies. It should be interesting to investigate how important these IPS electrons are at even lower laser fluencies and whether these carriers can be effectively extracted to implement optoelectric devices.

SUMMARIES AND FUTURE DIRECTIONS

On the instrumentation aspect, an VMI electron/ion optics was designed with a trajectory simulation software SIMION. A machine was built that includes the constructed VMI optics, a supersonic gas jet and 3D momentum imaging system to implement coincidence measurements for gas phase molecules. The machine functioning was tested with strong field ionization of CH_3I and Ar. This machine was also enabled to carry out time-of-flight angular-resolved photoemission spectroscopy (TOF-ARPES) to study surface dynamics of condensed phase materials. Labview programs were upgraded to enable electron-ion coincidence measurements with one digitizer and two cameras through pulsing electrodes. We developed a new strategy to remove the repetition rate barrier of the 3D detection system and make it to be compatible with 80 MHz laser.

On the molecular and surface dynamics aspect, we studied ionization/dissociation dynamics of camphor in mid-intensity laser field. In the mass spectrum, the peak of parent ion had strongest intensity. Meanwhile, some parent ions were highly fragmented through many different single and double ionization pathways, leading to various monocations. Only one double ionization and dissociation channel was reported in a previous study. Here, we confirmed more than twenty double ionization pathways through ion-ion coincidence map. We examined the electron momentum distribution in camphor enantiomers with circularly and elliptically polarized light. Asymmetric distributions were observed along the laser propagation direction in previous studies. In our experiments, the asymmetric signature was first observed but diminished after we accumulated more ionization events. We also checked the distributions in the polarization plane. The subtraction of the YZ images arising from camphor enantiomers did not show obvious asymmetry. We then

calculated the asymmetric factor for forward and backward electrons along the TOF axis, which was the major axis of the laser polarization ellipse. The time resolution was not enough to extract a clear conclusion along this axis.

We also studied the single and double ionization/dissociation dynamics of PENNA in mid-intensity laser field. The major products were dimethylamine from single ionization. The yield of parent ions was about 5% of the major products. The previous studies of PENNA mainly focused on single ionizations. We observed clear double ionization signatures in the momentum images and confirmed the major double ionization/dissociation pathway through ion-ion coincidence map. By comparing experimental kinetic energy release of the ion pairs to DFT computational results, we demonstrated the open-shell single diradicals were the main products of strong field double ionization, which dissociated into dimethylamine and benzyl monocation through the singlet potential energy surface.

We employed TOF-ARPES to study surface dynamics. Different from the reflection geometry in "traditional" ARPES, we exploited transmission geometry to send lasers beams perpendicular to surface samples. We studied multiphoton photoemission in thin metal films (Al and Cu) with laser beams at different wave lengths, 800 nm, 400 nm, and 276 nm. We observed hemispherical electron momentum distributions from Cu film. For both Al and Cu samples, the linear fittings of log (intensity)-log (yield) plottings show that it was a three-photon process for the fundamental beam and two-photon process for the frequency-doubled UV beam.

We studied hot carrier decay dynamics in graphene. The 3D momentum imaging capability allowed us to measure the decay time without a pump-probe scheme. We

observed extremely long hot carrier decay at room temperature and low laser fluence (~10 $\mu J/cm^2$). This delayed emission persisted over 1 *ns*, two orders of magnitude longer than previous reported values, most of which were several *ps*. From the Richardson-Dunshman equation, we obtained a work function ~1 eV. A prominent candidate is image potential state (IPS). We proposed that hot carriers in graphene can be excited to IPSs and have a long lifetime at low laser fluencies.

In mid-intensity field ionization of camphor, we did not observe clear asymmetric distribution of photoelectrons in the laser polarization plane. The asymmetric signature could be diminished after averaging all molecular orientations. Our group has showed recoil-frame electron distribution by coincidence detection of electron and I^+ arising from single ionization and dissociation of CH_3I. [57] In the future, we could try to construct 3D electron distributions in chiral molecular frames. The camphor molecules may not be the best candidate because they are highly fragmented in mid-intensity laser field and have many different single and double ionization/dissociation channels. To demonstrate the methodology, simpler chiral molecules might be ideal.

To study relatively large molecules that are in liquid or solid phase at room temperature, we heated the samples and supersonic gas jet to transfer gas-phase big molecules. The molar mass of the molecules we studies were around 150 g/mol (Dalton). There should be a size limit of molecules that can be heated and studied in gas phase, at which the vaporization rate would be too slow to obtain enough target molecules. Another way to study lager size molecules/complexes/crystals and break the limit of heating samples is to deposit solid phase sample to a plate to carry out surface studies. This will allow the study of peptides, proteins, polymers, light harvesting crystals, etc. Matrix-

assisted laser desorption/ionization (MALDI) provides the mass spectra of ion fragments. Different from MALDI, VMI-beased TOF-ARPES will also allow the detection of energy, momentum and angular distribution of ion/anion fragments and electrons, which will provide information on the desorption and dissociation dynamics, instead of only provide mass spectra.

REFERENCES

[1]   Ullrich, J.; Moshammer, R.; Dörner, R.; Jagutzki, O.; Mergel, V., et al., *Recoil-ion momentum spectroscopy.* J. Phys. B: At. Mol. Opt. Phys. **1997,** 30, 2917.

[2]   Ullrich, J.; Moshammer, R.; Dorn, A.; Dörner, R.; Schmidt, L. P. H., et al., *Recoil-ion and electron momentum spectroscopy: reaction-microscopes.* Rep. Prog. Phys. **2003,** 66, 1463.

[3]   KELDYSH, L. V., *Ionization in the field of a strong electromagnetic wave.* VOVIET PHYSICS JETP **1965,** 20, 1307-1314.

[4]   Faisal, F. H. M., *Multiple absorption of laser photons by atoms.* J. Phys. B: At. Mol. Phys. **1973,** 6, L89.

[5]   Reiss, H. R., *Effect of an intense electromagnetic field on a weakly bound system.* Phys. Rev. A **1980,** 22, 1786-1813.

[6]   Pukhov, A., *Strong field interaction of laser radiation.* Rep. Prog. Phys. **2003,** 66, 47-101.

[7]   Moulton, P. F., *Spectroscopic and laser characteristics of Ti:Al2O3.* J. Opt. Soc. Am. B **1986,** 3, 125-133.

[8]   Kapteyn, H.; Cohen, O.; Christov, I.; Murnane, M., *Harnessing Attosecond Science in the Quest for Coherent X-rays.* Science **2007,** 317, 775-778.

[9]   Eckle, P.; Pfeiffer, A. N.; Cirelli, C.; Staudte, A.; Dörner, R., et al., *Attosecond Ionization and Tunneling Delay Time Measurements in Helium.* Science **2008,** 322, 1525-1529.

[10]   Eckle, P.; Smolarski, M.; Schlup, P.; Biegert, J.; Staudte, A., et al., *Attosecond angular streaking.* Nat. Phys. **2008,** 4, 565-570.

[11] Pfeiffer, A. N.; Cirelli, C.; Smolarski, M.; Dorner, R.; Keller, U., *Timing the release in sequential double ionization.* Nat. Phys. **2011,** 7, 428-433.

[12] Uiberacker, M.; Uphues, T.; Schultze, M.; Verhoef, A. J.; Yakovlev, V., et al., *Attosecond real-time observation of electron tunnelling in atoms.* Nature **2007,** 446, 627.

[13] Krausz, F.; Ivanov, M., *Attosecond physics.* Rev. Mod. Phys. **2009,** 81, 163-234.

[14] Tzallas, P.; Charalambidis, D.; Papadogiannis, N. A.; Witte, K.; Tsakiris, G. D., *Direct observation of attosecond light bunching.* Nature **2003,** 426, 267-271.

[15] Hentschel, M.; Kienberger, R.; Spielmann, C.; Reider, G. A.; Milosevic, N., et al., *Attosecond metrology.* Nature **2001,** 414, 509-513.

[16] Kienberger, R.; Hentschel, M.; Uiberacker, M.; Spielmann, C.; Kitzler, M., et al., *Steering Attosecond Electron Wave Packets with Light.* Science **2002,** 297, 1144-1148.

[17] Kienberger, R.; Goulielmakis, E.; Uiberacker, M.; Baltuska, A.; Yakovlev, V., et al., *Atomic transient recorder.* Nature **2004,** 427, 817-821.

[18] Paul, P. M.; Toma, E. S.; Breger, P.; Mullot, G.; Augé, F., et al., *Observation of a Train of Attosecond Pulses from High Harmonic Generation.* Science **2001,** 292, 1689-1692.

[19] López-Martens, R.; Varjú, K.; Johnsson, P.; Mauritsson, J.; Mairesse, Y., et al., *Amplitude and Phase Control of Attosecond Light Pulses.* Phys. Rev. Lett. **2005,** 94, 033001.

[20] Laurent, G.; Cao, W.; Li, H.; Wang, Z.; Ben-Itzhak, I., et al., *Attosecond Control of Orbital Parity Mix Interferences and the Relative Phase of Even and Odd Harmonics in an Attosecond Pulse Train.* Phys. Rev. Lett. **2012,** 109, 083001.

[21] Freeman, R. R.; McIlrath, T. J.; Bucksbaum, P. H.; Bashkansky, M., *Pondermotive effects on angular distributions of photoelectrons.* Phys. Rev. Lett. **1986,** 57, 3156-3159.

[22] Zipp, L. J.; Natan, A.; Bucksbaum, P. H., *Probing electron delays in above-threshold ionization.* Optica **2014,** 1, 361-364.

[23] Giusti-Suzor, A.; He, X.; Atabek, O.; Mies, F. H., *Above-threshold dissociation of H_2^+ in intense laser fields.* Phys. Rev. Lett. **1990,** 64, 515-518.

[24] Bucksbaum, P. H.; Zavriyev, A.; Muller, H. G.; Schumacher, D. W., *Softening of the H_2^+ molecular bond in intense laser fields.* Phys. Rev. Lett. **1990,** 64, 1883-1886.

[25] Hufner, S., *Photoelectron Spectroscopy Principles and Applications.*

[26] Law, A. R.; Barry, J. J.; Hughes, H. P., *Angle-resolved photoemission and secondary electron emission from single-crystal graphite.* Phys. Rev. B **1983,** 28, 5332-5335.

[27] Höfer, U.; Shumay, I. L.; Reuß, C.; Thomann, U.; Wallauer, W., et al., *Time-Resolved Coherent Photoelectron Spectroscopy of Quantized Electronic States on Metal Surfaces.* Science **1997,** 277, 1480-1482.

[28] Cavalieri, A. L.; Müller, N.; Uphues, T.; Yakovlev, V. S.; Baltuška, A., et al., *Attosecond spectroscopy in condensed matter.* Nature **2007,** 449, 1029.

[29]   Kirchmann, P. S.; Rettig, L.; Nandi, D.; Lipowski, U.; Wolf, M., et al., *A time-of-flight spectrometer for angle-resolved detection of low energy electrons in two dimensions.* Appl. Phys. A **2008,** 91, 211-217.

[30]   Hong Ye, S. T., Michele Di Fraia, Arya Fallahi, Oliver D. Mücke, Franz X. Kärtner, and Jochen Küpper, *Velocity-map imaging for emittance characterization of multiphoton-emitted electrons from a gold surface.* arXiv:1707.06472 **2017**.

[31]   Monti, O. L. A.; Baker, T. A.; Nesbitt, D. J., *Imaging nanostructures with scanning photoionization microscopy.* J. Chem. Phys. **2006,** 125, 154709.

[32]   Schweikhard, V.; Grubisic, A.; Baker, T. A.; Thomann, I.; Nesbitt, D. J., *Polarization-Dependent Scanning Photoionization Microscopy: Ultrafast Plasmon-Mediated Electron Ejection Dynamics in Single Au Nanorods.* ACS Nano **2011,** 5, 3724-3735.

[33]   Eppink, A. T. J. B.; Parker, D. H., *Velocity map imaging of ions and electrons using electrostatic lenses: Application in photoelectron and photofragment ion imaging of molecular oxygen.* Rev. Sci. Instrum. **1997,** 68, 3477-3484.

[34]   McLaren, W. C. W. a. I. H., *Time‑of‑Flight Mass Spectrometer with Improved Resolution.* Rev. Sci. Instrum. **1955,** 26, 1150-1157.

[35]   Gebhardt, C. R.; Rakitzis, T. P.; Samartzis, P. C.; Ladopoulos, V.; Kitsopoulos, T. N., *Slice imaging: A new approach to ion imaging and velocity mapping.* Rev. Sci. Instrum. **2001,** 72, 3848-3853.

[36]   Townsend, D.; Minitti, M. P.; Suits, A. G., *Direct current slice imaging.* Rev. Sci. Instrum. **2003,** 74, 2530-2539.

[37]   Lin, J. J.; Zhou, J.; Shiu, W.; Liu, K., *Application of time-sliced ion velocity imaging to crossed molecular beam experiments.* Rev. Sci. Instrum. **2003,** 74, 2495-2500.

[38]   Ryazanov, M.; Reisler, H., *Improved sliced velocity map imaging apparatus optimized for H photofragments.* J. Chem. Phys. **2013,** 138, 144201.

[39]   Kling, N. G.; Paul, D.; Gura, A.; Laurent, G.; De, S., et al., *Thick-lens velocity-map imaging spectrometer with high resolution for high-energy charged particles.* Journal of Instrumentation **2014,** 9, P05005.

[40]   Skruszewicz, S.; Passig, J.; Przystawik, A.; Truong, N. X.; Köther, M., et al., *A new design for imaging of fast energetic electrons.* Int. J. Mass spectrom. **2014,** 365-366, 338-342.

[41]   Golovin, A. V.; Heiser, F.; Quayle, C. J. K.; Morin, P.; Simon, M., et al., *Observation of Site-Specific Electron Emission in the Decay of Superexcited ${O}_{2}$.* Phys. Rev. Lett. **1997,** 79, 4554-4557.

[42]   Lafosse, A.; Lebech, M.; Brenot, J. C.; Guyon, P. M.; Jagutzki, O., et al., *Vector Correlations in Dissociative Photoionization of Diatomic Molecules in the VUV Range: Strong Anisotropies in Electron Emission from Spatially Oriented NO Molecules.* Phys. Rev. Lett. **2000,** 84, 5987-5990.

[43]   Vredenborg, A.; Roeterdink, W. G.; Janssen, M. H. M., *A photoelectron-photoion coincidence imaging apparatus for femtosecond time-resolved molecular dynamics with electron time-of-flight resolution of σ =18ps and energy resolution $\triangle E / E$=3.5%.* Rev. Sci. Instrum. **2008,** 79, 063108.

[44]   Cao, W.; Laurent, G.; Ben-Itzhak, I.; Cocke, C. L., *Identification of a Previously Unobserved Dissociative Ionization Pathway in Time-Resolved Photospectroscopy of the Deuterium Molecule.* Phys. Rev. Lett. **2015,** 114, 113001.

[45]   Lee, S. K.; Cudry, F.; Lin, Y. F.; Lingenfelter, S.; Winney, A. H., et al., *Coincidence ion imaging with a fast frame camera.* Rev. Sci. Instrum. **2014,** 85, 123303.

[46]   Lee, S. K.; Lin, Y. F.; Lingenfelter, S.; Fan, L.; Winney, A. H., et al., *Communication: Time- and space-sliced velocity map electron imaging.* J. Chem. Phys. **2014,** 141, 221101.

[47]   Lin, Y. F.; Lee, S. K.; Adhikari, P.; Herath, T.; Lingenfelter, S., et al., *Note: An improved 3D imaging system for electron-electron coincidence measurements.* Rev. Sci. Instrum. **2015,** 86, 096110.

[48]   Liu, H.; Yang, Z.; Gao, Z.; Tang, Z., *Ionization and dissociation of CH3I in intense laser field.* J. Chem. Phys. **2007,** 126, 044316.

[49]   Wang, Y.; Zhang, S.; Wei, Z.; Zhang, B., *Velocity Map Imaging of Dissociative Ionization and Coulomb Explosion of CH3I Induced by a Femtosecond Laser.* J. Phys. Chem. A **2008,** 112, 3846-3851.

[50]   Böwering, N.; Lischke, T.; Schmidtke, B.; Müller, N.; Khalil, T., et al., *Asymmetry in Photoelectron Emission from Chiral Molecules Induced by Circularly Polarized Light.* Phys. Rev. Lett. **2001,** 86, 1187-1190.

[51]   Garcia, G. A.; Nahon, L.; Lebech, M.; Houver, J.-C.; Dowek, D., et al., *Circular dichroism in the photoelectron angular distribution from randomly oriented enantiomers of camphor.* J. Chem. Phys. **2003,** 119, 8781-8784.

[52]   Christian Lux; Matthias Wollenhaupt; Tom Bolze; Qingqing Liang; Jens Köhler, et al., *Circular Dichroism in the Photoelectron Angular Distributions of Camphor and Fenchone from Multiphoton Ionization with Femtosecond Laser Pulses.* Angew. Chem. Int. Ed. **2012,** 51, 5001-5005.

[53]   Christian, L.; Arne, S.; Cristian, S.; Matthias, W.; Thomas, B., *Photoelectron circular dichroism observed in the above-threshold ionization signal from chiral molecules with femtosecond laser pulses.* J. Phys. B: At. Mol. Opt. Phys. **2016,** 49, 02LT01.

[54]   Ferré, A.; Handschin, C.; Dumergue, M.; Burgy, F.; Comby, A., et al., *A table-top ultrashort light source in the extreme ultraviolet for circular dichroism experiments.* Nature Photonics **2014,** 9, 93.

[55]   Beaulieu, S.; Comby, A.; Clergerie, A.; Caillat, J.; Descamps, D., et al., *Attosecond-resolved photoionization of chiral molecules.* Science **2017,** 358, 1288-1294.

[56]   de Castilho, R. B.; Ramalho, T. C.; Nunez, C. V.; Coutinho, L. H.; Santos, A. C. F., et al., *Single and double ionization of the camphor molecule excited around the C 1s edge.* Rapid Commun. Mass Spectrom. **2014,** 28, 1769-1776.

[57]   Winney, A. H.; Basnayake, G.; Debrah, D. A.; Lin, Y. F.; Lee, S. K., et al., *Disentangling Strong-Field Multielectron Dynamics with Angular Streaking.* J. Phys. Chem. Lett. **2018,** 9, 2539-2545.

[58]   Danby, C. J.; Eland, J. H. D., *Photoelectron-photoion coincidence spectroscopy: II. Design and performance of a practical instrument.* Int. J. Mass Spectrom. Ion Phys. **1972,** 8, 153-161.

[59]   Powis, I.; Mansell, P. I.; Danby, C. J., *A photoelectron-photoion coincidence spectrometer for the study of translational energy release distributions.* Int. J. Mass Spectrom. Ion Phys. **1979,** 32, 15-26.

[60]   Baer, T., *Ion dissociation dynamics and thermochemistry by photoelectron photoion coincidence (PEPICO) spectroscopy.* Int. J. Mass spectrom. **2000,** 200, 443-457.

[61]   Sztáray, B.; Baer, T., *Suppression of hot electrons in threshold photoelectron photoion coincidence spectroscopy using velocity focusing optics.* Rev. Sci. Instrum. **2003,** 74, 3763-3768.

[62]   Davies, J. A.; LeClaire, J. E.; Continetti, R. E.; Hayden, C. C., *Femtosecond time-resolved photoelectron–photoion coincidence imaging studies of dissociation dynamics.* J. Chem. Phys. **1999,** 111, 1-4.

[63]   Lebech, M.; Houver, J. C.; Dowek, D., *Ion–electron velocity vector correlations in dissociative photoionization of simple molecules using electrostatic lenses.* Rev. Sci. Instrum. **2002,** 73, 1866-1874.

[64]   Rijs, A. M.; Janssen, M. H. M.; Chrysostom, E. t. H.; Hayden, C. C., *Femtosecond Coincidence Imaging of Multichannel Multiphoton Dynamics.* Phys. Rev. Lett. **2004,** 92, 123002.

[65]   Rolles, D.; Pešić, Z. D.; Perri, M.; Bilodeau, R. C.; Ackerman, G. D., et al., *A velocity map imaging spectrometer for electron–ion and ion–ion coincidence experiments with synchrotron radiation.* Nucl. Instrum. Methods Phys. Res., Sect. B **2007,** 261, 170-174.

[66]   Winney, A. H.; Lee, S. K.; Lin, Y. F.; Liao, Q.; Adhikari, P., et al., *Attosecond Electron Correlation Dynamics in Double Ionization of Benzene Probed with Two-Electron Angular Streaking.* Phys. Rev. Lett. **2017,** 119, 123201.

[67]   Winney, A. H.; Lin, Y. F.; Lee, S. K.; Adhikari, P.; Li, W., *State-resolved three-dimensional electron-momentum correlation in nonsequential double ionization of benzene.* Phys. Rev. A **2016,** 93, 031402.

[68]   Weinkauf, R.; Lehr, L.; Metsala, A., *Local Ionization in 2-Phenylethyl-N,N-dimethylamine: Charge Transfer and Dissociation Directly after Ionization.* J. Phys. Chem. A **2003,** 107, 2787-2799.

[69]   Lünnemann, S.; Kuleff, A. I.; Cederbaum, L. S., *Ultrafast charge migration in 2-phenylethyl-N, N-dimethylamine.* Chem. Phys. Lett. **2008,** 450, 232.

[70]   Lünnemann, S.; Kuleff, A. I.; Cederbaum, L. S., *Charge migration following ionization in systems with chromophore-donor and amine-acceptor sites.* J. Chem. Phys. **2008,** 129, 104305.

[71]   Bush, J. C.; Minitti, M. P.; Weber, P. M., *Dissociative Energy Flow, Vibrational Energy Redistribution, and Conformeric Structural Dynamics in Bifunctional Amine Model Systems.* J. Phys. Chem. A **2010,** 114, 11078-11084.

[72]   Jenkins, A. J.; Vacher, M.; Bearpark, M. J.; Robb, M. A., *Nuclear spatial delocalization silences electron density oscillations in 2-phenyl-ethyl-amine (PEA) and 2-phenylethyl-N,N-dimethylamine (PENNA) cations.* J. Chem. Phys. **2016,** 144, 104110.

[73]   Mignolet, B.; Levine, R. D.; Remacle, F., *Charge Migration in the Bifunctional PENNA Cation Induced and Probed by Ultrafast Ionization: A Dynamical Study.* J. Phys. B **2014,** 47, 124011.

[74]   Mignolet, B.; Levine, R. D.; Remacle, F., *Charge migration in the bifunctional PENNA cation induced and probed by ultrafast ionization: a dynamical study.* J. Phys. B: At. Mol. Opt. Phys. **2014,** 47, 124011.

[75]   Cheng, W.; Kuthirummal, N.; Gosselin, J. L.; Sølling, T. I.; Weinkauf, R., et al., *Control of Local Ionization and Charge Transfer in the Bifunctional Molecule 2-Phenylethyl-N,N-dimethylamine Using Rydberg Fingerprint Spectroscopy.* J. Phys. Chem. A **2005,** 109, 1920-1925.

[76]   Lehr, L.; Horneff, T.; Weinkauf, R.; Schlag, E. W., *Femtosecond Dynamics after Ionization: 2-Phenylethyl-N,N-dimethylamine as a Model System for Nonresonant Downhill Charge Transfer in Peptides.* J. Phys. Chem. A **2005,** 109, 8074-8080.

[77]   Chai, J.-D.; Head-Gordon, M., *Long-range corrected hybrid density functionals with damped atom-atom dispersion corrections.* PCCP **2008,** 10, 6615-6620.

[78]   Dennington, R.; Keith, T.; Millam, J. *GaussView, version 5*, Semichem Inc.: Shawnee Mission, KS, 2009.

[79]   Shoutian Sun, B. M., Lin Fan, Wen Li, R. D. Levine and F. Remacle, *Nuclear Motion Driven Ultrafast PHotodissociative Charge Transfer of PENNA Cation: An Experimental and Computational Study.* J. Phys. Chem. A **2017,** 121, 1442-1447.

[80]   Lehmann, C. S.; Ram, N. B.; Janssen, M. H. M., *Velocity map photoelectron-photoion coincidence imaging on a single detector.* Rev. Sci. Instrum. **2012,** 83, 093103.

[81]   Hemmers, O.; Whitfield, S. B.; Glans, P.; Wang, H.; Lindle, D. W., et al., *High-resolution electron time-of-flight apparatus for the soft x-ray region.* Rev. Sci. Instrum. **1998,** 69, 3809-3817.

[82]   Takahashi, K.; Azuma, J.; Kamada, M., *Two-dimensional band dispersion and momentum-resolved lifetime of the image-potential state on graphite studied by angle-resolved multiphoton photoemission spectroscopy.* Phys. Rev. B **2012,** 85, 075325.

[83]   Lehmann, J.; Merschdorf, M.; Thon, A.; Voll, S.; Pfeiffer, W., *Properties and dynamics of the image potential states on graphite investigated by multiphoton photoemission spectroscopy.* Phys. Rev. B **1999,** 60, 17037-17045.

[84]   Bistritzer, R.; MacDonald, A. H., *Electronic Cooling in Graphene.* Phys. Rev. Lett. **2009,** 102, 206410.

[85]   Dawlaty, J. M.; Shivaraman, S.; Chandrashekhar, M.; Rana, F.; Spencer, M. G., *Measurement of ultrafast carrier dynamics in epitaxial graphene.* Appl. Phys. Lett. **2008,** 92, 042116.

[86]   George, P. A.; Strait, J.; Dawlaty, J.; Shivaraman, S.; Chandrashekhar, M., et al., *Ultrafast Optical-Pump Terahertz-Probe Spectroscopy of the Carrier Relaxation and Recombination Dynamics in Epitaxial Graphene.* Nano Lett. **2008,** 8, 4248-4251.

[87] Sun, D.; Wu, Z.-K.; Divin, C.; Li, X.; Berger, C., et al., *Ultrafast Relaxation of Excited Dirac Fermions in Epitaxial Graphene Using Optical Differential Transmission Spectroscopy.* Phys. Rev. Lett. **2008,** 101, 157402.

[88] Breusing, M.; Ropers, C.; Elsaesser, T., *Ultrafast Carrier Dynamics in Graphite.* Phys. Rev. Lett. **2009,** 102, 086809.

[89] Wang, H.; Strait, J. H.; George, P. A.; Shivaraman, S.; Shields, V. B., et al., *Ultrafast relaxation dynamics of hot optical phonons in graphene.* Appl. Phys. Lett. **2010,** 96, 081917.

[90] Breusing, M.; Kuehn, S.; Winzer, T.; Malić, E.; Milde, F., et al., *Ultrafast nonequilibrium carrier dynamics in a single graphene layer.* Phys. Rev. B **2011,** 83, 153410.

[91] Strait, J. H.; Wang, H.; Shivaraman, S.; Shields, V.; Spencer, M., et al., *Very Slow Cooling Dynamics of Photoexcited Carriers in Graphene Observed by Optical-Pump Terahertz-Probe Spectroscopy.* Nano Lett. **2011,** 11, 4902-4906.

[92] Winnerl, S.; Orlita, M.; Plochocka, P.; Kossacki, P.; Potemski, M., et al., *Carrier Relaxation in Epitaxial Graphene Photoexcited Near the Dirac Point.* Phys. Rev. Lett. **2011,** 107, 237401.

[93] Brida, D.; Tomadin, A.; Manzoni, C.; Kim, Y. J.; Lombardo, A., et al., *Ultrafast collinear scattering and carrier multiplication in graphene.* Nat. Commun. **2013,** 4, 1987.

[94] Trushin, M.; Grupp, A.; Soavi, G.; Budweg, A.; De Fazio, D., et al., *Ultrafast pseudospin dynamics in graphene.* Phys. Rev. B **2015,** 92, 165429.

[95] Bostwick, A.; Ohta, T.; Seyller, T.; Horn, K.; Rotenberg, E., *Quasiparticle dynamics in graphene.* Nat. Phys. **2007,** 3, 36-40.

[96] Kang, K.; Abdula, D.; Cahill, D. G.; Shim, M., *Lifetimes of optical phonons in graphene and graphite by time-resolved incoherent anti-Stokes Raman scattering.* Phys. Rev. B **2010,** 81, 165405.

[97] Gilbertson, S.; Dakovski, G. L.; Durakiewicz, T.; Zhu, J.-X.; Dani, K. M., et al., *Tracing Ultrafast Separation and Coalescence of Carrier Distributions in Graphene with Time-Resolved Photoemission.* J. Phys. Chem. Lett. **2012,** 3, 64-68.

[98] Gierz, I.; Petersen, J. C.; Mitrano, M.; Cacho, C.; Turcu, I. C. E., et al., *Snapshots of non-equilibrium Dirac carrier distributions in graphene.* Nat. Mater. **2013,** 12, 1119-1124.

[99] Johannsen, J. C.; Ulstrup, S.; Cilento, F.; Crepaldi, A.; Zacchigna, M., et al., *Direct View of Hot Carrier Dynamics in Graphene.* Phys. Rev. Lett. **2013,** 111, 027403.

[100] Gierz, I.; Link, S.; Starke, U.; Cavalleri, A., *Non-equilibrium Dirac carrier dynamics in graphene investigated with time- and angle-resolved photoemission spectroscopy.* Faraday Discuss. **2014,** 171, 311-321.

[101] Ulstrup, S.; Johannsen, J. C.; Cilento, F.; Miwa, J. A.; Crepaldi, A., et al., *Ultrafast Dynamics of Massive Dirac Fermions in Bilayer Graphene.* Phys. Rev. Lett. **2014,** 112, 257401.

[102] Gierz, I.; Calegari, F.; Aeschlimann, S.; Chávez Cervantes, M.; Cacho, C., et al., *Tracking Primary Thermalization Events in Graphene with Photoemission at Extreme Time Scales.* Phys. Rev. Lett. **2015,** 115, 086803.

[103] Gierz, I.; Mitrano, M.; Bromberger, H.; Cacho, C.; Chapman, R., et al., *Phonon-Pump Extreme-Ultraviolet-Photoemission Probe in Graphene: Anomalous Heating of Dirac Carriers by Lattice Deformation.* Phys. Rev. Lett. **2015,** 114, 125503.

[104] Isabella, G.; Matteo, M.; Jesse, C. P.; Cephise, C.; Turcu, I. C. E., et al., *Population inversion in monolayer and bilayer graphene.* J. Phys.: Condens. Matter **2015,** 27, 164204.

[105] Johannsen, J. C.; Ulstrup, S.; Crepaldi, A.; Cilento, F.; Zacchigna, M., et al., *Tunable Carrier Multiplication and Cooling in Graphene.* Nano Lett. **2015,** 15, 326-331.

[106] Song, J. C. W.; Reizer, M. Y.; Levitov, L. S., *Disorder-Assisted Electron-Phonon Scattering and Cooling Pathways in Graphene.* Phys. Rev. Lett. **2012,** 109, 106602.

[107] Betz, A. C.; Jhang, S. H.; Pallecchi, E.; Ferreira, R.; Feve, G., et al., *Supercollision cooling in undoped graphene.* Nat. Phys. **2013,** 9, 109-112.

[108] Graham, M. W.; Shi, S.-F.; Ralph, D. C.; Park, J.; McEuen, P. L., *Photocurrent measurements of supercollision cooling in graphene.* Nat. Phys. **2013,** 9, 103-108.

[109] Someya, T.; Fukidome, H.; Watanabe, H.; Yamamoto, T.; Okada, M., et al., *Suppression of supercollision carrier cooling in high mobility graphene on SiC.* Phys. Rev. B **2017,** 95, 165303.

[110] Tielrooij, K. J.; Song, J. C. W.; Jensen, S. A.; Centeno, A.; Pesquera, A., et al., *Photoexcitation cascade and multiple hot-carrier generation in graphene.* Nat. Phys. **2013,** 9, 248-252.

[111] Tan, S.; Argondizzo, A.; Wang, C.; Cui, X.; Petek, H., *Ultrafast Multiphoton Thermionic Photoemission from Graphite.* Phys. Rev. X **2017,** 7, 011004.

[112] Bainbridge, A. R.; Bryan, W. A., *Velocity map imaging of femtosecond laser induced photoelectron emission from metal nanotips.* New J. Phys. **2014,** 16, 103031.

[113] Ye, H.; Kienitz, J. M.; Fang, S.; Trippel, S.; Swanwick, M., et al. In *Velocity Map Imaging of Electrons Strong-Field Photoemitted from Si-Nanotip*, 19th International Conference on Ultrafast Phenomena, Okinawa, 2014/07/07; Optical Society of America: Okinawa, 2014; p 09.Wed.P03.37.

[114] Fan, L.; Lee, S. K.; Tu, Y.-J.; Mignolet, B.; Couch, D., et al., *A new electron-ion coincidence 3D momentum-imaging method and its application in probing strong field dynamics of 2-phenylethyl-N, N-dimethylamine.* J. Chem. Phys. **2017,** 147, 013920.

[115] Daniel, N.; Thomas, F., *Image-potential states and work function of graphene.* J. Phys.: Condens. Matter **2014,** 26, 393001.

[116] Silkin, V. M.; Zhao, J.; Guinea, F.; Chulkov, E. V.; Echenique, P. M., et al., *Image potential states in graphene.* Physical Review B **2009,** 80, 121408.

[117] von Helden, G.; Holleman, I.; van Roij, A. J. A.; Knippels, G. M. H.; van der Meer, A. F. G., et al., *Shedding New Light on Thermionic Electron Emission of Fullerenes.* Phys. Rev. Lett. **1998,** 81, 1825-1828.

[118] Campbell, E. E. B.; Ulmer, G.; Hertel, I. V., *Delayed ionization of C_{60} and C_{70}.* Phys. Rev. Lett. **1991,** 67, 1986-1988.

[119] Richardson, O. W., *Thermionic Emission from Hot Bodies*. Wexford College Press: London, UK, 2003.

[120] Pop, E.; Varshney, V.; Roy, A. K., *Thermal properties of graphene: Fundamentals and applications.* MRS Bull. **2012,** 37, 1273-1281.

[121] Liang, S.-J.; Ang, L. K., *Electron Thermionic Emission from Graphene and a Thermionic Energy Converter.* Phys. Rev. Appl. **2015,** 3, 014002.

ABSTRACT

3D MOMENTUM IMAGING SPECTROSCOPY PROBING OF STRONG-FIELD MOLECULAR AND SURFACE DYNAMICS

by

LIN FAN

December 2018

Advisor: Dr. Wen Li

Major: Chemistry (Physical)

Degree: Doctor of Philosophy

Electron-ion coincidence measurements in combination with 3-dimensional (3D) momentum imaging can provide comprehensive 3D-momentum information to unravel multichannel photoionization/dissociation processes, and thus is an effective tool to investigate atomic/molecular dynamics. A camera-based 3D coincidence momentum imaging system and the velocity mapping imaging (VMI) based machine were introduced in Chapter 2. Studies of strong field dissociative single and double ionization of relatively large molecules camphor and 2-phenylethyl-N, N-dimethylamine (PENNA) were carried out and illustrated in Chapter 3. We demonstrated the main products of double ionization of PENNA were singlet diradicals. In Chapter 4, a novel time-of-flight angular-resolved photoemission spectroscopy was demonstrated. We employed this method to study multiphoton photoemission in thin metal films (Al and Cu), and hot carrier decay dynamics in graphene, in which unprecedented long hot carrier decay dynamics were observed (> 1 *ns*).

AUTOBIOGRAPHICAL STATEMENT

I was born and raised in China. I obtained my bachelor's from Hunan University and master's degree from Nankai University. Then I came to the USA to pursue Ph.D. education at Wayne State University. The experience here opened the door for me to see the charm and power of science and technology.

My publications are listed below:

1. <u>L. Fan</u>, S. K. Lee, P.-Y. Chen and W. Li**, "Observation of nanosecond hot carrier decay in graphene" **2018**, *J. Phys. Chem. Lett.* 2018, 9, 1485.

2. <u>L. Fan</u>, S. K. Lee, Y. J. Tu, B. Mignolet, D. Couch, K. Dorney, Q. Nguyen, L. Wooldridge, M. Murnane, F. Remacle, H. B. Schlegel and W. Li*, "A new electron-ion coincidence 3D momentum-imaging method and its application in probing strong field dynamics of 2-phenylethyl-N, N-dimethylamine" *J. Chem. Phys.* **2017**, 147, 013920.

3. S. T. Sun, B. Mignolet, <u>L. Fan</u>, W. Li, R. D. Levine and F. Remacle*, "Nuclear motion driven ultrafast photodissociative charge transfer of the PENNA cation: An experimental and computational study" *J. Phys. Chem. A* **2017**, 121, 1442.

4. S. K. Lee, Y. F. Lin, S. Lingenfelter, <u>L. Fan</u>, A. H. Winney and W. Li*, "Communication: Time- and space-sliced velocity map electron imaging" *J. Chem. Phys.* **2014**, 141, 221101.

5. S. K. Lee, F. Cudry, Y. F. Lin, S. Lingenfelter, A. H. Winney, <u>L. Fan</u> and W. Li*, "Coincidence ion imaging with a fast frame camera" *Rev. Sci. Instrum.* **2014**, 85, 123303.

6. <u>Fan, L.</u>; Yan, X.-P.*(2012): Evaluation of isostructural metal-organic frameworks coated capillary columns for the gas chromatographic separation of alkane isomers. *Talanta*, **2012**, 99, 944.